Probing the Universe with Space Based Low-Frequency Radio Measurements

by

Alexander M. Hegedus

A dissertation submitted in partial fulfillment
of the requirements for the degree of
Doctor of Philosophy
(Atmospheric, Oceanic and Space Sciences and Scientific Computing)
in The University of Michigan
2019

Doctoral Committee:

Professor Justin Kasper, Chair
Dr. Joseph Lazio, Jet Propulsion Laboratory
Professor Michael Liemohn
Professor Ward Manchester IV
Associate Professor Shravan Veerapaneni

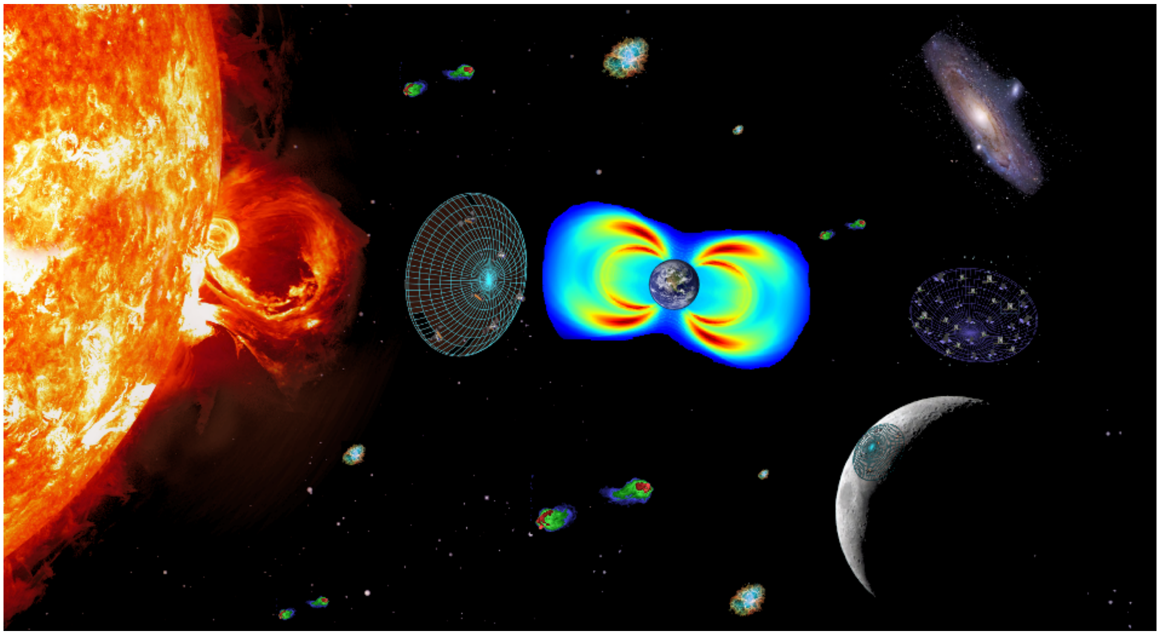

Alexander M. Hegedus
alexhege@umich.edu
ORCID iD: 0000-0001-6247-6934

ACKNOWLEDGMENTS

I would like to gratefully acknowledge all the mentorship I received from from NASA's Jet Propulsion Laboratory's (JPL) Dr. Konstantin Belov, Dr. Nikta Amiri, Dr. Joseph Lazio, Dr. Andrew Romero-Wolf, Dr. Farah Alibay, and Melissa Soriano. I would also like to thank JPL's Strategic University Research Partnership (SURP) Program, which funded over half of my time in graduate school. Part of this research was carried out at the Jet Propulsion Laboratory, California Institute of Technology, under a contract with the National Aeronautics and Space Administration.

I would also like to acknowledge the Network for Exploration and Space Science (NESS) team. They sparked my imagination with their plans of lunar radio science, providing great ideas and great camaraderie. This work was directly supported by the NASA Solar System Exploration Research Virtual Institute cooperative agreement number 80ARC017M0006, as part of the NESS team.

Thank you to Dr. Justin Kasper, who picked me out of a stack, and in a single meeting exhibited such a flaming curiosity for universe that it convinced to come here for my PhD. You have always an endless fountain of advice and inspiration through all these years. May we work together fruitfully for many more.

Finally, thank you to my friends and family who have supported me, distracted me, and listened to me through a long 5 years of graduate school.

TABLE OF CONTENTS

Chapter

LIST OF FIGURES

FIGURE

LIST OF TABLES

TABLE

LIST OF ABBREVIATIONS

CASA Common Astronomy Software Applications

SunRISE Sun Radio Interferometer Space Experiment

MoM Method of Moment

GNSS Global Navigation Satellite System

FFT Fast Fourier Transform

ECEF Earth Centered Earth Fixed

ECI Earth Centered Inertial

CME Coronal Mass Ejection

SEP Solar Energetic Particles

DRAGN Double Radio sources Associated with a Galactic Nuclei

LRO Lunar Reconaissance Orbiter

LOLA Lunar Orbiter Laser Altimeter

AKR Auroral Kilometric Radiation

ABSTRACT

Due to Earths ionosphere, it is not possible to image the sky below 10 MHz. Any waves below this cutoff frequency are absorbed by the plasma in Earths ionosphere, whose free electron density determines the cutoff. A constellation of small spacecraft above the ionosphere could enable radio imaging from space at frequencies below this cutoff, but the logistics and costs of doing this imaging using multiple satellites that are kilometers apart in a precise enough manner to form a radio array has until recently been unfeasible. With the lowering costs and increasing reliability of smallsats, the use of radio arrays in space is finally set to open up this new window through which we may observe the universe in a new light. For complex sources in the sky, analytical formulas are not enough to predict array performance; full simulations must be done to evaluate potential array configurations. Simulated outputs must be compared to a realistic input model to make sure that a given array configuration can meet its defined scientific requirements. Space-based arrays also introduce additional challenges in understanding novel data processing and errors from location retrieval of the receivers and budgeting for data transmission.

In this thesis I demonstrate the feasibility for different space-based radio arrays by simulating their performance under realistic conditions. I outline the science goals involving radio imaging below 10 MHz for a range of solar, astrophysical, and magnetospheric targets. I then outline different strategies for creating synthetic apertures in space that are well suited for each of these targets. I describe the calculations needed for each style of correlation and create a data processing and science analysis pipeline for showcasing the imaging performance of each simulated array.

I show that the SunRISE and RELIC array concepts are both able to meet their main scientific goals of localizing solar radio bursts and mapping radio galaxies respectively. I describe a novel way in which I use magnetohydrodynamic simulations of a solar eruption alongside real radio data to predict the sky brightness patterns of the radio bursts for input to the SunRISE pipeline across different theories of particle acceleration. This technique provides initial predictions of the location of solar type II burst generation in a coronal mass ejection that SunRISE can potentially confirm. I also demonstrate the feasibility of a lunar near side array powerful enough to image the Earths synchrotron emission, along with a zoo of brighter auroral emissions. Synchrotron measurements would provide a unique proxy measurement of the global energetic electron distribution in the Earths radiation belts. Such an array could also pinpoint the location of brighter transient events such as Auroral Kilometric Radiation with high precision, providing local, small scale electron data in addition to global data.

The time finally seems ripe for low frequency radio astronomy to make its move to outer space. Increased feasibility of small satellites is a huge game changer for the entire space industry, incentivizing mission designs that can take advantage of the distributive nature of multiple small inexpensive spacecraft to do the jobs traditionally done, or unable to be done, by larger, more costly single spacecraft. In that same spirit, this work acts as a helpful starting point for the general mission design, data processing, and science analysis required for distributed space-based radio arrays.

CHAPTER 1

Introduction

The field of radio astronomy began in 1932 with the accidental detection of galactic radio emission by Karl G. Jansky [9] at 20 MHz, in a range now commonly called the low frequency radio. Ever since then, radio astronomy has grown rapidly, catching up with higher frequency optical observations that have been going on for centuries longer. Another breakthrough was the utilization of radio interferometry, where groups of antenna separated by large distances are used to create a synthetic aperture, providing a way to scale up the sensitivity and resolution of radio observations [10] [2]. This can intuitively be thought of as an extension of the regular resolution formula for optical observations:

$$\Theta_{HPBW} \approx 1.22\frac{\lambda}{D} \tag{1.1}$$

For a observing dish of size D meters, and an observing wavelength of λ meters, Θ_{HPBW} is the angular size in radians of the Half Power Beam Width (HPBW), defining the resolution on the sky. The actual mathematics for radio interferometry are a little more involved, as we are attempting to synthesize a fraction of a large full dish with only scattered points across a mostly empty area. This process is also called *aperture synthesis*. For radio interferometry, the furthest distance between any two receivers in an array defines its resolution, taking the place of D in Equation 1.1. Radio interferometry has allowed amazing feats such as creating synthetic apertures as large as the Earth itself to image radio emission from the black hole M87 with the Event Horizon

Telescope at millimeter and sub-millimeter wavelengths [11] [12] [13]. Such an array is the result of worldwide collaboration and the combined effort of hundreds of scientists and engineers. Less than 100 years have passed since its genesis, yet it could be said that radio astronomy is nearing its limits on the ground.

This is not to say there is not still much to be learned from the ground; existing observatories and techniques can be expanded to add more sensitivity and resolution to existing arrays. Sky surveys of increasingly better resolution and sensitivity may be done, and better detection systems for transients such as Fast Radio Bursts may answer some open scientific questions, but there are some inherent limitations that all Earth bound arrays share. They are of course limited by the size of the Earth itself, limiting their potential resolution. There is also the matter of Earth's atmosphere, whose turbulence and opacity can corrupt measurements, and completely prevent them below 10 MHz. This lower limit is due to the Earth's ionosphere, whose free electrons prevents celestial radio waves below 10 MHz from reaching the ground and also makes measurements up to 30 MHz noisy and difficult. This has been demonstrated with many arrays; [14] reviews the issue in context of the Very Large Array (VLA). There is also the confusion limit, inherent to all arrays [15] [16], which limits the maximum density of reliably detectable and individually countable sources to about one source per 25 beam areas. Any denser of an imaging field and there will be inaccuracies in the resulting images from the interference of nearby clusters of point sources.

The obvious answer to this limitation is to put radio receivers into space where they can record data free of the influence of Earth's atmosphere. This has been done before with single antennas on spacecraft like Wind and STEREO, which have revealed a wealth of astrophysical processes that produced emissions in this low frequency radio range. We now know that there are emissions from the interactions of electrons with the Earth's magnetosphere, electron acceleration from solar eruptions, and from the galaxy itself. A plot from [1] is shown in Figure 1.1 that summarizes the frequency range and flux density of different sources as seen from Earth. Single antenna observations can measure the total flux density of such events, but cannot pinpoint where the emission is coming from. In order localize this low frequency emission and make images in this frequency

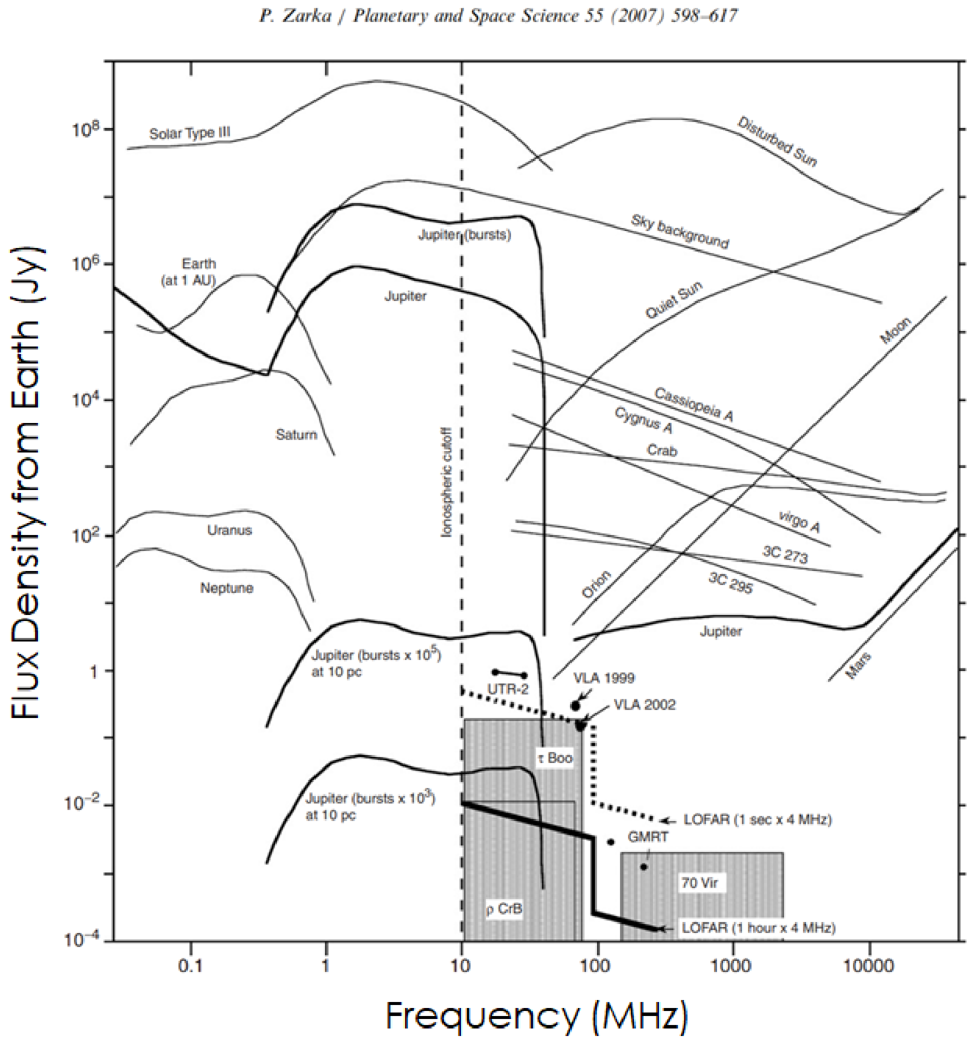

Figure 1.1: Plot from Zarka [1] that shows the strength of low frequency radio sources in the sky as seen from Earth over frequencies just above and below the Ionospheric cutoff, indicated by the dashed line at 10 MHz.

regime for the first time, many antennas will have to be sent to space and have their data combined to make a synthetic aperture. The Astronomical Low-Frequency Array (ALFA)[17] and the Solar Imaging Radio Array (SIRA) [18] are examples of early concept arrays that would overcome the ionospheric cutoff to target novel science at these low frequencies by putting multiple spacecraft with radio receivers into space. Interest in this area has only increased in recent years, with concepts for space-based arrays from teams all over the world being dreamed up, including NOIRE [19], CURIE [20], DSL [21], OLFAR [22], and more. In this thesis I demonstrate the feasibility for three different space based radio arrays by simulating their performance under realistic conditions, showing that they can achieve specific scientific goals. The arrays discussed here are SunRISE, RELIC, and an unnamed lunar near side array.

There are simple formulas for Signal to Noise ratios (SNRs) that hold for a point source on the sky of spectral flux density S_ν W/m^2/Hz and a single receiver with system temperature T_{sys}, effective area A_e, and system efficiency η_s that is focused on that point source. Spectral flux density is often presented in the derived unit 1 Jansky (Jy) = 10^{-26} W/m^2/Hz. The receiver system has a finite frequency bandwidth $\delta\nu$ Hz, and integrates the measurement for a period of δT seconds. The system temperature and effective area can also be tied together in a single parameter called the system equivalent flux density (SEFD). These formulas can be seen in Equation 1.2.

$$\frac{S}{N} = \frac{S_\nu A_e \eta_s \sqrt{\Delta\nu\Delta T}}{2k_B T_{sys}} = \frac{S_\nu \eta_s \sqrt{\Delta\nu\Delta T}}{SEFD} \tag{1.2}$$

We can extend this for an array of N_a antenna observing a point source. Each pair of antenna will yield us a single measurement, so the total number of measurements will be proportional to N_a^2. There will also be a measurement for each polarization, captured in the term N_{pol}. The SNR of an antenna array observing a single point source is shown in Equation 1.3. Vidal et al. [23] has shown how localization better than the array's beamwidth can be achieved provided there is a strong SNR. This overresolution is proportional to SNR$^{-0.5}$. This phenomena will be reviewed in depth in Chapter 5 in the context of bright transients. One may use these formulas to naïvely estimate how many antenna an array would need to detect a given point source brightness S_ν. One could also naïvely assume that that fitting an m parameter model to the emission would only take an N_a such that N_a(N_a-1)/2 $>$ m. For instance, this would imply that only N_a=5 antenna are needed to fit emission to an elliptical Gaussian ($m = 6$), since $5 * 4/2 > 6$. However, we will see that not all radio measurements are equal.

$$\frac{S}{N} = \frac{S_\nu A_e \eta_s \sqrt{N_a(N_a-1)N_{pol}\Delta\nu\Delta T}}{2k_B T_{sys}} = \frac{S_\nu \eta_s \sqrt{N_a(N_a-1)N_{pol}\Delta\nu\Delta T}}{SEFD} \tag{1.3}$$

In the realm of low frequency interferometry, these simple formulas do not always hold, since every pair of antenna are sampling a different Fourier component of the sky. This concept will be more rigorously spelled out in section 1.2 on interferometry. Equation 1.3 is for point source sensitivity, and is valid because the Fourier transform of a delta function has a constant non-zero amplitude. For diffuse structures in the sky, the Fourier transform of the sky brightness pattern is non-constant. This means the amount of signal added from a given pair of antenna is not constant, and imaging software like Common Astronomy Software Applications (CASA) [24] is needed to understand what the SNR would be for a given array configuration imaging diffuse structures with realistic noise. However, traditional radio astronomy software like CASA is hard coded to assume an Earth based array. To circumvent this, I have created an altered version of CASA that can simulate space based arrays. My version takes new space based sources of localization error into account, and can accurately track the changing array configuration from an evolving orbital constellation, as opposed to the standard of Earth rotation synthesis. This simulation pipeline will be leveraged to make sure the concept arrays described in the text can meet their scientific objectives.

The chapters of this thesis grow in scope as one progresses. After a introduction to the basic techniques commonly used in radio astronomy, I will describe the methodology changes that must be made for a space based array, and describe the pipeline used for simulating the array and analyzing its data. We note that there are differences in data processing and noise calculations for our main options of lunar surface arrays and free flying orbiting arrays compared to terrestrial arrays. Different hardware and data transmission costs are analyzed to find an optimal strategy for a given target in the sky.

We then look to small initial arrays that will be the first ones built for their low cost. These arrays will be suited towards detecting and imaging the brightest transients in the low frequency radio sky: solar radio bursts. We will describe the current theory for different types of solar radio bursts, and then describe the Sun Radio Interferometer Space Experiment (SunRISE) mission that hopes to answer some open scientific questions. Briefly put, SunRISE would detect Type II and III radio bursts, which are associated with Solar Energetic Particles (SEPs) accelerated into space by solar flares and Coronal Mass Ejections (CMEs). These solar radio bursts are thought to track the site of particle acceleration as it moves through the heliosphere. SunRISE hopes to answer where this site of particle acceleration creating the type II burst is in relation to the CME around it by providing low frequency radio images for the first time that we can compare with simultaneous coronagraph data. SunRISE also hopes to clarify to what extent electron jets fan out from a particular source region on the solar surface by tracking all the the type III bursts that originate from it. We also describe the extra things SunRISE might do as interesting extra radio science that could be expanded on with larger arrays.

As this thesis build in scope with larger arrays, it also turns its attention to dimmer targets that need the extra sensitivity of more antennas. The next set of objects in the sky described are orders of magnitude below solar radio bursts, and are mainly due to synchrotron radio emission from energetic electrons trapped in the magnetic fields of other galaxies. These are known as Double Radio Sources Associated with Galactic Nuclei (DRAGNs). These are the targets of RELIC, a concept for an array significantly past SunRISE in complexity and scope. RELIC will have improved resolution and sensitivity that allows it to measure astrophysical objects that are not detectable with smaller arrays. I demonstrate with realistic simulations that RELIC would be able to image the emission from large lobes on either side of a galactic center.

Then I move on to designing my own concept array on the Lunar near side that would be powerful enough to detect and image the Earth's synchrotron emission. Such an array would undoubtedly require a huge amount of infrastructure on the Moon, and is rivaling the scope of the largest arrays on Earth with 1000s of antennas. Such an array would be sensitive to all known low frequency emissions from Earth, and could serve as a near real time space weather monitoring station. By imaging the faint global synchrotron emission from the Earth, we would have a unique measure of global electron content in the radiation belts. We would also be sensitive enough to localize transient bursts to high precision, giving us an unprecedented understanding of the Earth's electron environment at both small and global scales.

The analysis and simulation techniques described here are applicable to any space based array concept. The use of radio arrays in space is set to open up a new window through which we may observe the universe in a new light. This new window promises to answer questions about particle acceleration near the Sun, and increase our understanding of the energetic electron environments both at Earth and all the way out to distant galaxies. Hopefully this work acts as a helpful starting point for the mission design, data processing, and science analysis required for space based radio arrays.

1.1 General Techniques

1.1.1 Antennas and Basic Formulas

All radio receivers record electromagnetic radiation by measuring the variation in voltage induced at the ends of the antenna. This voltage time series V_t is then typically treated with a Fourier transform and squared to get a voltage power spectral density V_f^2 that is then transmitted for further processing. V_f^2 can also be defined as an autocorrelation, as it is in Equation 1.4.

$$V_f^2 = 2\int_{-\infty}^{\infty} < V(t)V(t+\tau) > e^{i2\pi f\tau} d\tau \tag{1.4}$$

where brackets indicate a time averaged quantity. τ here is typically restricted to a single integration period before taking a Fourier transform. In order to compare the output of different receiver systems, we must translate V_f^2 into an external standard unit. Most common are the units of spectral flux density (Watts/meter^2/Hz) or brightness (Watts/Meter^2/Hz/Steradian). A common derived unit in radio astronomy is the Jansky (Jy), which is $1 \cdot 10^{-26}$ Watts/meter^2/Hz. To convert V_f^2 to a physically meaningful unit, one generally calibrates the antenna with a source with a known brightness. This allows a frequency dependent understanding of the effective area A_e of an antenna.

We assume a lossless antenna that has a complex impedance $Z_a = R_r + X * i$ with a real part R_r, called the radiation resistance, and a imaginary part X called the reactance. This quantity is dependent on the properties of the antenna and frequency f. For an antenna connected to a receiver of infinite impedance, the voltage power spectral density V_f can be described in terms of the antenna temperture T as described by Nyquist's 1928 formula:

$$V_f^2 = 4k_B T R_r \tag{1.5}$$

k_B is Boltzmann's constant and relates the kinetic energy of particles in a gas to the temperature in Kelvin of the gas.

One can relate antenna temperature in Kelvin, brightness, and flux density with the following equations. Following Plank's Law, or equivalently the Rayleigh-Jeans Law at low frequencies (valid for $f \leq$ 10s of GHz), we relate temperature and brightness with

$$B_f = 2\frac{k_B T}{\lambda^2} \tag{1.6}$$

Substituting Equation 1.6 into Equation 1.5, we can relate brightness to induced voltage and expand it for expressions over the whole sky.

$$V_f^2 = 2R_r\lambda^2 B_f \tag{1.7}$$

$$= 2R_r\int_{\Omega_{sky}} B(\Omega)A_e(\Omega)d\Omega \tag{1.8}$$

$$= 2R_r\int_0^{2\pi}\int_0^{\pi} B(\theta,\phi)A_e(\theta,\phi)\sin(\theta)d\theta d\phi \tag{1.9}$$

$$= 2R_r\int_0^{2\pi}\int_0^{\pi} B(\theta,\phi)\frac{\lambda^2}{4\pi}G(\theta,\phi)\sin(\theta)d\theta d\phi \tag{1.10}$$

Here, A_e is the effective area at that point in the sky. Since the total area of all lossless antenna is $\lambda/4\pi$, we can alternatively write $A_e(\theta,\phi) = \frac{\lambda^2}{4\pi}G(\theta,\phi)$, where is G is the defined as the gain, and defines the directionality of an antenna.

We can relate brightness to flux density by integrating its area in the sky. For a uniform brightness that covers the whole sky (approximately the case of galactic brightness at low frequencies), the flux density is $S_f = B_f\Omega_S$ with $\Omega_S = 4\pi$ for the whole sky. The isotropic observing area is $\lambda^2/(4\pi)$, and the deviation from that average is represented by the antenna gain in a given direction, $G(\theta,\phi)$. This collecting area is conserved, so any increase in gain for a given direction means less is available for other directions. This directionality of an antenna can be modeled using Method of Moment (MoM) simulation codes such as the Numerical Electromagnics Code NEC2 to predict the directional response and resistance of an antenna over a wide frequency range. For a handful of cases, such as an electrically short dipole, a half wavelength dipole, and 5/4 wavelength dipoles, analytical expressions can describe the ideal response of the antenna. We will now sketch out these equations for the case of the electrically short dipole where $L << \lambda$, which is a useful one to consider for low frequency astronomy, where for 0.1-30 MHz, the corresponding wavelength range is $\lambda = 3000 - 10$ meters

We can now substitute in the definitions for G and R_r for a short dipole. For a electrically short dipole antenna , the radiation resistance is given by standard texts such as [25].

$$R_r = \frac{2\pi}{3} Z_0 \left(\frac{l_{eff}}{\lambda} \right)^2 \tag{1.11}$$

where $Z_0 = \sqrt{\mu_0/\epsilon_0} \approx 120\pi$ is the impedance of free space and l_{eff} is the effective electrical length of the dipole antenna. [25] also gives the gain pattern of a short dipole as

$$G(\theta, \phi) = \frac{3}{2} \sin^2(\theta) \tag{1.12}$$

The factor of $\sin^2(\theta)$ comes from the fact that for a short dipole, the induced voltage from a current from a particular direction is projected with a basic $\sin(\theta)$ dependence. The power in the resultant Poynting vector will then be proportional to $\sin^2(\theta)$. As the length of a dipole increases, the antenna becomes inductive, and reaches a resonance at a length of $\lambda/2$. This will change the radiation resistance R_r and the antenna's gain pattern $G(\theta, \phi)$, making it more directional, with increased sensitivity to radiation coming in perpendicular to the antenna's polarization.

The actual voltage recorded by an antenna on a spacecraft is affected by the impedance of the receiver along with the stray/base impedance of the antenna base, amplifier, and connector cables. A shortened antenna will exhibit a capacitively reactive impedance, yielding a negative X reactance value, indicating that we need to add inductive reactance to cancel this capacitive reactance. This impedance matching process allows the accurate recording of the voltage that is proportional to the incoming brightness or current. Imperfections in this matching can reduce the gain in a receiver. This effect can be quantified with $\Gamma = |\frac{Z_s}{Z_a + Z_s}|$ for antenna impedance Z_a and stray impedance Z_s. A given inductor unit's performance varies over frequency, leading to a frequency dependence in the gain parameter. This makes the effective received voltage power spectral density V_r^2

$$V_r^2 = \left|\frac{Z_s}{Z_a + Z_s}\right|^2 V_f^2 \equiv \Gamma^2 V_f^2 \tag{1.13}$$

All the electronics in the receiver produce noise, depending on the hardware itself as well as the impedance of the antenna connected to it. This can be represented with a voltage term $V_{noise}^2 = |ZI_{noise}^2|$ that can also be conceptualized as a current source I_{noise}. This means that the overall voltage recorded will be

$$V_r^2 = V_{noise}^2 + \Gamma^2 V_f^2 \tag{1.14}$$

Combining all these equations allows us to predict the induced voltage for a constant sky brightness B_f, as it is for the galactic brightness at low frequencies, the response of a short dipole would be

$$\begin{align}
V_r^2 &= V_{noise}^2 + \Gamma^2 2R_r \int_0^{2\pi}\int_0^{\pi} B(\theta,\phi)\frac{\lambda^2}{4\pi}G(\theta,\phi)\sin(\theta)d\theta d\phi \tag{1.15}\\
&= V_{noise}^2 + \Gamma^2 2R_r \frac{\lambda^2}{4\pi}B_f\frac{3}{2}\int_0^{2\pi}\int_0^{\pi}\sin^3(\theta)d\theta d\phi \tag{1.16}\\
&= V_{noise}^2 + \Gamma^2 2R_r \frac{\lambda^2}{4\pi}B_f\frac{3}{2}\frac{8\pi}{3} \tag{1.17}\\
&= V_{noise}^2 + \Gamma^2 2\frac{2\pi}{3}Z_0\left(\frac{l_{eff}}{\lambda}\right)^2\frac{\lambda^2}{4\pi}B_f\frac{3}{2}\frac{8\pi}{3} \tag{1.18}\\
&= V_{noise}^2 + \frac{4\pi}{3}Z_0\Gamma^2 l_{eff}^2 B_f \tag{1.19}
\end{align}$$

which matches the expression used in [26] to calibrate S/WAVES.

1.1.2 Radio Interferometry

Radio interferometry is the act of combining the signals from different radio antenna to estimate the sky brightness pattern of a given frequency. The mathematics and theory of this field has been fleshed out in classic textbooks such as Thompson et al.'s Interferometry and Synthesis in Radio Astronomy [2]. Stated informally, the basic insight to understand is that for a group of antennas, the cross correlation of any pair of antennas will yield the information of a single 2D Fourier coefficient of the sky brightness pattern. The exact spatial 2D wave that is sampled depends on the separation between the given pair of radio receivers in units of wavelength of the observing frequency. The further apart the receivers are in a certain coordinate system oriented towards the imaging target, the higher the spatial frequency sample will be provided, giving higher resolution details at small scales. Conversely, the closer a pair of receivers are in that same reference frame, the lower the spatial frequency sampled, yielding larger scale structure information at a lower resolution.

This can intuitively be thought of as an extension of the regular resolution formula for optical observations:

$$\Theta_{HPBW} \approx 1.22\frac{\lambda}{D} \tag{1.20}$$

For a observing dish of size D meters, and an observing wavelength of λ, Θ_{HPBW} is the angular size of the Half Power Beam Width, defining the resolution on the sky. For radio interferometry, the furthest distance between any two receivers in an array defines its resolution, taking the place of D in Equation 1.1. The actual mathematics for radio interferometry are a little more involved, as we are attempting to synthesize a fraction of a full aperture with only scattered points across a mostly empty area. This process is also called *aperture synthesis*.

The two-dimensional Fourier transform between $f(l,m)$ and $F(u,v)$ can be written

$$F(u,v) = \int_{-\infty}^{\infty}\int_{-\infty}^{\infty} f(l,m)\exp^{-j2\pi(ul+vm)}\,dldm \tag{1.21}$$

$$f(l,m) = \int_{-\infty}^{\infty}\int_{-\infty}^{\infty} F(u,v)\exp^{j2\pi(ul+vm)}\,dudv \tag{1.22}$$

If l and m are in radians, then u and v are in units of cycles/radian. We write symbolically

$$f(l,m) \longleftrightarrow F(u,v) \tag{1.23}$$

The 3D coordinate system used is called the (u,v,w) frame. This is simply an $(x,y,z)/\lambda$ frame, naturalized to the observing wavelength, done in an idealized spectral 0 bandwidth framework. This frame is showed in Figure 1.2. An arbitrary point in the sky is deemed the phase center, to which the z, or w, axis of the frame is pointed. The sky brightness pattern around the source under observation is $I(l,m)$, where (l,m,n) are the direction cosines from the (u,v,w) coordinate system. This leads to a natural origin of (0, 0) at the phase center. The antenna baseline vector, measured in wavelengths, has length D_λ and components $(u,v,w) = (\Delta x, \Delta y, \Delta z)/\lambda$.

This separation of a pair of antenna (u,v,w) is called a *baseline*. After adding a phase lag for propagation effects, one correlates the signals to get the Fourier sample, called a *visibility*. One can obtain this visibility either by first cross correlating the analog signals and then Fourier transforming the resulting distribution (called XF correlation), or by first Fourier transforming the signal and then multiplying the corresponding channels (called FX correlation). Digital signal processing and the Fast Fourier Transform (FFT) have made it easy to do FX correlation, as the cross correlation (X). step in Fourier space is merely a multiplication of each pair of Fourier Coefficients. However it is done, the resulting visibility data, can then be inverse Fourier transformed into a dirty image at each frequency. One can use also fit the visibility data directly to various shapes of emission using an iterative algorithm to hone in on parameters of the shape. Both of these techniques are used and

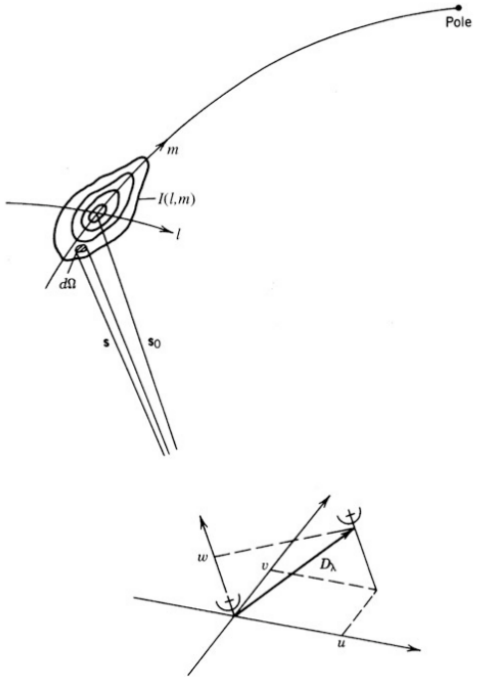

Figure 1.2: Taken from Thompson[2], this diagram shows the standard (u, v, w) reference frame used when observing the sky with a radio interferometer. An arbitrary point in the sky is deemed the phase center, to which the z, or w, axis of the frame is pointed. The sky brightness pattern around the source under observation is $I(l, m)$, where (l, m, n) are the direction cosines from the (u, v, w) coordinate system. This leads to a natural origin of (0, 0) at the phase center. The antenna baseline vector, measured in wavelengths, has length D_λ and components $(u, v, w) = (\Delta x, \Delta y, \Delta z)/\lambda$.

discussed in depth in Chapter 4.

For a planar array observing small field of view on the celestial sphere, one can use a 2D approximation, relating a visibility V with baseline $(u, v, w = 0)$, sky brightness pattern $I_\nu(l, m)$, and normalized antenna primary beam pattern $A_\nu(l, m)$ with a relation that is essentially a 2D Fourier transform. This result relating the 2D visibility function, also known as the mutual coherence between 2 antenna, to the Fourier transform of the sky Intensity pattern $I(l, m)$ is known as the van Cittert-Zernike theorem [2].

$$V_\nu(u, v) = \int\int \frac{A_\nu(l, m) I_\nu(l, m)}{\sqrt{1 - l^2 - m^2}} e^{-2\pi i(ul+vm)} dl dm \tag{1.24}$$

The full 3-D interferometry equation that relates a visibility V with baseline (u, v, w) and sky brightness pattern $I(l, m)$ is

$$V_\nu(u, v, w) = \int\int \frac{A_\nu(l, m) I_\nu(l, m)}{\sqrt{1 - l^2 - m^2}} e^{-2\pi i (ul + vm + w(n-1))} dl dm \tag{1.25}$$

This notation is standard and has been fine so far because ground based telescopes always have half of their collecting area towards the ground, so every (l, m) pair corresponds to a single point in the sky and assumes a positive n coordinate. In space there is nothing blocking the antenna, so this expression falls short since there are 2 points on the sky with the same (l, m) coordinates, with opposite n coordinates. For this reason it is necessary to integrate over n as well, seen below where $n' = n - 1$ is a helper variable to rewrite it as a 3D Fourier transform.

$$V_\nu(u, v, w) = \int\int\int \frac{A_\nu(l, m) I_\nu(l, m)}{\sqrt{1 - l^2 - m^2}} \delta(\sqrt{1 - l^2 - m^2} - n' - 1) e^{-2\pi i (ul + vm + wn')} dl dm dn' \tag{1.26}$$

$$\begin{aligned} &= \int_{-1}^{0}\int_{-1}^{1}\int_{-1}^{1} \frac{A_\nu(l, m) I_\nu(l, m)}{\sqrt{1 - l^2 - m^2}} e^{-2\pi i (ul + vm + wn')} \delta(\sqrt{1 - l^2 - m^2} - n' - 1) dl dm dn' \\ &+ \int_{-2}^{-1}\int_{-1}^{1}\int_{-1}^{1} \frac{A_\nu(l, m) I_\nu(l, m)}{\sqrt{1 - l^2 - m^2}} e^{-2\pi i (ul + vm + wn')} \delta(\sqrt{1 - l^2 - m^2} + n' + 1) dl dm dn' \end{aligned} \tag{1.27}$$

The integrals in the final line are constructed to cover both halves of the celestial sphere, with $n \in [0, 1] \equiv n' \in [-1, 0]$ in the first integral and with $n \in [-1, 0] \equiv n' \in [-2, -1]$ in the second integral.

CHAPTER 2

Designing a Space Based Array

In this chapter I analyze existing technology and simulate possible work flows to find the best hardware and data processing strategies for the position solving and correlation steps of space based radio arrays at various scales. I will assume these arrays are composed of many free flying spacecraft, and accurate knowledge of their relative positions is necessary for proper data analysis. Alternatively, we may have a radio array on the Lunar surface, where positional uncertainty is not a problem with a static array configuration, in which case the noise budget remains similar in principle with any ground based array. This topic will be investigated in Chapter 6. For now, I will assume free flying spacecraft that constantly updating positional awareness, either by using signals from existing Global Navigation Satellite System (GNSS) satellites in the case of SunRISE [27], or cross spacecraft ranging in the case of RELIC [28].

In this spacecraft ranging scenario, each spacecraft must emit a homing signal to its neighbours to keep each other updated to every ship's position. This system is not reliant on being near GPS satellites, so it is likely the best strategy for an array located further than a few Earth radii. In either case, each individual spacecraft may record data that can be used to solve for precise orbit determination (POD) solutions to determine the relative propagation delays between each spacecraft pair. Any errors in the position are translated into phase error of the complex correlation data following the equations laid out in the last chapter. The acceptable limits of error in position before harming the localization of the radio array are tested, using localization performance of SunRISE as a test case. This work help sets requirements for future space based arrays, particularly the quality of GNSS signal/ranging signal needed on each spacecraft as well as correlator capabilities. It is found that there are several feasible hardware and software combinations available today that could constitute a space based array, and recommendations are provided on which combinations would be well suited for various correlation strategies.

Synthetic aperture interferometers in space would have a variety of applications, from atmospheric sounding, to tracking particle acceleration by imaging the radio emission associated with coronal mass ejections in the inner heliosphere [29] [27], to imaging distant radio galaxies enabling the determination of magnetic fields and astrometric measurements [28], and studying magnetospheric emission from extrasolar planets. Studying the magnetospheres of both solar system planets and extrasolar planets was a topic that was mentioned multiple times at the recent Planetary Sciences Vision 2050 workshop [30]. Space-based radio arrays will operate above Earth's ionosphere, opening a new window (<10 MHz radio) to study the physical processes previously blocked for ground based radio arrays.

A key aspect of any synthetic aperture is the correlator, which is responsible for forming the synthetic aperture by appropriate combination of the signals from the individual antennas. JPL and the University of Michigan have teamed on two space based synthetic aperture concepts, the Geostationary Synthetic Thinned Aperture Radiometer III (GeoSTAR-III) [31] and the Sun Radio Imaging Space Experiment (SunRISE) [27], which took very different approaches to their correlators. GeoSTAR-III envisioned correlating signals in space while SunRISE proposes to downlink all of the data and correlate on the ground. GeoSTAR-III is a set of relatively small antennas that could all be mounted on a single spacecraft bus. Such an approach would not be feasible for constellation of free-flying spacecraft for which the antennas are large nor would it be feasible for future, larger synthetic apertures. Moreover, it is not clear if the SunRISE approach (downlinking all data to the ground) would be feasible for future larger arrays, necessitating on-board correlation.

The objectives of this Chapter are to:

1. Establish the feasibility of on-board correlation for space-based radio arrays.

2. Develop a model for a space based correlator, including the geometric, instrumental, and

propagation delays between each spacecraft pair.

3. Determine the breakpoints between the different approaches of correlation for space-based radio arrays with a particular focus on how to implement correlators for constellations of free-flying spacecraft.

Much of this chapter is taken from [32]. ©2019 IEEE. Reprinted, with permission, from Hegedus et al., Correlators for Synthetic Apertures in Space, 2019 IEEE Aerospace Conference.

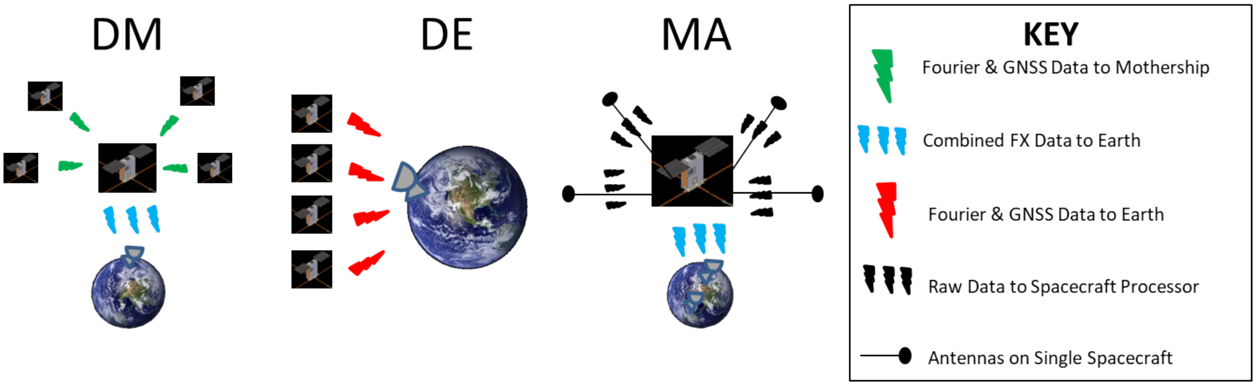

Figure 2.1: 3 Strategies of Correlation: Distributed-Mothership (DM), Distributed-Earth (DE), Multiple Antenna (MA)

Table 2.1: Data Processing and Transmission Steps over Correlation strategies

Time Flows ↓	Strategy DM	Strategy DE	Strategy MA
Daughtership Calculations	O(N log N) multiplies for FT parallel across each spacecraft	O(N log N) multiplies for FT parallel across each spacecraft	Send data from connected antennas to Central Processor O(SC*50MHz)
	Send Data to mothership	Send data to ground	
Mothership Calculations	Receive B frequency channels for each S/C	*	Receive raw data for each S/C
	Optional: Correlate O(SC^2*B) data		O(SC*N log N) multiplies for FTs
	Transmit visibilities to ground		Correlate O(SC^2*B) data
			Transmit visibilities to ground
Ground Calculations	Receive O(SC^2*B) visibilities	Receive SC*B Fourier channels	Receive O(SC^2*B) visibilities
		Correlate O(SC^2*B) data	

An outline of the Chapter is as follows: in Section 1 we describe various correlation strategies, in Section 2 we describe how we model space based correlators, including the positional uncertainty from localization imperfections. We showcase our end to end model for SunRISE to see how performance degrades as the error increases. In section 3 we examine different hardware options for space based correlation, finding space ready options well suited for different correlation styles. In section 4 we break down the communication costs of different bands and correlation strategies for various sized arrays and comment on when switching correlation strategies is cost effective.

Past work in conceptualizing different space based correlator options has been done recently, including work from 2013 by a Dutch group lead by Rajan [33] [34]. [33] was a in depth overview describing different correlator styles, including XF, FX, and HFX and their computational requirements. This classification is similar to ours in section 2, though we describe fewer categories and focus on FX correlation. [34] focuses on the synchronization requirements for a space based correlator, solving for the clock jitter requirements for a given SNR. They also provide a table of space qualified clocks and their masses and power needs. Both of these papers are focused on advancing the Orbiting Low Frequency Antenna Array (OLFAR) array concept [35].

The novelty in this paper is that we provide a list of processors for doing the correlation process, along with relevant space based parameters. We provide recommendations as to which processors are well suited to which correlation styles. We also compare different communication bands and their effect on data transmission prices to provide a larger trade study to determine when different correlation and transmission styles become optimal. We also use an end to end pipeline to test how much clock errors affect the localization performance of the array. As seen in section 2, the dominating source of error is the GNSS localization, which is typically in the nanoseconds, while clock jitter is in the picoseconds.

2.1 Correlation Strategies

Radio arrays consist of a constellation of individual radio receivers. Each receiver pair in the constellation forms a Fourier component of the radio brightness in the sky, the visibility, in standard notation, $V(u, v, w; \nu, t) = F[I(l, m; \nu, t)]$, where (l, m) are angular displacements on the sky, the spacecraft separations are measured in wavelengths $(u, v, w) = (\Delta x/\lambda, \Delta y/\lambda, \Delta z/\lambda)$ [2]. The visibility data V are functions of both time t and frequency , and F(·) indicates a Fourier transform (FT). A correlator involves 2 computational steps, the Fourier Transform (the 'F' portion), and a cross correlation step (the 'X' portion). They can be done either order, but digital signal processing has made it easy to do FX correlation, as the X step in Fourier space is merely a multiplication of each pair of Fourier Coefficients. The FX correlator returns samples of the visibility data, which is then inverse Fourier transformed into a dirty image at each frequency.

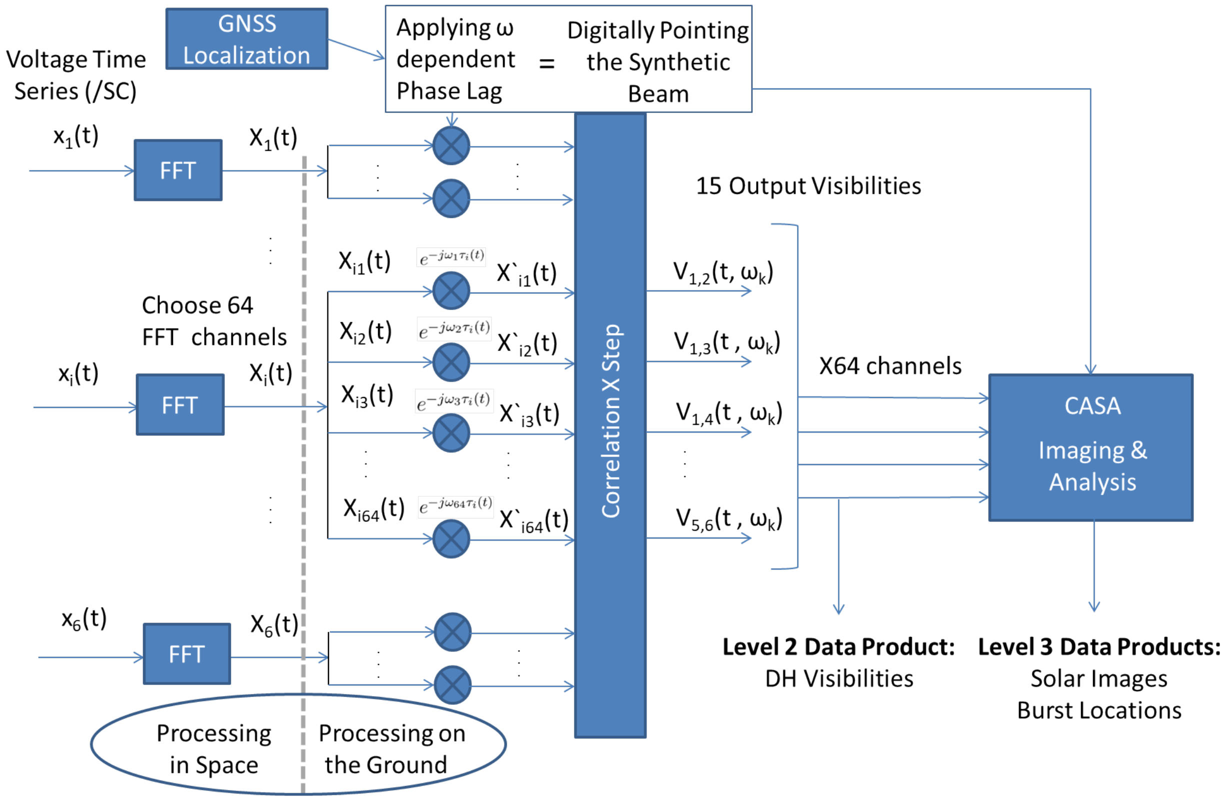

Figure 2.2: Flowchart Showing the Correlation Process for Space Based Array SunRISE

We focus our study to three options for the correlation of radio signals for space-based arrays, illustrated in Figure 2.1. They will be referred to as *Distributed-Mothership (DM)*, *Distributed-Earth (DE)*, and *Multiple Antenna (MA)*. *Distributed-Mothership (DM)*: Each spacecraft computes the first portion of correlation, the Fast Fourier Transform, individually. This data is then sent to a single spacecraft, which then may or may not perform the cross-multiplication, which is typically less demanding than the FT step. The resulting output is downlinked to Earth with a higher quality mothership antenna. *Distributed-Earth (DE)*: The correlator is implemented partially in space and partially on the ground. Each spacecraft individually computes the Fast Fourier portion and then transmits this data to the ground. The data is cross-correlated on the ground. *Multiple Antenna (MA)*: All of the correlator is implemented in space on a single spacecraft. Raw data from each antenna is sent to a central processor, which then computes the Fast Fourier transform portion and cross-multiplication of correlation.

The data processing and transmission steps that each strategy takes is detailed in Table 2.1. N is the number of samples per duty cycle, and is assumed to be 32,768 in this paper. This study assumes 64 frequency channels will be used per duty cycle out of a 4096 Polyphase Filterbank (PFB) are being transmitted for each spacecraft [36]. A PFB is a common alteration to a FT to decrease leakage of the signal across channels, and takes multiple samples per channel. We assume a factor of 4 to arrive at 32768 samples in total. SC is the number of individual receivers; assumed to be 1 per spacecraft in correlation strategies DM and DE, but multiple antenna for a single spacecraft in correlation strategy MA.

A critical issue for the correlator of any synthetic aperture is to have accurate positions for the individual antennas so as to be able to combine the signals from the individual antennas in phase. This issue is mitigated for a ground-based system, for which there are well-developed techniques for determining antenna positions referenced to the geoid, or a GeoSTAR-III like spacecraft employing correlation strategy MA, in which the antennas are mounted to a boom and remain relatively stable. This strategy is ideal for higher radio frequencies such as GeoSTAR-III's 153-180 GHz band. The stability the spacecraft provides ensures that the antenna separations are known to a high precision needed for the short observing wavelengths. This strategy cannot be used for low frequency radio interferometry (<10 MHz) where the wavelengths are meters to kilometers, so to get acceptable resolution the receivers must distributed in a free flying constellation (strategies DM and DE).

For free-flying spacecraft in a synthetic aperture, the positions of the individual antennas need to be determined continuously. GNSS-based precise orbit determination (POD) offers a potential solution to do that determination, but it requires that the correlator for the array is capable of ingesting such POD solutions to produce cross correlated visibility products. Receivers on board each spacecraft may record the radio emission and GNSS signals, keeping track of the time stamps of the arrival of the radio signals from which the relative propagation delays will be determined for correlation. Specifically, spacecraft can record carrier phase and pseudo-range data from any GNSS satellites they can see (usually at least 2, from GEO graveyard orbits, per SunRISE analyses). There are 2 levels of GPS solutions for space based radio arrays. One is to have Real Time Gipsy (RTGx) running on all of the spacecraft, this gives an approximate location to within 22 ns that is good enough to synchronize the taking of data between the duty cycles of all the spacecraft [37].

The next level is using GIPSY/OASIS-II (GOA-II) software, or its modern iteration GipsyX, to do post processing on the GNSS data to solve for even more precise locations down to 2 nanoseconds. Intense testing of this stage of processing was outside the scope of this report, but it has been demonstrated that RTGx can easily run on a Zynq 7020 FPGA. For array setups involving a mothership doing correlation on board, we will assume such a CPU is available for this further reduction of GNSS data to usable POD solutions.

2 nanoseconds corresponds to about 60 cm of positional uncertainty. This is because the signal they are getting from GNSS satellites is coming from a weaker sidelobe, and even with four Haigh-Farr COSMIC radio occultation antennas to pick up the signal, we can achieve better results on the ground with the full strength of the GNSS transponders. With 14 days worth of ground based data, the 3D rms positional error from GOA-II is 2.5 cm for GPS satellites, and 5 cm with 2 hours of data [38].

2.2 Modeling a Space Based Correlator

Cross-correlation of the radio signals enables a coherent combination of the signals forming a synthetic aperture. A correlator for a space based free flying radio array must be capable of ingesting GPS-derived antenna position and timing solutions to correctly produce the cross product visibility

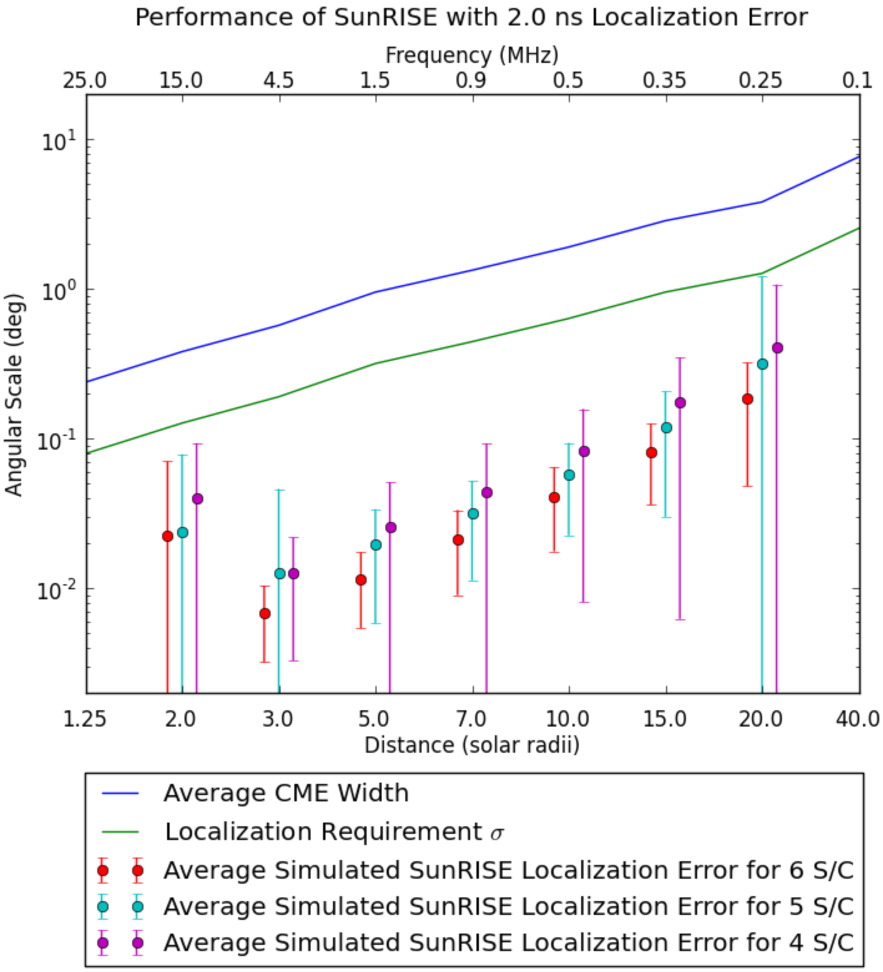

Figure 2.3: Realistic Localization Performance of 4, 5, and 6 Spacecraft in the SunRISE Array

data. Our model for space-based correlation is based on ground-based correlators, but with continuous updating of the receiver's relative positions. The model describes the spacecraft signals and computes phase delays, outputting the radio visibilities. The visibility data can then be Fourier inverted to form an image. We have built a version of this correlator pipeline, which takes in a GOA-II pos_goa file and correctly delays the incoming DH radio data to add it coherently across the entire array.

Uncertainties in the GNSS-derived POD and timing solutions could introduce phase errors in the cross-correlated signals, and, if not modeled accurately, they would introduce distortions in the final image, potentially shifting or distorting the apparent location of the radio emission. Imaging analysis of the performance was done to determine if GPS POD solutions of various qualities can be used to do successful correlation. This process is shown in Figure 2.2, with a specific focus on implementation for the 6 spacecraft SunRISE array employing correlation strategy DE. The process begins with a Fourier Transform (F step) of each of the antenna's data, followed by a frequency dependent phase shift calculated from the projected distances between receivers. Each Fourier coefficient is then pairwise multiplied (X step) to obtain the radio visibility data. This model for space based correlation takes in Earth Centered Earth Fixed (ECEF) coordinates, along with a target in the sky and computes the necessary phase delays to correctly correlate the data. The data is then sent off for imaging and analysis, which for SunRISE is described more in [39].

For the correlation strategy MA, the data processing & transmission reduces to that of strategy DM, only with a rigid formation of receivers and all processing already internal to a single spacecraft.

Table 2.2: List of Possible Hardware Options for doing Correlation Processing for Space Based Radio Arrays.

Processor type	Clock Speed	Max Multiplies/ 50 MHz clock cycle	Power Needed (W)	Total Ionizing Dose (TID) kRad	FX Correlation for 50 Spacecraft?
Zynq 7020 CubeSat Space Processor	667 MHz	2900	2	30	Yes
Virtex-5QV	360 MHz	2300	6	1000	Yes
Zynq 7100 CubeSat Space Processor	667 MHz	26000	9.5	30	Yes
Cubic Aerospace GPU	2 GHz	4000	<25	30	Yes

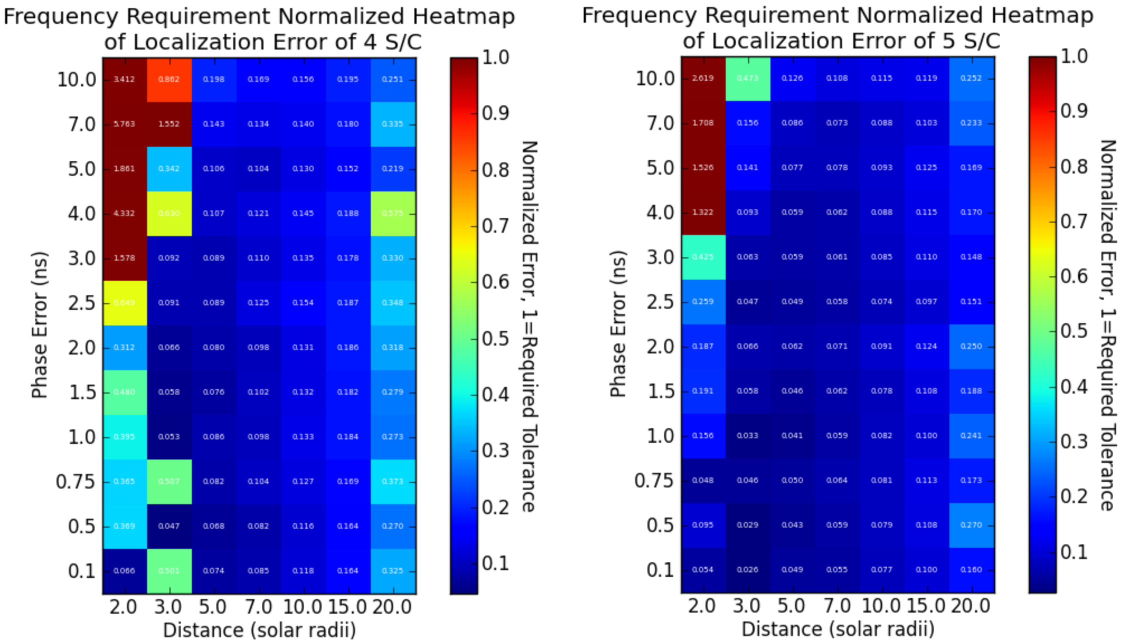

Frequency Requirement Normalized Heatmap of Localization Error of 4 S/C

Frequency Requirement Normalized Heatmap of Localization Error of 5 S/C

(a) 4 Spacecraft over a range of Phase Errors (b) 5 Spacecraft over a range of Phase Errors

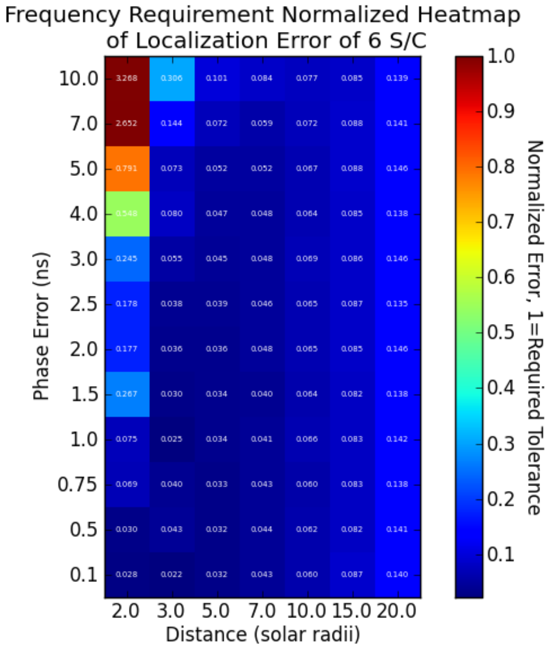

Frequency Requirement Normalized Heatmap of Localization Error of 6 S/C

(c) 6 Spacecraft over a range of Phase Errors

Figure 2.4: Localization Performance as a Function of Positional Uncertainty and Distance/Frequency. The color scale is maxed out at a normalized error of 1.0, so anything 1.0 and above will show up as red, which means there is too much error to meet the array's specified localization performance.

.

A conversion from the ECEF frame (the native frame for GNSS localizations) to the Earth Centered Inertial (ECI) frame must be done. This is a standard calculation and has been implemented in python [40]. Once in the ECI frame, it is a simple manner to rotate the axes so that the z direction is pointing towards the source the array is trying to image, given by an ephemeris of the target. The separations in this new z axis are important to note, as they must be treated as the propagation delays that allow coherent adding throughout the array. Any errors or uncertainties in the new z direction are translated into frequency dependent phase errors of the visibility data, where the same error (measured in seconds of light travel time) will affect the data more at higher frequencies with lower wavelengths, because the error is a larger fraction of the wavelength. This error is typically more consequential in strategies DM and DE, as the relative uncertainties are a larger fraction of the wavelength than for high frequency static arrays employing strategy MA like GeoSTAR-III.

The signals are then cross correlated in unique pairs to create the visibilities. We have used the SunRISE science pipeline as a test case, imaging Gaussian sources in the sky to act as the data behind the radio visibility data. This pipeline will be examined in more detail in Chapter 4, but we use it here as a stand in for an arbitrary array to show why this modeling is required in the first place. Figure 2.3 shows localization performance of the SunRISE array in 7 frequencies throughout its observing band, including realistic thermal noise and phase noise from positional uncertainty. The localization performance of SunRISE is compared to its requirements of 1/3 the width of a Coronal Mass Ejection at various solar distances and corresponding frequencies. The model developed for space based correlation was used here, taking in GNSS data along with the associated errors in spacecraft position. This positional error affects higher frequencies more due to their small wavelengths, thus introducing more phase error, seen here as a decrease in performance for 15 MHz compared to the overall trend. The averages and error bars reflect the distribution of 80 trials in localizing a Gaussian in the sky over constellation orbital phase and location of the burst in the sky.

GipsyX post processing on the ground gets the position error down to about 2 nanoseconds

(0.6 m). Performance is shown relative to the size of Coronal Mass Ejections at that frequency, and 1/3 of that size is set as SunRISE's requirement. Figure 2.3 shows the fact that even if SunRISE loses 1 or 2 spacecraft, it can meet baseline requirements. More details on the SunRISE imaging process may be found in [39].

Figure 2.4 shows results of similar simulations where the positional error has been varied. Heatmap plots are normalized to the baseline requirements, illustrating how much positional error can be tolerated by a 4, 5, or 6 spacecraft array. The distance in solar radii corresponds to the same frequency scale of 15 - 0.25 MHz in Figure 2.3. Plots like this can be used to help define positional accuracy requirements for future free flying space based radio arrays.

2.3 Mapping the Trade Space of Space Based Radio Array Hardware

We have examined several current hardware setups and found that many options have the capability to do all the signal processing for the FX correlation of a 50 antenna array, as seen in Table 2.2. We have computed the number of multiplies and adds each operation takes, and taken into account clock speeds and number of digital signal processing blocks to verify the hardware in question is suitable for correlation. We assume a 50 MHz antenna sampler to get a maximum frequency of 25 MHz. Anything higher than this is more easily and cheaply done on the ground. Most FGPAs and GPUs run at a higher speed than this, so it may do several iterations of operations for every sample of data that comes in, allowing better than real time processing for many spacecraft. Table 2.2 also includes approximate power usage rates, given by Xilinx Power Estimators for the various FPGAs [41] [42], and taken from a Technical Specifications Sheet for the GPU [43].

The Virtex-5QV FPGA is especially radiation hard, using a special wafer manufacturing process to increase its protection against latch up in the event of high energy particle bombardment. It has single event latch up immunity for radiation up to 100 $\mathrm{MeV{\cdot}cm^2/mg}$, in addition to having the highest Total Ionizing Dose (TID) tolerace. This translates to a Single-event functional interrupt in a GEO 36,000 km orbit of 2.76E-07 upsets/device/day. These properties mean that the Virtex-5QV may be useful for longer term missions, or for a mothership processor that would be safe even if it lost a couple daughterships with more radiation soft processors. The Zynq 7020 and 7100 are good candidates for processors for shorter term missions, or for correlation strategies that involve disposable daughterships doing parts of their own signal processing. The Cubic Aerospace GPU requires a bit more power than the FPGAs but in turn gains flexibility of operations. This hardware could be used in spacecraft with many components that require processing for many subsystems, not just simple signal processing.

Table 2.3: Data Rates, Hours to Transmit Data/Week, and Yearly Total Cost of 6 and 8 Spacecraft Arrays over DSN Bands

Property/Observing Band	X Band	Regular Ka Band	Near Earth Ka Band
Downlink Frequency	8.4 GHz	26 GHz	26 GHz
Equivalent Data Rate	2 Mbps	10 Mbps	150 Mbps
DE Hours to Transmit 6 SC	10 hours (2 x 3 MSPA)	*	*
DM Hours to Transmit 6 SC Space Correlation	75 hours	15 hours	1 hour
DM Hours to Transmit 6 SC Ground Correlation	30 hours	6 hours	0.4 hours
DE Total 1 Year Price 6 SC	$9627624	*	*
DM Total 1 Year Price 6 SC Space Correlation	$26244956	$13249012	$10216632
DM Total 1 Year Price 6 SC Ground Correlation	$16497972	$11299636	$10086684
DE Hours to Transmit 8 SC	10 hours (2 x 4 MSPA)	*	*
DM Hours to Transmit 8 SC Space Correlation	138 hours	28 hours	2 hour
DM Hours to Transmit 8 SC Ground Correlation	40 hours	8 hours	0.5 hours
DE Total 1 Year Price 8 SC	$12836832	*	*
DM Total 1 Year Price 8 SC Space Correlation	$42323852	$18064812	$12404352
DM Total 1 Year Price 8 SC Ground Correlation	$20663980	$13732796	$12115544

2.4 A Crossover in Optimal Correlation Strategies

We have examined the trade off between DE and DM (breaking DM into correlating in space vs correlating on the ground) as we increase the number of spacecraft. By spending more on a more powerful mothership, one may allocate a better communication antenna to communicate at a faster rate with the ground. A compiled list of Deep Space Network (DSN) frequencies and corresponding data rates is shown in Table 2.3 [44]. In calculating hours to transmit the data, an optimal setup of Multiple Spacecraft Per Antenna (MSPA) is assumed for the DE strategy. Doing MSPA allows data capture of multiple spacecraft for half the usual rate, for up to 4 simultaneous connections at twice the base cost. For instance, with 6 spacecraft, an MSPA of 3 is used, and for multiples of 4, an MSPA of 4 is used. As an example for the trade study, we have assumed a 1 year mission, using the DSN catalogue's pricing formulas for weekly data downloads with 100% margin on transmission time. GNSS data is on the order of 10% the volume of the DH radio data, and is assumed to be taken care of with the transmission margin. The basic form of the equation is shown below.

$$AF = R_B \left[A_W \left(0.9 + \frac{F_C}{10} \right) \right] \tag{2.1}$$

AF here is the hourly Aperture Fee, R_B is the flat hourly rate ($1037 for FY2010), A_W is the aperture weighting (4 for the 70 m dishes), and F_C is the number of station contacts per week.

The price of daughterships is assumed to be 1 million dollars each, and only has a less expensive X band transmission antenna. A mothership with a better Ka band antenna is assumed to be 5 million dollars. The DSN Ka band has the capacity to do a 150 Mbps downlink at near Earth distances, but can only do 10 Mbps at further distances (such as for Lunar orbiting arrays). A given constellation is assumed to have only 1 mothership that does the data transmission and/or the correlation. The only items included in the total cost summation are the data transmission and the costs of the spacecraft. We publish the options of 6 and 8 spacecraft, showcasing a shift in optimal strategy for the assumed baseline costs and bandwidths. The most cost effective strategy for 6 spacecraft and below is to apply the Distributed-Earth (DE) strategy. Above 6 spacecraft and 64 channels, the most cost effective strategy is to apply the Distributed-Mothership (DM) strategy with Near Earth Ka band to transmit Fourier data, where correlation is done on the ground to minimize data transmission costs. If the data is correlated pre-transfer, the data transmitted goes from from O(N) Fourier data for N spacecraft to O(N(N-1)/2) cross correlated visibilities, an unnecessary increase for no additional information that can't be cheaply extracted on the ground post-transfer. This crossover in price is seen in Table 2.3.

2.5 Trade Study Conclusions

All the pieces for space based radio interferometers are finally coming together, decades after they were first conceived of. Low cost smallsat parts along with ever smaller, more powerful computers have enabled the design process to proceed in earnest. The results of this paper contribute to the enabling of such arrays, sketching out different strategies and hardware that may be used. Multiple space qualified processor options were found that could do FX correlation for 50 spacecraft with a duty cycle of 32768 50 MHz samples every 100 ms. Simulated arrays were run with a range of errors in positional accuracy of individual spacecraft to demonstrate how acceptable error limits may be set depending on the various mission specific parameters such as signal strength and number of spacecraft. Much of the software and analysis done here is applicable to SunRISE, a University of Michigan and JPL led effort to create the first low frequency space based interferometer with the target of imaging solar radio bursts. The analysis done here also looks further to the future, finding hardware and software combinations that will enable even larger and more powerful arrays. We find that for arrays larger than a certain number (6 for our simple spacecraft cost model), the most cost effective strategy with DSN communication switches from every ship transmitting it's own data to the ground, to having a mothership with a more powerful Ka-band transmission antenna sending every ship's data down for ground based correlation. These price analyses provide a starting point for making informed design choices of larger future arrays.

CHAPTER 3

Solar Physics for Radio Emission

3.1 Solar Energetic Particles

Solar Energetic Particles (SEP) are space weather events that can have a range of harmful effects on Earth, from reducing GPS accuracy, to causing widespread blackouts. They are also potentially dangerous to astronauts or robots outside Earth's protective atmosphere. That same atmosphere also constrains us from viewing telltale signatures of SEPs in the lowest frequencies below 15 MHz. SEP events give off bright radiation further from the sun, scaling down with the local plasma frequency as the SEPs travel outward. In this range, we can see what are called type II and III solar radio bursts. These two types of bursts also nicely correspond to the main types of SEP events: gradual and impulsive, as reviewed in [45]. The local plasma frequency is only dependent on the density of electrons n_e, and so these accelerated particles mark a trail down through frequency space as they soar out from the Sun. The full formula for the local plasma frequency ω_{pe} is shown in Equation 3.1.

$$\omega_{pe} = \sqrt{\frac{n_e e^2}{m_e \epsilon_0}} = 8.98\text{kHz}\sqrt{n_e/cm^3} \tag{3.1}$$

In Equation 3.1 above, the elementary charge of an electron e, the mass of an electron m_e and the permittivity of free space ϵ_0 are all constants. SEPs are the main reason why it's important for us to fully understand the radio bursts associated with them, giving us an important and bright target

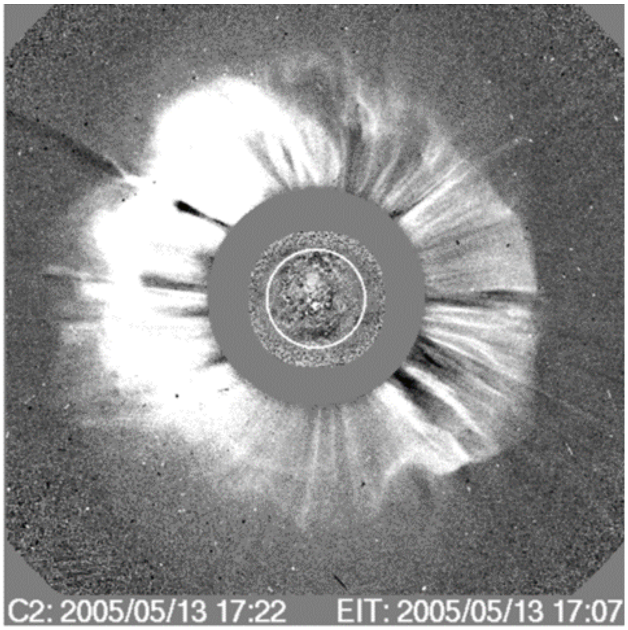

Figure 3.1: SOHO C2 coronagraph image of a 2005 ”Halo” CME that is headed towards Earth. This event was associated with a sustained type II burst, seen in Figure 3.6.

to image in the low frequency sky. As mentioned before, SEPs and their origin and transport are the major scientific motivators for SunRISE. Figure 3.1 shows a 2005 Coronal Mass Ejection (CME). CMEs are thought to be major source of SEPs. This particular CME was radio loud for over 24 hours and has been extensively modeled, as the next couple chapters will reveal.

3.2 Type II Bursts and Gradual SEP Events

Gradual SEP events make up the majority of SEPs seen at Earth, and are generated around shock waves from CMEs that are violently ejected from the sun. There are large eruptions of hot plasma creating a shockwave that can significantly impact the magnetic field structure of the surrounding environment. Type II bursts are associated with all strong gradual SEP events, and the frequency profile of the burst generally traces the height of the CME as it moves through the heliosphere, shocking the local plasma, and accelerating some of the downstream plasma to create SEPs. As reported by Winter et al. in [46], every single SEP event seen by Wind WAVES from 2010-2013 with a peak ≥10 MeV flux above 15 protons $cm^2s^1sr^{-1}$ are associated with a type II burst and

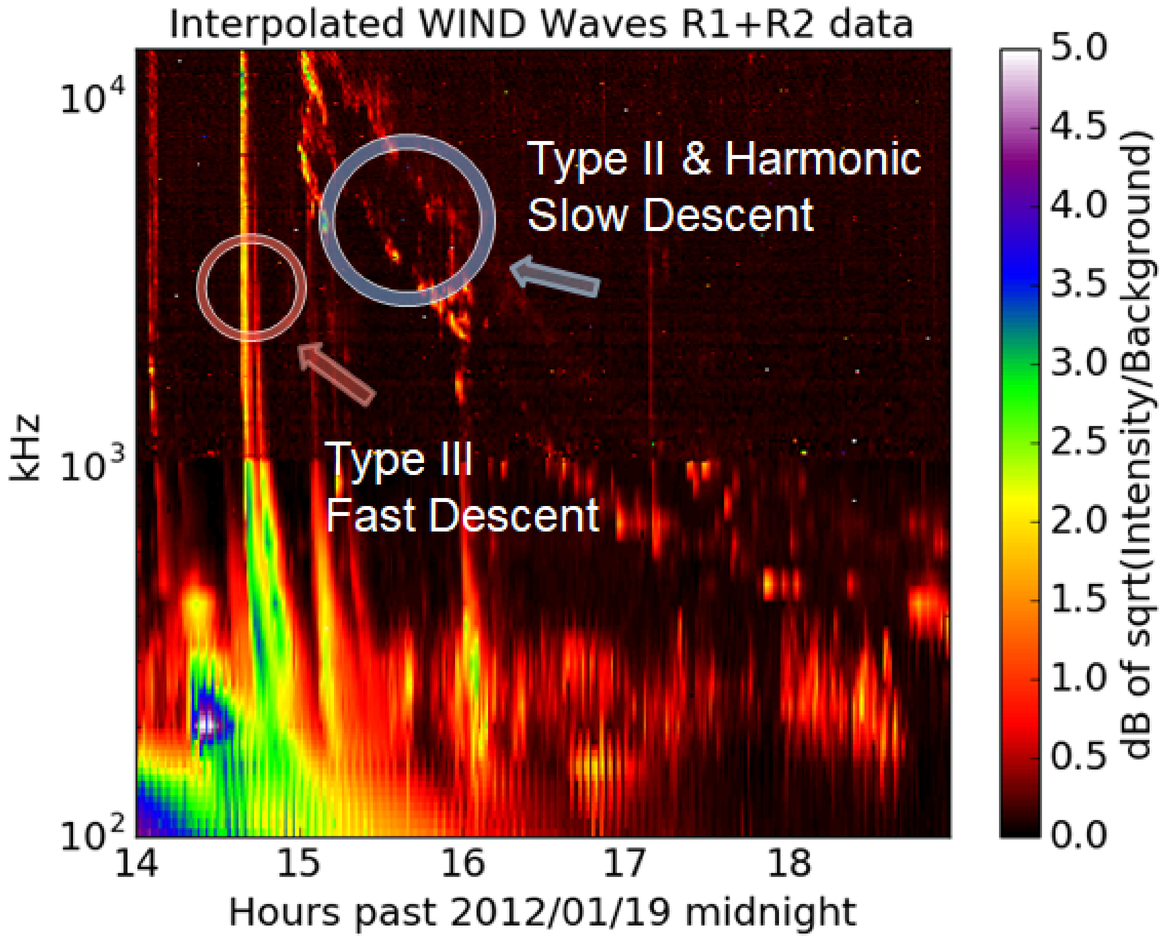

Figure 3.2: Radio Spectral Data from Wind/WAVES. Type II and III bursts are identified by their speeds of descent in frequency. Type II bursts follow along shockwaves moving out from the Sun, and descend slowly, while type III bursts follow a fast electron jet that descends far more quickly due to the higher speed of the jet.

virtually all SEP events, 92%, are also associated with a type III radio burst. Type III radio bursts that occur along with a Decametric-Hecametric (DH) type II burst are shown to be an important diagnostic that can be used to forecast SEP events. Type II and III bursts recorded by Wind WAVES are shown in Figure 3.2 in the 100 kHz to 10s of MHz range, though type III bursts can have a starting frequency higher than that [5].

They are thought to have their origin in Coronal Mass Ejections (CMEs). [47] shows a statistical analysis of type II bursts seen by the Wind WAVES instrument from 1997 to 2003. They show that they show a bandwidth to frequency to ratio (BFR) of between 0.1 - 0.4 in the frequency range 0.03 to 14 MHz of the RAD1 and RAD2 antennas.

The exact nature of the association of SEP events with CMEs and Type IIs are unknown in many respects. Basic questions about where in the geometry of the CME particles are being accelerated from perhaps one of the largest outstanding issues. There are a few classes of theories: the first one is acceleration at the shock front of the CME, described in [48] [49] [50], second is SEP generation with CME expansion and acceleration in the low corona [51], third is acceleration happening below the flux rope, at the current sheet [52] [53], and finally fourth is the possibility that a non-local acceleration is happening all occurring diffusely over a broad region as coronal plasma is diverted and compressed by the expanding filament [54].

3.3 Type III Bursts and Impulsive SEP Events

Impulsive SEP events are more numerous than gradual events, but overall create fewer energetic particles. Impulsive events are short lived bursts travelling quickly outward from a flare or jet on the surface of the Sun. These impulsive events are associated with type III bursts that also trace out the plasma frequency of the local plasma as they move outward, though they are far steeper in frequency as the electrons released from the jets are moving faster than the typical CME. A spectrum with an example of a type II and III burst can be seen in Figure 3.2. Due to their common nature, plenty of statistical studies have been done on type III bursts, characterizing their burst

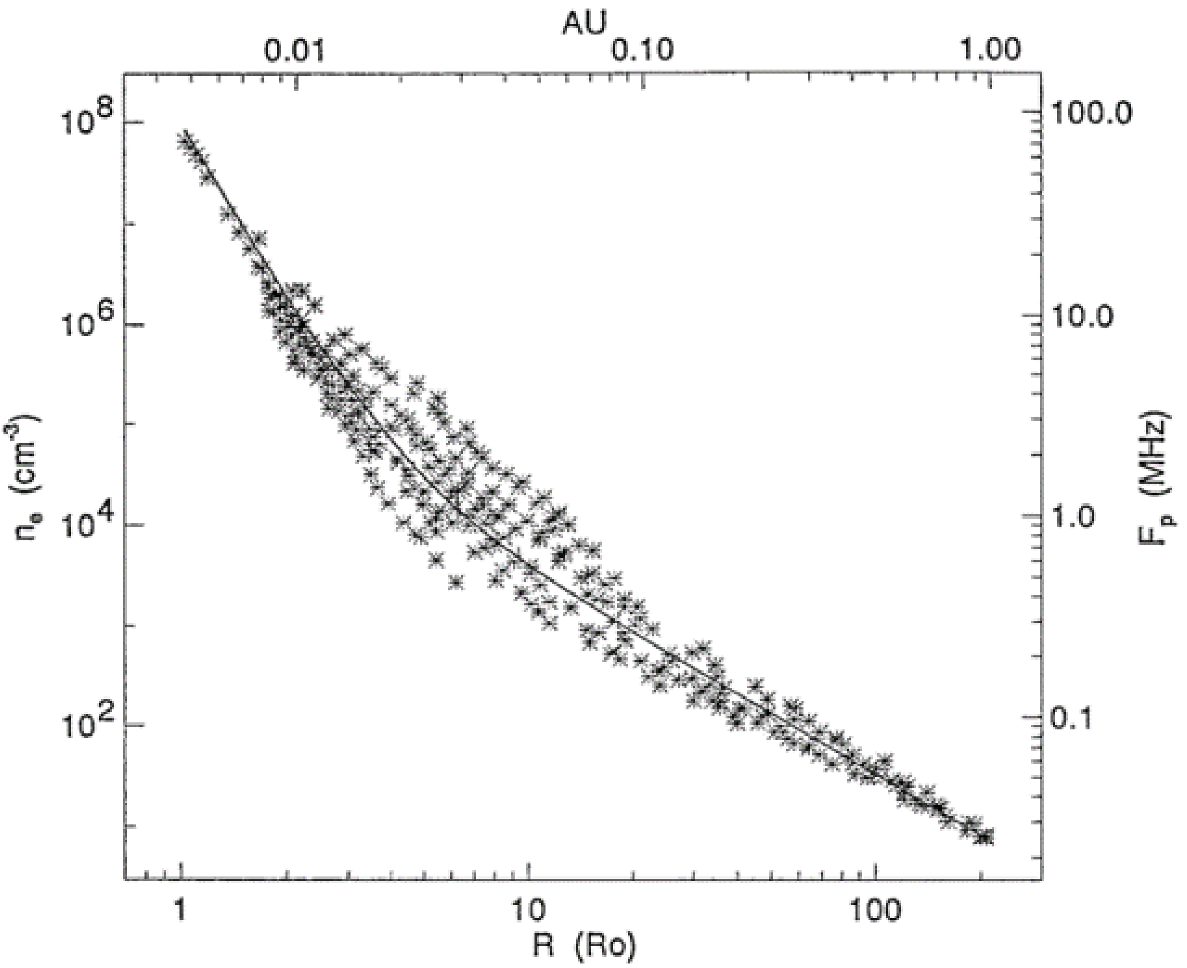

Figure 3.3: This plot from Leblanc et al. [3] shows the relationship between local electron density, local plasma frequency, and distance from the Sun. Each X is a distance-frequency fit of a frequency channel from 1 of 11 type III events. The line is the average fit of the electron density model.

duration, frequency drift rate, source flux, and more [5].

A famous paper from Leblanc et al. [3] traces the path of type III bursts through the heliosphere to 1 Astronomical Unit (1 AU is $1.496 \cdot 10^8$ kilometers) to create a model of the electron density in the central plane of the Sun. Figure 3.3, taken from [3], offers an intuitive way to see the relationship between distance from the Sun, and decreasing electron density and plasma frequency.

There has also been some appreciation recently of the high structure in time and frequency structure of these bursts, even past the normal variability expected from a faster drift rate. Figure 3.4 shows a set of spectra from LOFAR, a ground based low frequency array. With LOFAR's high

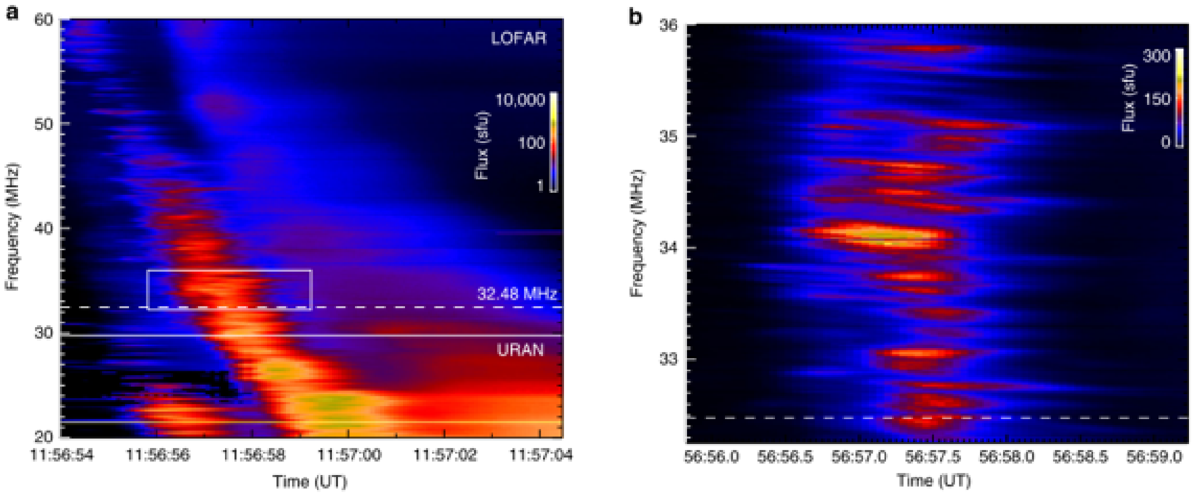

Figure 3.4: Taken from [4] this figure shows a fine time and frequency resolution spectra on a type III burst. Panel b zooms into the box on panel a; one can see the fine structure originating from the turbulent transport of the plasma.

time and frequency resolution, they see the fine structure of type III bursts, thought to originate from the turbulent transport of the plasma.

3.4 Current Theories

The prevailing physical theory for these radio bursts is the plasma emission mechanism, first put forward in 1958 by Ginzburg and Zhelezniakov [55]. The theory has been refined by them and many others over the years, as reviewed by Melrose in [6] and references therein. The basic idea is that the radio bursts are created in a multi-step process that starts with an electron beam, or a subpopulation of electrons that are much faster than their neighbors. In the case of impulsive SEP events, the jettisoned material itself is the beam, while for gradual SEP events, the beam is formed by acceleration of particles at a fast, strong CME driven shock. The fast Fermi model of acceleration is where the shockwave in the plasma reflects the incoming protons and electrons [56]. This leads to the formation of an electron beam upstream of the shock due to the fact that there is a minimum escape speed that is needed to move past the shock front. This imposes a sharp feature in the electron velocity distribution function that nature wants to smooth out.

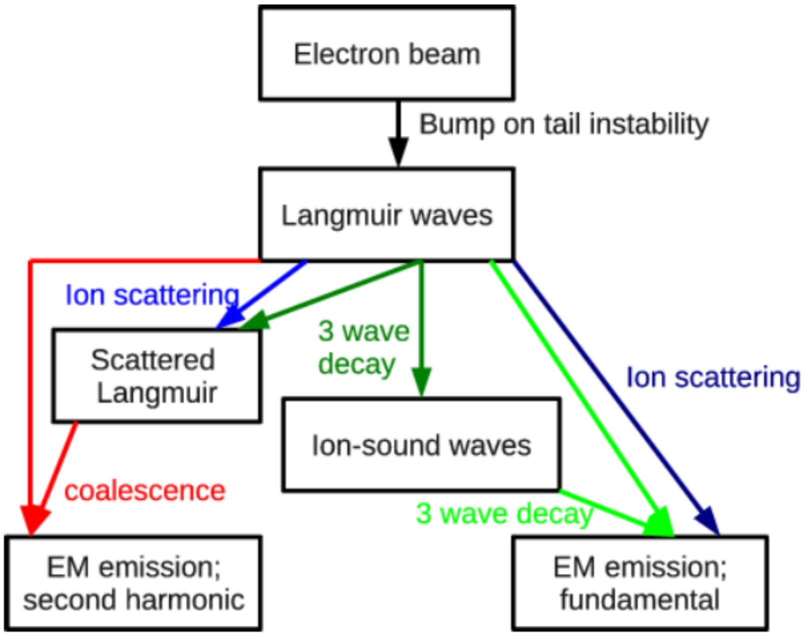

Figure 3.5: Taken from [5], adapted from [6], this flowchart describes the plasma emission mechanism, the widely accepted theory of radio burst generation given an electron beam either from energized particles at an CME driven shock, or from jettisoned material from a flare.

Once the electron beam is there, it is unstable to wave-particle interactions, and can generate Langmuir (plasma) waves with frequencies around the local plasma frequency via the standard bump-on-tail instability. The waves that are the right frequency to resonate with the beamed electrons convert energy from the electron beam to the plasma waves, relaxing the distribution function to a smoother profile. Then these Langmuir waves are converted to electromagnetic radio waves at some efficiency. There are many theories how this happens, but the leading one is called the plasma emission mechanism, and is described in Figure 3.5. Through a combination of 3 wave decay, ion scattering, and coalescence, a fraction of the power in the Langmuir waves can be converted into radio waves.

Pulupa et al. [57] shows that best predictor of Langmuir activity is the de HoffmannTeller speed, a result consistent with the fast Fermi model of electron acceleration. de Hoffmann-Teller frame velocity is the frame where the convection electric field vanishes on both sides of the shock. The angle between the shock normal and the magnetic field, Θ_{BN}, is also thought to important in deciding the acceleration zone. We know from single antenna observations that these bursts have a small 10% spread in frequency, but simulations of CME shocks have shown that if the entire shock surface was emitting a Type II burst, the frequency spread would be far larger.

3.5 MHD Simulations

In the past century or so, the scientific community has realized that space weather, dominated by the Sun, can have important effects here on Earth. One of these effects are Coronal Mass Ejections (CMEs). Coronal Mass Ejections are an eruption of highly magnetized plasma from the Sun that can cause disruptions when they reach Earth by shutting down satellites, global communications systems, airline control systems, and occasionally electric power grids. The largest CMEs, like the Carrington Event of 1859, or the 2012 CME that missed us by about a week could cause extensive blackouts, with a total economic impact of 1-2 trillion dollars. There is an estimated 12% chance that we will be hit by one of these in the next 10 years, and the most troubling part is that it could happen at any time [2]. However, if we are given enough warning, we can prevent catastrophic losses by taking the electrical grid offline. This is why space weather prediction models are essential for the survival of our technology centered society in the long term. In the past decades we have finally sent out spacefcraft to get in situ measurements of the solar wind and we can do certain observations such as measuring the magnetic field of the surface of the sun with instruments on the ground, but these are only pieces of the puzzle. We currently have no way of seeing how the plasma in the solar wind acts as it travels between the sun and the Earth, but we can make a good guess using the Magnetohydronamic (MHD) Equations. By using various measurements such as magnetograms (which measure magnetic field strength on the surface of the sun), space weather models such as the Space Weather Model Framework (SWMF) [58] (created and maintained here at Michigan) the model can propogate forward plasma through the heliosphere, eventually linking it up with models of Earth, and seeing how it interacts. By using a model to link up various inputs and solving the MHD equations between them, we can get a good guess at a unified picture of the entire environment.

3.5.1 MHD Equations

Magnetohydrodynamic models may be used to simulate the overall activity from the heliosphere. These rely on a numerical discretization of Maxwell's equations to take an initial configuration and march it forward in time. A Solar magnetogram that tells the magnetic field strength and polarity of the surface of the sun is used to initialize the simulation. Below are the simplified MHD partial differential equations in their symmetrizable formulation; the equations are respectively for mass conservation, momentum conservation, the induction equation, and the energy equation [59].

$$\frac{\partial \mathbf{U}}{\partial t} + (\nabla \cdot \mathbf{F})^T = \mathbf{Q} \tag{3.2}$$

where $\mathbf{U}$ is the vector of conserved vector quantities

$$\mathbf{U} = \begin{pmatrix} \rho \\ \rho \mathbf{u} \\ \mathbf{B} \\ E_{mhd} \end{pmatrix} \tag{3.3}$$

$\mathbf{F}$ is the flux dyad

$$\mathbf{F} = \begin{pmatrix} \rho \mathbf{u} \\ \rho \mathbf{u}\mathbf{u} + (p + \frac{1}{2\mu_0}B^2)\mathbf{I} - \frac{1}{\mu_0}\mathbf{B}\mathbf{B} \\ \mathbf{u}\mathbf{B} - \mathbf{B}\mathbf{u} \\ \mathbf{u}(E_{mhd} + p + \frac{1}{2\mu_0}B^2) - \frac{1}{\mu_0}(\mathbf{u} \cdot \mathbf{B})\mathbf{B} \end{pmatrix}^T \tag{3.4}$$

Here, E_{mhd} is the magnetohydronamic energy, given by

$$E_{mhd} = \frac{1}{2}\rho u^2 + \frac{1}{\gamma - 1}p + \frac{1}{2\mu_0}B^2 \tag{3.5}$$

and $\mathbf{Q}$ are the sources.

$$\mathbf{Q} = -\nabla \cdot \mathbf{B} \begin{pmatrix} 0 \\ \frac{1}{\mu_0}\mathbf{B} \\ \mathbf{u} \\ \frac{1}{\mu_0}\mathbf{u} \cdot \mathbf{B} \end{pmatrix} \tag{3.6}$$

This $\mathbf{Q}$ term is 0 in the conservative formulation, but adding these terms gives the system some good qualities. First off, it makes the system symmetrizable. An $n \times n$ matrix A is said to be symmetrizable if there exists an invertible diagonal matrix D and symmetric matrix S such that $A = DS$. Symmetrizable matrices are known to have an inverse, so codes can use state of the art inversion and diagonalization algorithms, greatly decreasing computational complexity and increasing the speed of the simulation, making this class of matrices very favorable to work with. A system without the source term, while conservative, is not Gallilean invariant, and has a zero eigenvalue in the Jacobian matrix, making the matrix non-invertible. Secondly, with this formulation, one can derive another conservation law for entropy $s = log(p/\rho^{\gamma})$,

$$\frac{\partial(\rho s)}{\partial t} + \frac{\partial(\rho s u_x)}{\partial x} + \frac{\partial(\rho s u_y)}{\partial y} + \frac{\partial(\rho s u_z)}{\partial z} = 0 \tag{3.7}$$

which is how entropy behaves in most physical systems. This formulation also makes the system Galilean invariant, a nice property that says all waves propagate at speeds $u \pm c$, where c is the wave speed, specified by the Alfvén speed, or the slow or fast magnetosonic speeds.

Another problem this $\mathbf{Q}$ term solves is the constraint that $\nabla \cdot \mathbf{B} = 0$. This is also called the ”Eight-wave scheme” and its discretization leads to enhanced stability and accuracy. One can think of it as propagation of jumps in the normal component of the magnetic field. However, if there are regions in the flow where $\nabla \cdot \mathbf{B}$ is large, the numerical errors can generate unwanted magnetic fields. Adding this term helped stabilize the simulation.

3.5.2 Volume Discretization Scheme

Systems of equations in conservative form like what we have here are well handled by finite volume discretizations. We split a computational domain up into individual 3D cells, where each cell is represented by an average value for the conserved quantities within that cell. By simply calculating the total flux in/out for every cell, if the cells are small enough, we can get accurate results, which hold up even in near discontinuous situations such as shock waves. The detail that can make or break a simulation when using a finite volume scheme is how the spatial derivatives are calculated. The most straightforward methods involve symmetric-centered differences, but these lead to numerically unstable schemes.

A better way to do it is to use an approximate Riemann solver, which is more accurate in interpolated values of fluxes at boundaries of cells. Many modern schemes use a method from van Leer called the monotone upstream-centered scheme for conservation laws (MUSCL) approach.

Specifically, the equations are

$$q_{i+\frac{1}{2}} = q_i + \frac{1}{2}\phi(r_{i+1/2})(u_i - u_{i-1}) \tag{3.8}$$

$$r_{i+1/2} = \frac{u_i - u_{i-1}}{u_{i+1} - u_i} \tag{3.9}$$

$$\phi(r) = \frac{r + r^2}{1 + r^2} \tag{3.10}$$

Again, these were more accurate than just using a basic centered difference approximation.

3.5.3 Time Discretization Scheme

Different time stepping schemes are possible in these sorts of models, each having their own uses. Explicit time stepping schemes give the measurement of the conserved vector at the next time step as a function of only past values. This scheme is simple, doesn't require solving any complex equations, but has a shorter time step compared to other methods. However, explicit time methods can capture the behavior of shocks quite well.

Explicit time steps are limited by the Courant-Friedrichs-Lewy (CFL) condition, which ensures that no information travels more than one cell size during a time step. This condition represents a nonlinear penalty for highly resolved calculations, because finer grid resolution not only results in more computational cells, but also in smaller time steps.

To do explicit time stepping, we simply solve the following equation for every cell i and time step n

$$U_i^{n+1} = U_i^n + \Delta t_i^n (-\nabla \cdot \mathbf{F} + Q)_i \tag{3.11}$$

where the time step Δt is determined by the local CFL condition

$$\Delta t_i^n = C \frac{\Delta x_i}{c_i^{fast}} = |u_i| \tag{3.12}$$

for Courant number C ≈ 1 and c_i^{fast} is the fastest speed anything can move in the cell, given by $u + v_f$ for fast magnetosonic speed v_f

$$v_f = \frac{1}{2}((a_s^2 + v_A^2) - \sqrt{(a_s^2 + v_A^2)^2 - 4a_s^2 V_{A_n}^2}) \tag{3.13}$$

$$a_s^2 = \frac{\gamma p}{\rho} \tag{3.14}$$

$$V_A = \frac{B}{\sqrt{\mu_0 \rho}} \tag{3.15}$$

where a_s^2 is the acoustic speed, V_A is the Alfvén speed, and V_{A_n} is the normal component of the Alfvén speed.

For adaptive grids like the ones that BATS-R-US uses, the time step is set to be inversely proportional to cell size, so that finer cell typically makes two half time steps while the coarser cell makes only one full time step. In this method, a global stability condition determines the time steps compared with local time-stepping in which time steps are set on a cell-by-cell basis

The other main category of time stepping methods are implicit methods. These methods are used in places where the plasma is not as dynamic, and allows a time step around 1000-10000 times larger than that of explicit time stepping. The trade-off is that to do so one must solve a system of nonlinear equations for all flow variables at each time step, which requires 20-30 times more CPU time per time step than explicit time stepping. Modern iterations of the BATS-R-US model automatically analyzes the problem and uses the most optimal choice between explicit, implicit, or point-implicit time stepping schemes [58].

3.5.4 The AWSoM Model

The Alfvén Wave Solar Model (AWSoM) was recently developed at the University of Michigan and acts as an upgrade to the physics running on the SWMF [60]. AWSoM includes a generalization of the Alfvén wave turbulence to counter-propagating waves on both open and closed field lines. The outward propagating waves are now partially reflected by the Alfvén speed gradients and field-aligned vorticity. The balanced turbulence at the apex of the closed field lines is accounted for. AWSoM also generalized separate electron and ion temperatures to anisotropic ion temperatures and isotropic electron temperatures. To distribute the turbulence dissipation to the coronal heating of the three temperatures, we use the results of the linear wave theory and nonlinear stochastic heating as presented in Chandran et al. (2011) [61]. AWSoM also incorporates collisionless heat conduction into ites treatment of isotropic electron temperature.

Compared with the two temperature solar wind model, the AWSoM model is a three-temperature MHD model that considers the anisotropy of ion temperature in the solar corona and the inner heliosphere. The coronal heating and solar wind acceleration are addressed with low frequency Alfvn wave turbulence. The Alfvn waves are partially reflected by the Alfvn speed gradient and the vorticity along the field lines, which may be important in close proximity of the active region. At the inner boundary, Alfvn wave energy whose Poynting flux was proportional to the magnetic field strength is injected. This all leads to a more realistic simulation that better matches real data.

3.5.5 Simulating the 2005/05/13 CME

The AWSoM model was used to model the inner corona, and was coupled to a heliospheric model with the Space Weather Modeling Framework (SWMF) to model the CME from 2005/05/13 [62]. Radio spectra for this event can be seen in Figure 3.6, where the type II burst has been identified with a white dashed line. The ambient solar wind is structured with a GONG synoptic magnetogram to produce the conditions of CR 2029. The CME is driven by a magnetic flux rope that possesses common characteristics of pre-event structures, including a dense helmet streamer with a cavity and core threaded by the flux rope. The CME is expelled from the corona with a peak speed of nearly 2000km/s, closely matching the speed observed in the corona, and propagates beyond Earth orbit. Snapshots from this simulation are shown in Figure 3.7.

3.6 Simulating Radio Bursts on top of MHD

I propose that we can use MHD simulations to predict what radio bursts would look like for different theories of particle acceleration around CMEs, utilizing different data cutsfor each of the main

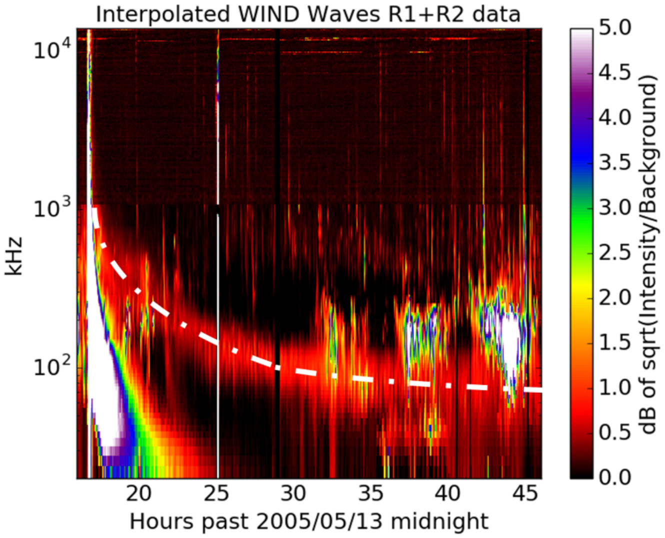

(a) Long time frame

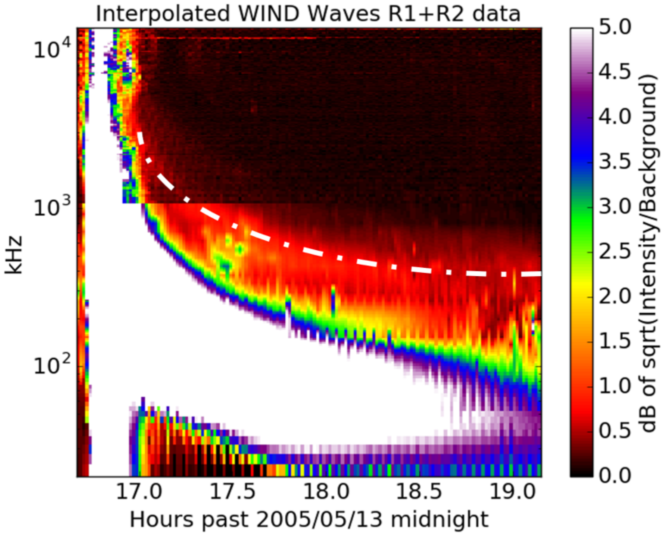

(b) Short time frame

Figure 3.6: Sustained Type II burst from a CME on 2005/05/13. This was a halo (heading straight toward Earth) CME that was radio loud for over 25 hours, tracing out the location of particle acceleration on the shockwave.

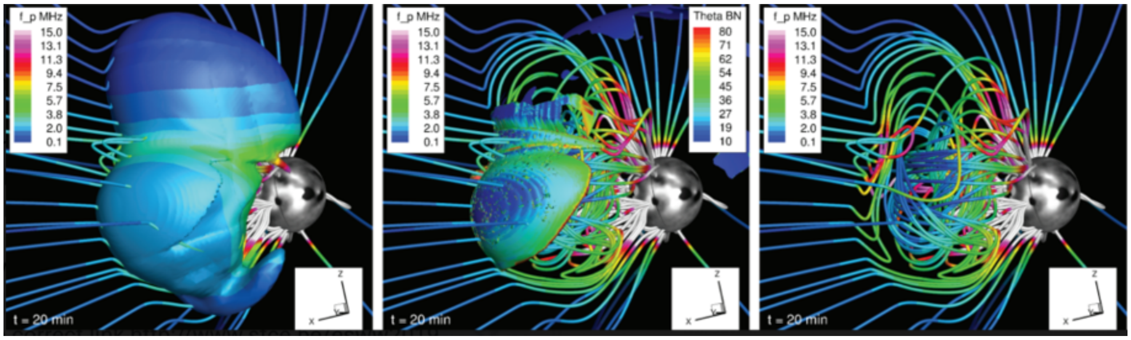

Figure 3.7: Snapshots from a AWSoM 2-Temperature MHD Simulation of a Radio-Loud CME on May 13, 2005

theories. Figure 3.7 shows some derived quantities of the points on the MHD simulated shock from an AWSoM simulation of the May 13 2005 CME.

I was given snapshot data from this simulation, each file containing a subset of the points of the run for each timestep that were all meeting some criteria, along with the plasma parameters for them. I received 3 main data cuts: points identified to be in the current sheet from a 3.5 MK isosurface, points that were shocked to a factor of 4 or more in their density compared to before the shockwave, and points that had a large change in entropy compared to before the shockwave.

I had a set of points for each of these categories, over the 2 hours of the simulation. The time cadence for these snapshot data was every 2 minutes in the beginning of the run, transitioning to every 5 minutes later in the run for a total of 35 snapshots over 120 minutes.

I have below made 4 different data cuts corresponding to the 4 classes of hypotheses for particle acceleration in CMEs: Shock Front, Flank, Current Sheet, and diffuse acceleration. Each of these data cuts contains a multitude of points that each have their own set of plasma parameters. Aside from the Current Sheet data cut, which was made with a 3.5 MK temperature selection, all the other data cuts were made using an angular slice of the simulation that corresponds to a theorized area of particle acceleration. Using the plasma parameters in each data cut, we can calculate the plasma frequency with equation 3.1. We then look at the distribution in frequency over time for each data cut. These can then be made into a sort of synthetic spectra, showing the possible frequencies that each data cut could emit in over time. The colors in these spectra correspond not to intensity,

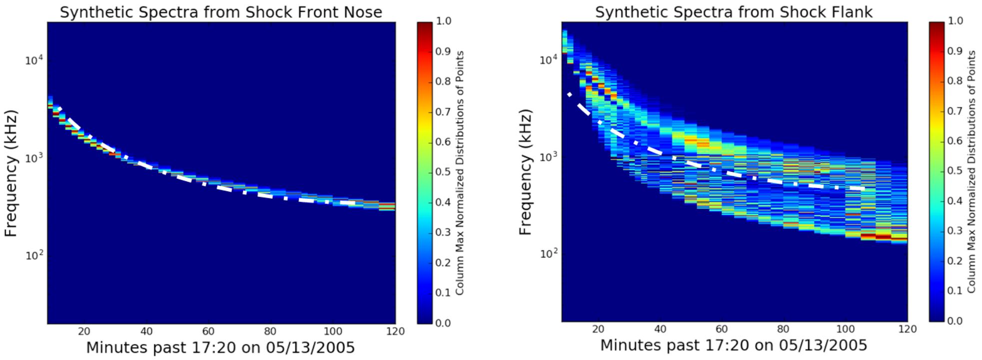

(a) Shock Front Data Cut (b) Shock Flank Data Cut

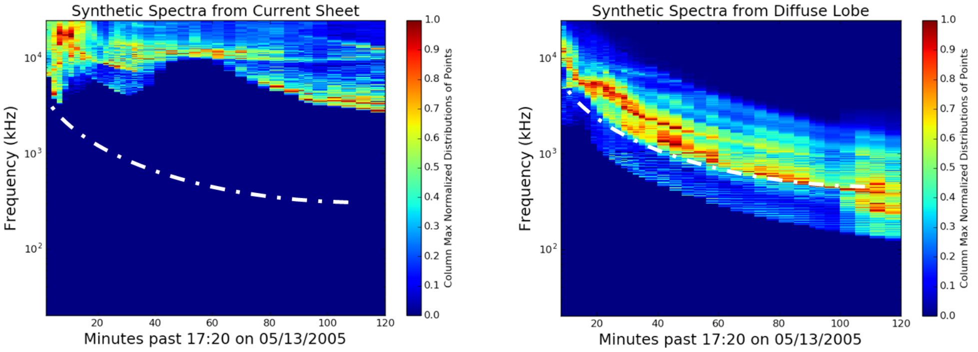

(c) Current Sheet Data Cut (d) Non-local Acceleration Data Cut

Figure 3.8: Synthetic spectra generated from datacuts near the shock front of the 2005/05/13 CME

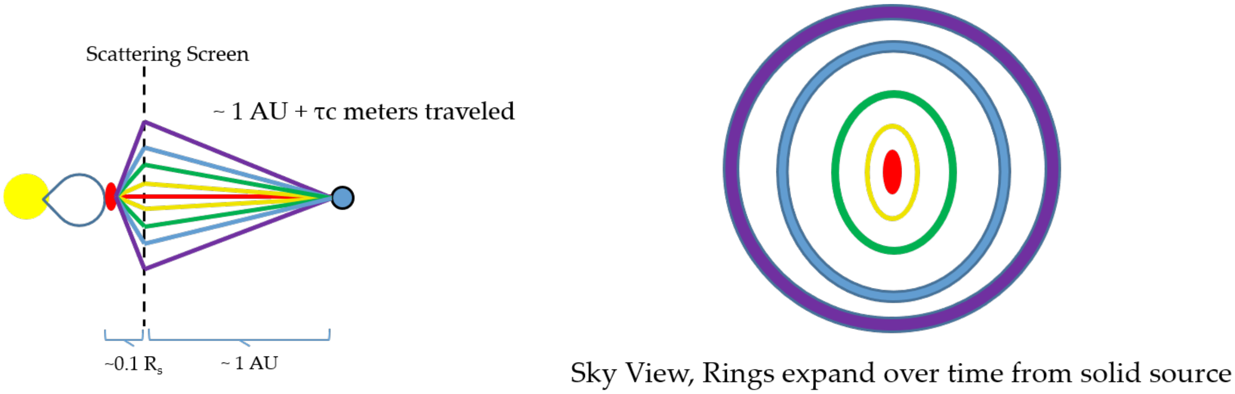

Figure 3.9: Cartoon plot of how scattering effects low frequency plasma emission

but to number of points with that particular frequency and time. This way we can bypass the exact physics that are creating the bursts, and only look to what areas of the CME most highly correspond to the actual frequency curve of the real data. These synthetic spectra for the 4 models of acceleration are seen in Figre 3.8.

We see that the shock front matches the actual frequency spectra best, matching the gradual downward curve in frequency over time. The current sheet spectra stays mostly in the high frequency portion of the figure, reflecting the fact that the current sheet stayed close in to the sun even as the flux rope driving the shock moved outwards. The shape of this emission roughly matches that of a solar type IV radio noise storm [63]. This may be proof that these radio storms originate from the current sheet formed behind a large solar shockwave. The shock flank synthetic spectra shows the correct general shape of the type II burst, but is far too wide. This could be a problem with the data cut being too inclusive, but it does mostly overlap with the correct spectrum. The non-local acceleration synthetic spectra is appropriately wide in frequency, and again seems to be too inclusive when comparing to the relatively thin bandwidth-frequency ratio (BFR) of the actual spectra.

3.6.1 Diffraction & Scattering

Diffraction and scattering are known to happen to solar radio bursts due to the fact that the plasma around the site of generation is perfectly primed to scatter radiation of the surrounding plasma

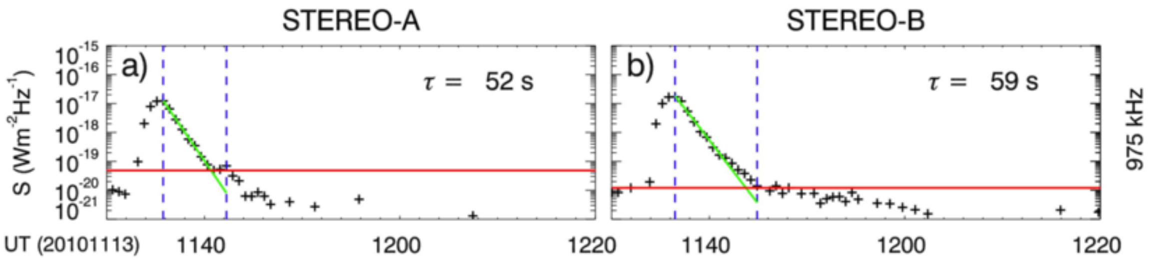

Figure 3.10: Taken from [7] this figure shows a single 975 kHZ channel of STEREO A and B. The exponential decay time in flux of a type III burst can be used to estimate the size of the scattered emission in the sky.

frequency. Once the radiation travels outward from the sun to areas of less dense plasma, the local plasma frequency decreases, and the radiation is free to continue in its current path with little more deflection. This effect means that one can model the scattering effects with a scattering screen, as described by Bastian in [64]. This effect is captured in the cartoon shown in Figure 3.9.

One can look at the exponential decay time of type III bursts and assume a simple model to gauge the extent of the scattering. This exponential decay time is shown in Figure 3.10, which shows the power received in a single channel both in STEREO A and B, and how it exponentially decays once reaching its peak.

Taking only singly scattered photons into account, from the cartoon in Figure 3.9, a simple relation may be derived that the Gaussian width of the scattered light Θ from a point source that has flux with an e-folding time τ is

$$\Theta \approx \arctan\left(\frac{\tau c}{1\ \mathrm{AU}}\right) \approx \frac{\tau c}{1\ \mathrm{AU}} \tag{3.16}$$

This approximation is good for $\tau c << 1$ AU, which is true down to about 0.3 MHz. Using this formula, one will expect a scattering width of $\Theta = 6.8°$ at τ = 60 sec at 1 MHz. Therefore, with a 1.0 second time resolution, a point source at 1 MHz in the Solar wind would appear to be .113 degrees wide. This would be a good physical justification for setting engineering requirements for an array that would image this emission. We could use this result to inform input truth data and evaluate the array’s performance in reconstructing the emission. This is just the sort of thing I will do in the next chapter for the SunRISE array.

CHAPTER 4

Operational Pipeline Design for Free Flying Radio Interferometers

4.1 SunRISE Overview

The Sun Radio Interferometer Space Experiment (SunRISE) mission concept is a low-cost mission (< \$55M for Phase A-E, including launch costs) that was proposed to NASA's Heliophysics Small Explorer (SMEX) Mission of Opportunity (MoO) program and was selected for a Step 2/ Phase A one-year study in September 2017. SunRISE would be a space-based interferometer composed of a passive formation of six SmallSats in an orbit just above the geostationary orbit (GEO), called a GEO graveyard orbit. The spacecraft would detect Type II and III radio bursts, which are associated with Solar Energetic Particles (SEPs) accelerated into space by solar flares and Coronal Mass Ejections (CMEs). Despite their importance in understanding our Sun and predicting the dangers of potential solar storms, these processes by which SEPs are created and travel through our solar system are poorly understood.

The SunRISE mission concept has recently been described at a high level in [29] and [27]. Most of this chapter through 4.3 will be taken from [39]. ©2019 IEEE. Reprinted, with permission, from Hegedus et al., The Data Processing Pipeline and Science Analysis of the Sun Radio Interferometer Space Experiment, 2019 IEEE Aerospace Conference. This chapter goes into more detail in the data processing and science analysis that would be done for the real mission. A high level view of the steps taken for testing and analysis is seen in Figure 4.1. We have constructed a pipeline to do these steps, and have tested it with realistic simulations. We go step by step in the pipeline, showing how we go from input data that the spacecraft will send down, to the final science data products, along with all intermediate steps taken. The test Decametric-Hecametric (DH) radio data has been informed by state of the art Magnetohydrodynamic (MHD) simulations of a real Coronal Mass Ejection from 5/13/2005 that was radio loud [62] over SunRISE's range of $2 - 20$ Solar radii. The model used is the University of Michigan Alfvén Wave Solar Model (AWSoM) [60]. This model takes in Solar Magnetogram data and solves for an global model of the upper chromosphere to the corona and the heliosphere. It has advanced physics such as separate electron and ion temperatures that allow it to reproduce general features of CMEs and other solar output.

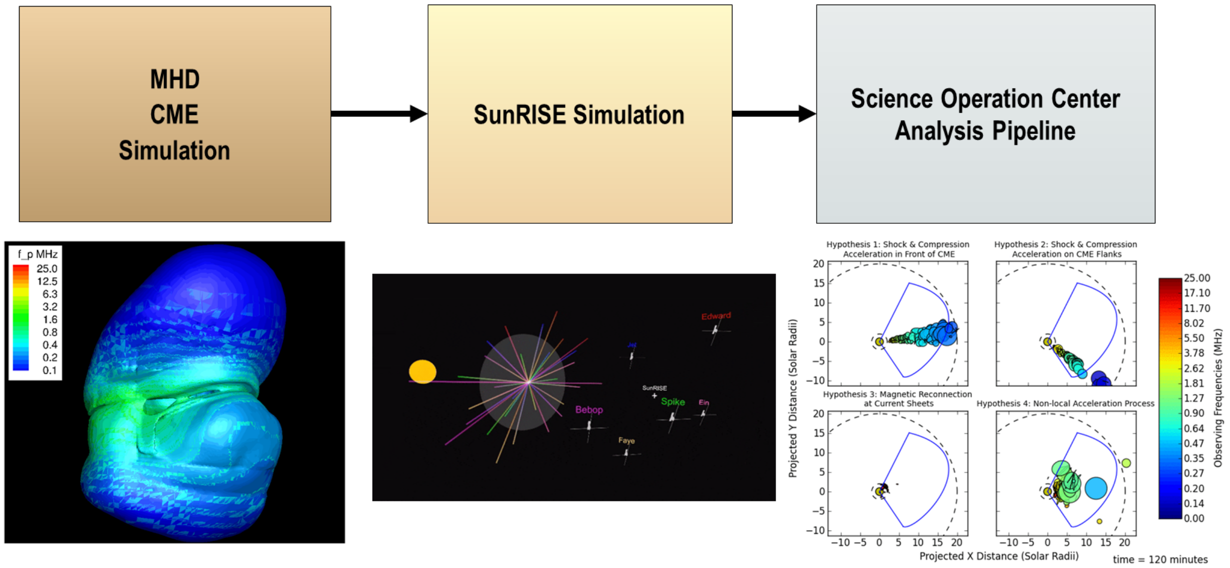

Figure 4.1: High Level Overview of the Data Processing in Testing the SunRISE Pipeline

We test different hypotheses by applying different cuts to the data for every moment in time, identifying possibilities such as the evolution of the nose of the shock, or the CME's flank, or its current sheet. The MHD simulations compute parameters of the plasma at these areas, including the plasma frequency, which would be the frequency of radio emission emitted there if it was the source of particle acceleration. A frame of these simulations may be seen in the left panel of Figure 4.1. These simulation driven radio brightness models are then input to the simulation of SunRISE.

The middle panel of Figure 4.1 shows a simulation of the SunRISE orbit, and how that moment in the formation leads to a particular set of spacecraft spacing in plane normal to the Sun-SunRISE line. These separations determine the exact response of the array, and affect how well the array can fit the emission to a Gaussian.

The processing done on the ground, mostly at the Science Operation Pipeline are indicated by the right panel of Figure 4.1. The accompanying figure shows an example of the SunRISE reconstructions over time and frequency for different emission hypotheses. We will describe how this figure is generated, and how it shows that SunRISE can complete its mission in discerning between various hypotheses of type II burst generation.

It is found that SunRISE has the ability to successfully discern between different possible sites of type II burst emission. This by extension means it can also map type III radio emission, which is an order of magnitude brighter, and comes from flare accelerated electron packets as opposed to CMEs.

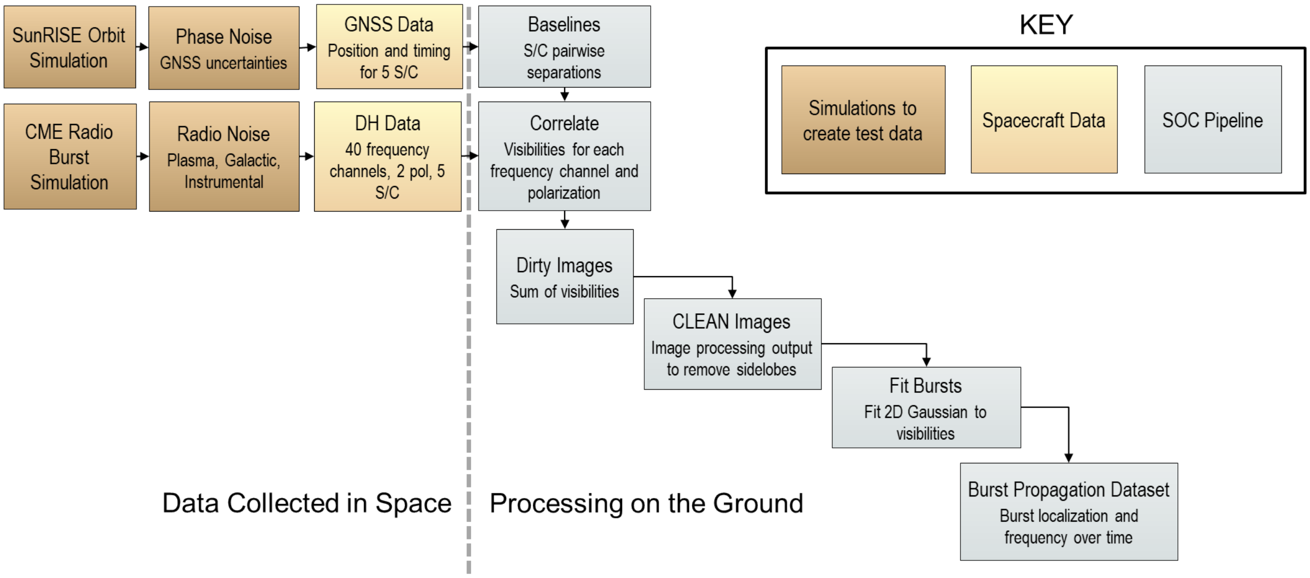

Figure 4.2: Detailed View of SunRISE Testing Pipeline

4.2 Simulating SunRISE

Most radio interferometry simulation software depends on the measurement equation, where Jones matrices are used to represent the measured voltage and sky brightness for a given baseline and model the noise effects happening to it with different operations on the matrix. Thermal noise is added directly to the brightness matrix, but for all other effects such as modeling the gain and phase errors the brightness matrix on the left and right are multiplied with the conjugate transposes of the transformation matrices. The resulting matrix is the voltage matrix which models what the actual measurements will be.

The level of system noise in the Solar DH radio signal chain was calculated from the Galactic background, the antenna plasma noise, and the characteristics of the instrument. Signal strengths were estimated from previous single antenna observations of type II events from Wind and STEREO. To calculate the root mean square, RMS, on the Gaussian thermal noise to add, one usually looks at the levels of different instrumental sources of noise as described in classic texts [2]. In this frequency range, the galactic noise is the major limiting factor. We used Cane's 1979 measurements in [65] to get the T_{sys} temperatures from the frequency dependent galactic noise, which is turned into noise RMS using the following standard formula:

$$\sigma = \frac{2k_B T_{sys}}{\eta_s A_{eff}\sqrt{N_a(N_a-1)N_{pol}\tau\Delta\nu}} \tag{4.1}$$

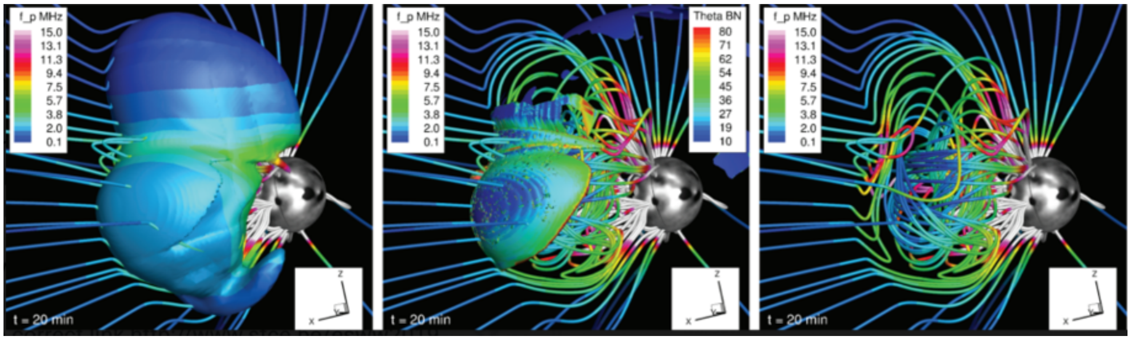

Figure 4.3: Snapshots from a AWSoM 2-Temperature MHD Simulation of a Radio-Loud CME on May 13, 2005

4.2.1 Antennas and Noise

4.2.2 Orbits

We have constructed a simulation of the orbits of the spacecraft (S/C) for the notional SunRISE orbit. For a specific realization, we sample the instantaneous positions of the S/C at a given time in the orbit or orbital phase. These positions are taken as truth positions. Orbit simulations were done with the JPL Mission Analysis, Operations, and Navigation Toolkit Environment (MONTE) [66], which has been successfully leveraged on many S/C, including Cassini, Mars Science Laboratory, and Juno. The orbits created are represented in the middle panel of Figure 4.1. The lines on the circle represent the projected baselines to the plane perpendicular to the Sun-SunRISE line. These projected separations are important, and will be used later in the pipeline to simulate the synthetic beam of the array.

Using models of the GNSS sidelobes and expected signal strengths at the SunRISE altitude, we generate a set of (3-D) position and timing uncertainties for each S/C. These values were given by the GNSS-Inferred Positioning System and Orbit Analysis Simulation Software package (GipsyX) [37]. This software has been successfully leveraged for many Low Earth Orbiting missions such as Jason-1, Jason-2/OSTM, and GRACE. Specifically, spacecraft can record carrier phase and pseudo-range data from any GNSS satellites they can see (usually at least 2, from GEO graveyard orbits, per SunRISE analyses). There are 2 levels of GPS solutions for space based radio arrays. One is to have Real Time Gipsy (RTGx) running on all of the spacecraft, this gives an approximate location to within 22 ns that is good enough to synchronize the taking of data between the duty cycles of all the spacecraft.

The next level is using GIPSY/OASIS-II (GOA-II) software, or its modern iteration GipsyX, to do post processing on the GNSS data to solve for even more precise locations down to 2 nanoseconds. For SunRISE, this post-processing is done on the ground, and the accurate spacecraft positions are then used for further science processing.

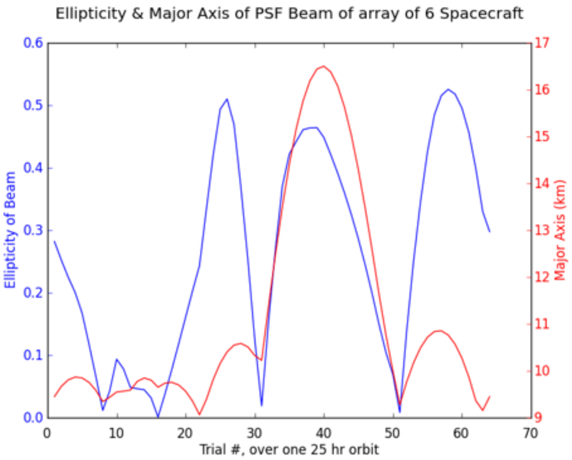

Figure 4.4: This plot shows the ellipticity of the instantaneous beam of the current configuration of the spacecraft. It is a measure of how the similar the distance between the Eastern and Western most receivers, and the distance between the Northern and Southern most receivers. Configurations of the spacecraft array with equally long separations in both directions has an ellipticity of 0. The major axis is the longer of the 2 directions, and can be used with the ellipticity to solve for the minor axis.

.

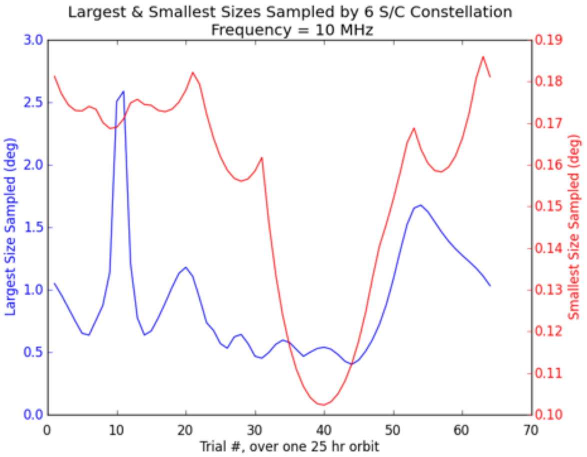

Figure 4.5: This plot shows the relative scale sizes on the sky that SunRISE is sensitive to at 10 MHz over the course of its nominal 25 hour orbit. These scale sizes are proportional to the wavelength of the observing frequency.

.

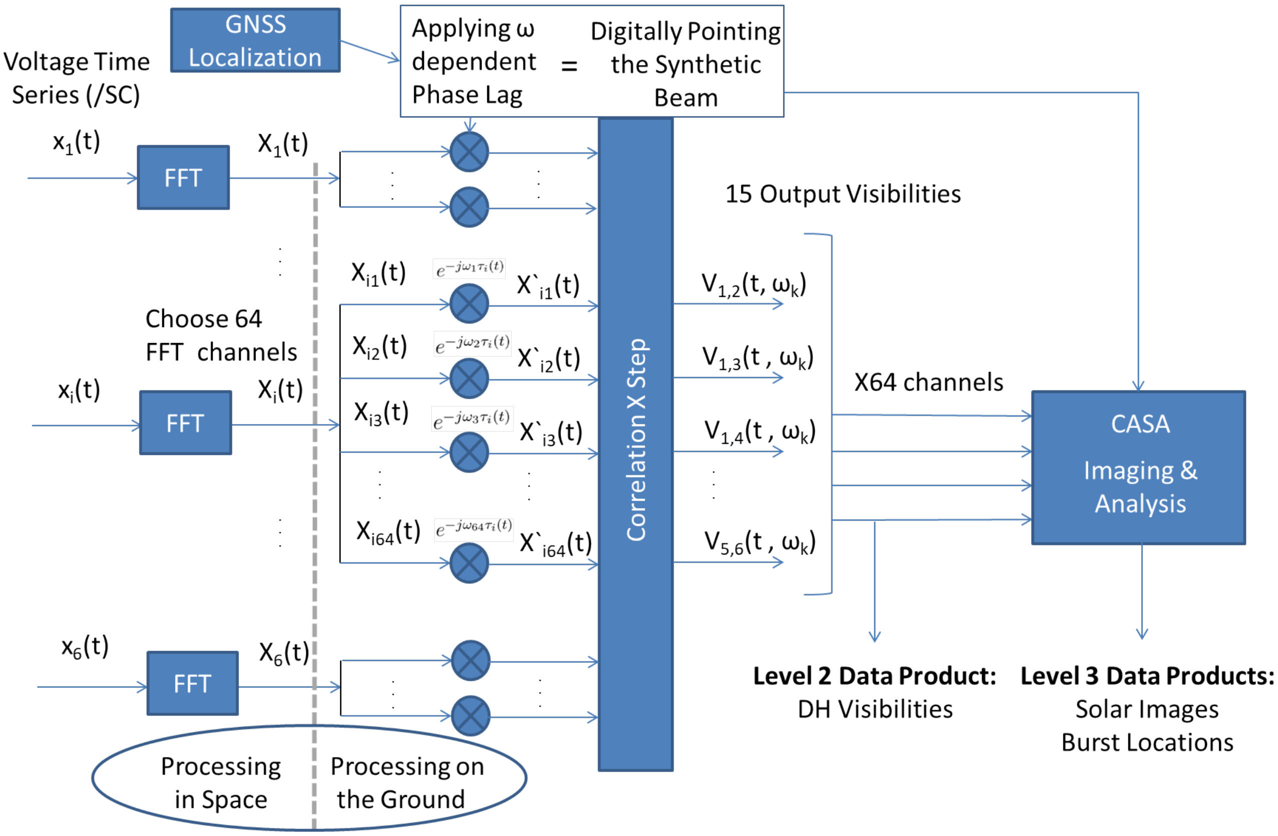

Figure 4.6: Flowchart Showing the Correlation Process for Space Based Array SunRISE

4.2.3 CME Radio Burst Simulation

The 2-temperature AWSoM model was used to simulate the first two hours of the 2005 May 13 CME event that produced a sustained type II radio burst. For each test, a specific region of the CME corresponding to one of the hypotheses under consideration (e.g., shock front or flank) was stimulated to produce radio emission at the local plasma frequency. The locations of these radio emissions in the sky as a function of frequency were used to construct truth images over the course of the event. These images were made for each 6.1 kHz frequency bin to match SunRISE's frequency resolution.

These MHD simulations reveal a lot about the plasma parameters of different regions of the heliosphere at the time of the event. Some are shown in Figure 4.3, though there are many correlated plasma parameters with type II burst observations [57], including de Hoffmann-Teller frame velocity and shock speed. Each parameter may be computed and used to cut the data in some way.

Figure 4.3 shows 3 panels at 20 minutes into the simulation; the left panel shows magnetic field lines colored for the plasma frequency of the region as well as a diffuse density enhancement from the event like wise colored by plasma frequency. The middle panel similarly shows magnetic field lines colored for plasma frequency, but also a entropy-jump determined shock that has been colored for the angle between shock normal and the upstream magnetic field (Θ_{BN}). The right panel shows only the magnetic field lines, demonstrating how the buildup of magnetic field is driving the event out from the sun. In addition to generating useful test data, MHD simulations will also help to inform the actual measurements of SunRISE, pointing to specific plasma parameters that are past certain thresholds at the site of the type II. The simulated velocity at Earth matches real corresponding observations of 1600 km/s, lending trust to the model.

4.3 Simulated Science Operation Center Pipeline

4.3.1 DH Data

DH Data: A set of at least 40 frequency sub-bands (channels) for the baseline mission are selected for further processing. The plan is to transmit to the ground 64 channels/0.1 second, giving a full sweep of the 4096 channels every 6.4 seconds. Data transmissions would be done on a weekly basis. In our test pipeline, each frequency sub-band's truth signal was corrupted by adding the appropriate level of system radio noise from thermal considerations and positional uncertainty in the GNSS measurements.

To get the proper simulated measurements from the input truth images $I(l, m)$, we used the simpler 2-D interferometry equation [2] to solve directly for the visibilites. This is justified because the only part of the sky SunRISE cares about for its main science is that near the Sun, and it only cares about imaging solar radio bursts which are by far the brightest things in the sky when they

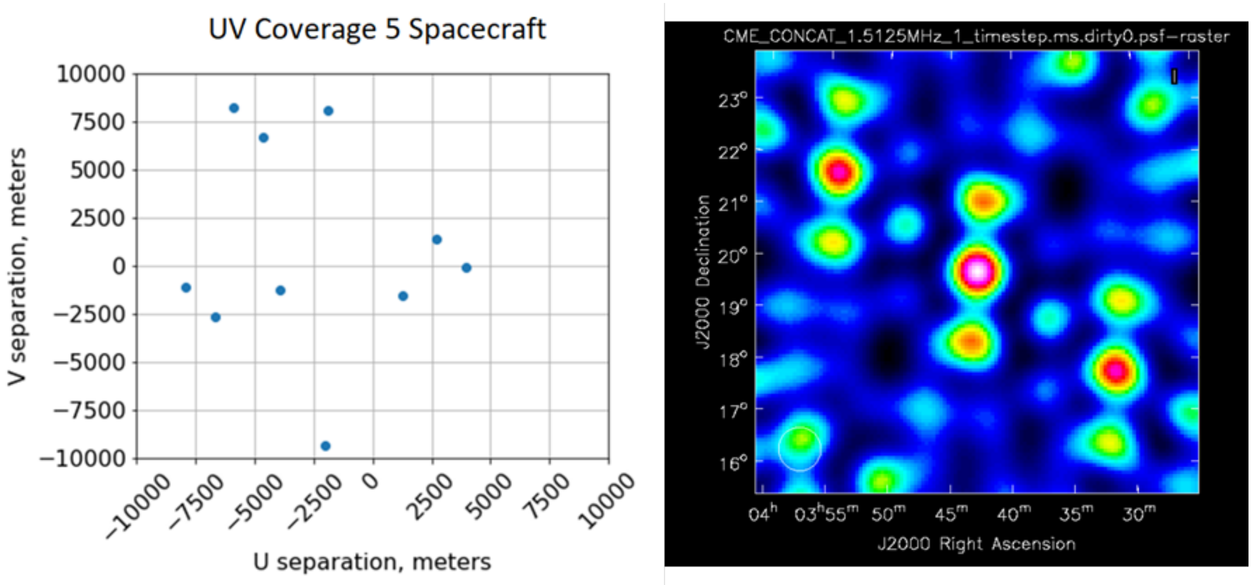

Figure 4.7: *Left*: UV Coverage of a 5 S/C SunRISE *Right*: The Point Spread Function for this Snapshot

happen. This allows us to make a 2-D assumption based off of this.

$$V_\nu(u,v) = \int\int \frac{A_\nu(l,m)I_\nu(l,m)}{\sqrt{1-l^2-m^2}} e^{-2\pi i(ul+vm)} dldm \tag{4.2}$$

This provides the visibility for each pair of spacecraft, from which the corresponding phase differences between receivers may be calculated. These radio visibilities are later used for imaging.

4.3.2 Baselines (S/C Pairwise Separations)

The following set of steps replicate the processing that will occur following the transmittal of the data to the SOC. The unique S/C pairs are identified, and their simulated positions (i.e., including the level of position uncertainties expected from the GNSS analysis) are used to construct the antenna separations. These antenna separations are then converted to spatial frequenciesu-v coordinatesby dividing by the appropriate wavelength corresponding to each frequency sub-band. An example of instantaneous UV coverage for a five-element SunRISE array is shown in Figure 4.7.

4.3.3 Correlate (Visibilities)

The simulated/real DH data from each S/C are cross-multiplied, and then the metadata of the u-v coordinates and frequency are added to form Measurement Sets in the standard format. More details are shown in Figure 4.6 showing the correlation process for SunRISE and the location of Science Data Products in the pipeline. The process begins with a Fourier Transform (F step) of each of the antennas voltage time series data in space, of which 64 frequency channels are sent down to the ground. There, the channels are treated with a frequency dependent phase shift calculated from the projected distances between receivers. The model takes in ECEF coordinates from GNSS localization data, along with a target in the sky, given by an ephemeris for the Sun, and computes the necessary phase delays to correctly correlate the data. This conversion from the ECEF frame to the ECI sky frames is standard and has equations defined to do so in [40]. Adding in the proper phase delays effectively steers the synthetic beam to point at the Sun. Each Fourier coefficient is then pairwise multiplied (X step) to obtain the radio visibility data, which is a Level 2 Data Product. These visibilities and S/C positions are then sent to a CASA script for further analysis to create the Level 3 Data Products, solar images and burst locations.

A parallel correlator has already been created at Michigan using the xGPU software that can perform the X step of the FX correlation process faster than real time (64 channels 5 S/C 10/s)

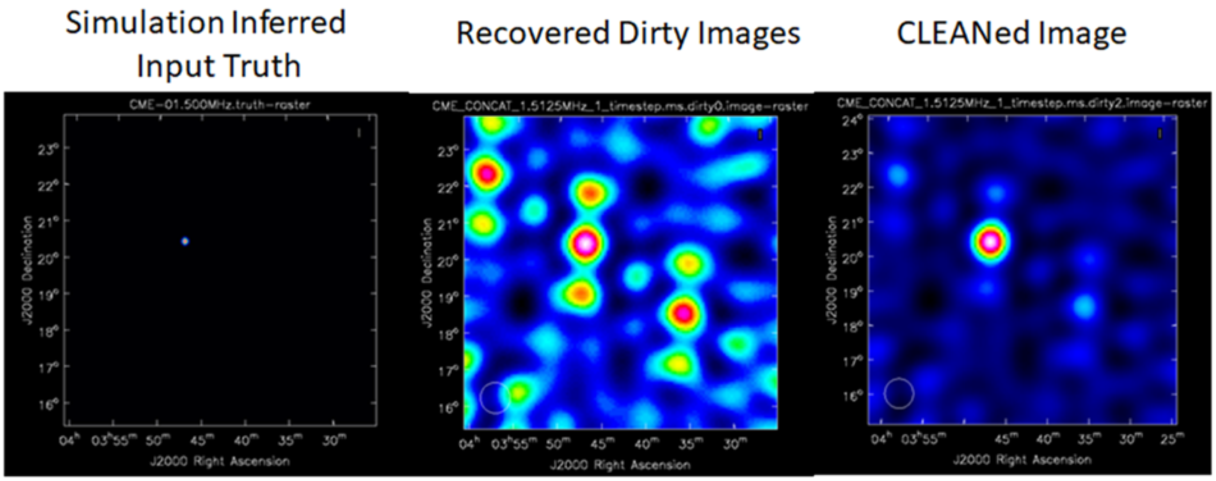

Figure 4.8: CASA Imaging Pipeline going from Input Truth to Dirty Image to CLEANed Image

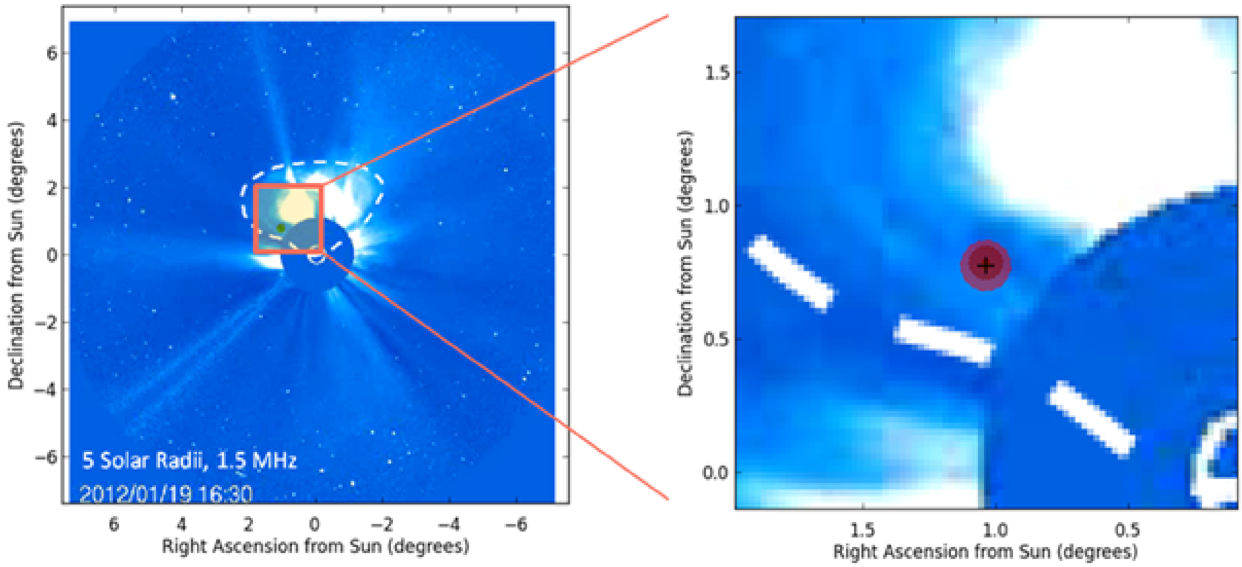

Figure 4.9: 2D Gaussian Fit from uvmodelfit at 1.5 MHz

for the SunRISE array. The correlator correctly phases up the DH data for each frequency channel and outputs the visibility data.

4.3.4 Dirty Images

The visibility data are Fourier inverted, using standard routines contained in the astronomical software package CASA [24], pictured in Figure 4.8, producing dirty images for each frequency sub-band. An important step in producing these data includes computing the dirty beam of the array, also called the point spread function (PSF). The spacing of the antennas decides the shape of the array's synthetic beam, creating a wavelength dependent pattern also called the point spread function (PSF). An example of the SunRISE PSF is shown alongside its UV coverage in Figure 4.7.

4.3.5 CLEAN Images

The dirty images are processed using the standard CLEAN algorithm [67], in order to remove the effects of the point spread function (beam). These images are produced for each frequency sub-band. An example of a CLEANed image is shown in Figure 4.8.

4.3.6 Fit Bursts

The width of the CLEANed image shows the width of the beam at that frequency, but due to our expected signal to noise ratio (SNR) of >10, SunRISE can actually localize to a higher degree than expected from a basic λ/D beamwidth calculation. We can take the position of the brightest point in the CLEANed image as a starting point for a CASA native iterative fitting algorithm uvmodelfit that fits the visibility data to a 2D Gaussian on the sky. This fitting algorithm outputs RA & Dec in the sky, total brightness, major axis, minor axis, and position angle, and predicts a shape far closer to the smaller truth emission. Figure 4.9 shows a reconstructed Gaussian on top of a LASCO coronagraph image of a CME. The right is a zoomed in portion of the left, where we have plotted the input truth in black and the reconstruction in red. The reconstruction is directly on top

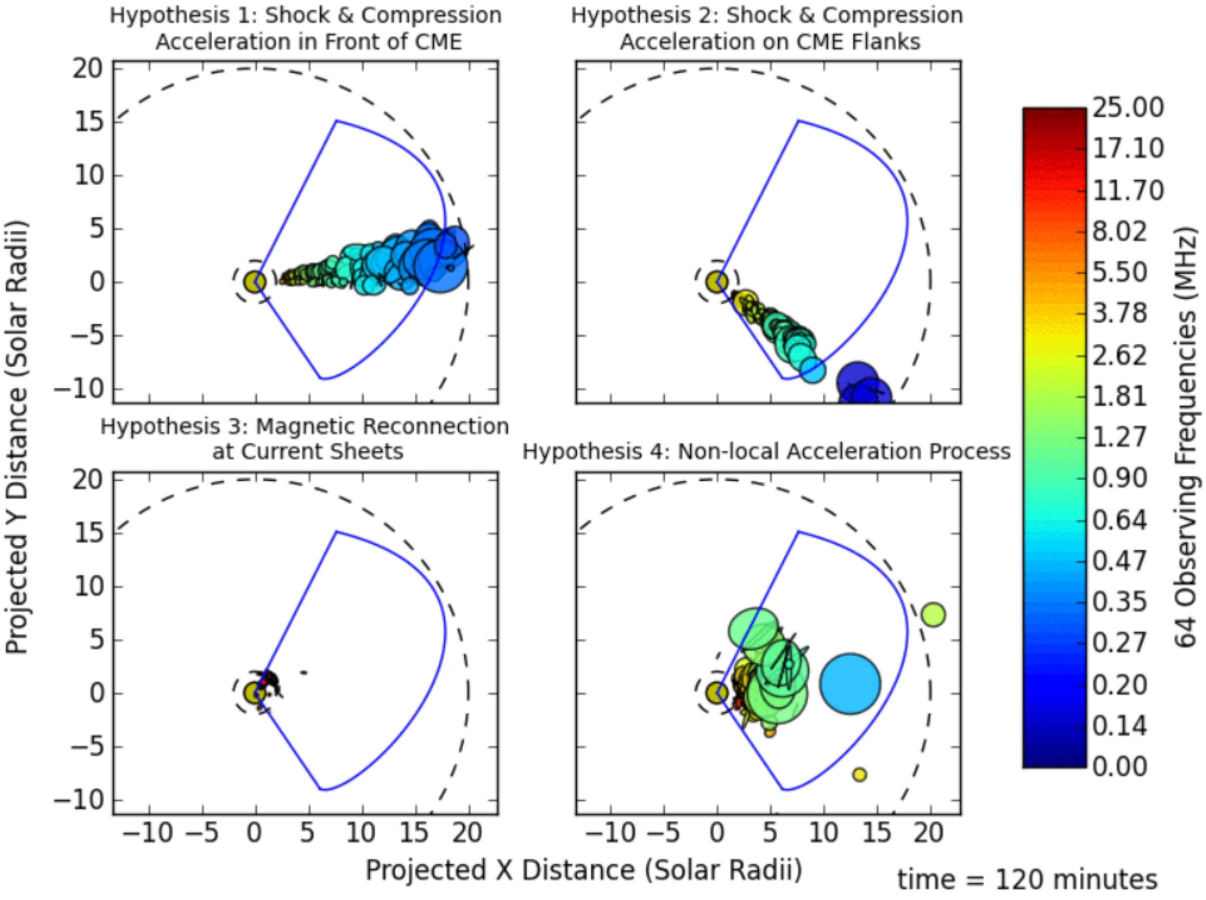

Figure 4.10: SunRISE Reconstructions of 4 Different Type II Emission Hypotheses

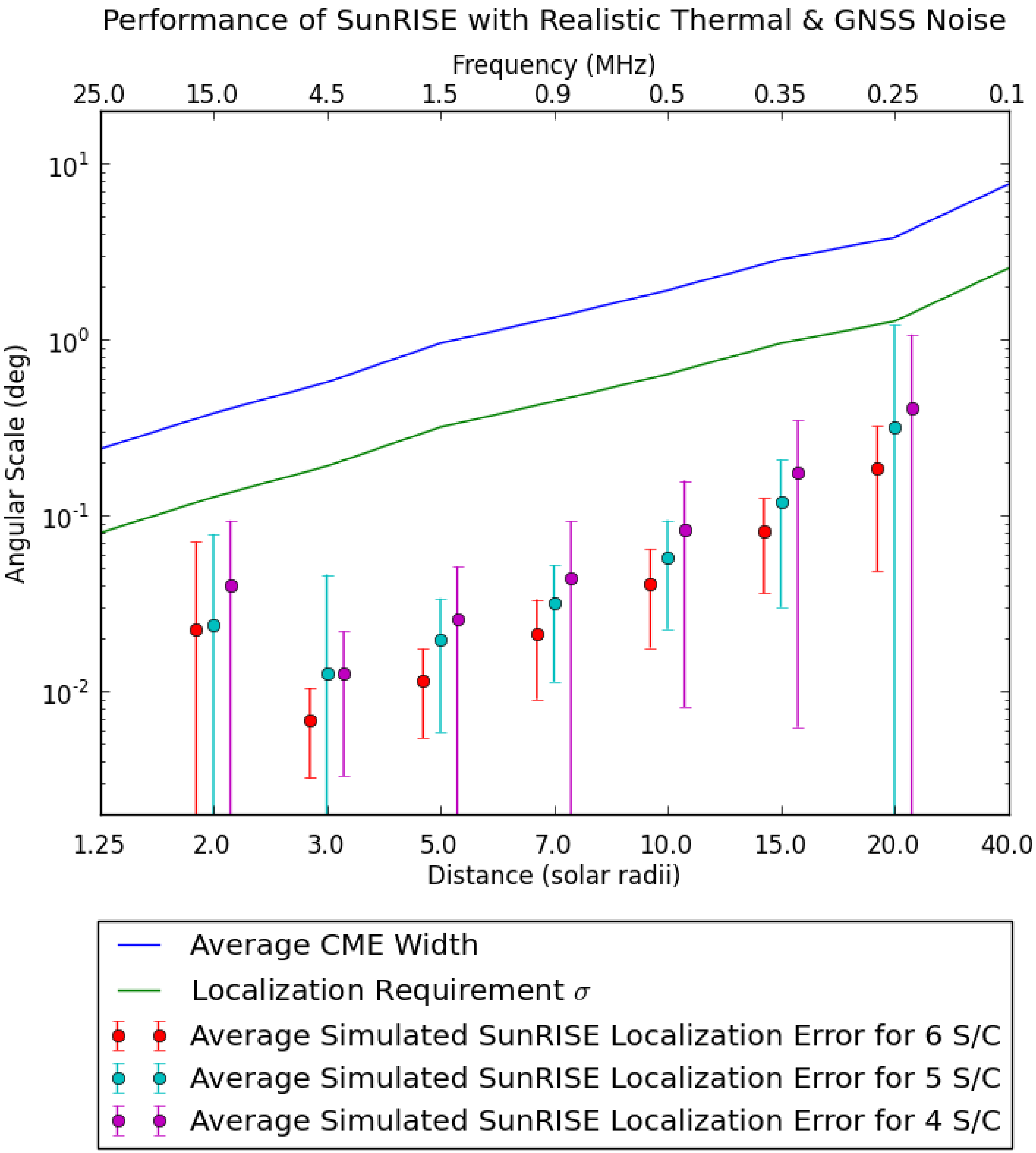

Figure 4.11: Realistic Localization Performance of 4, 5, and 6 Spacecraft in the SunRISE Array

of the truth and only slightly larger. The black bars over the reconstruction on the right represent the average localization error expected from 80 instances of the testing pipeline. The size of the emission is visibly smaller than the beamwidth seen in Figure 4.8. The total set of fit radio bursts over frequency and time will be released to the public as a Level 3 Data Product.

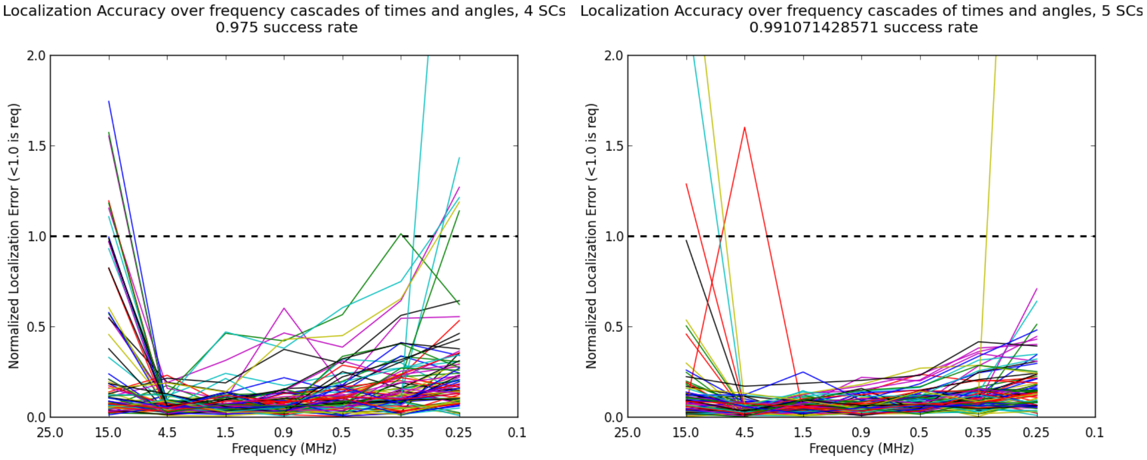

(a) 4 Spacecraft Event Localization Success

(b) 5 Spacecraft Event Localization Success

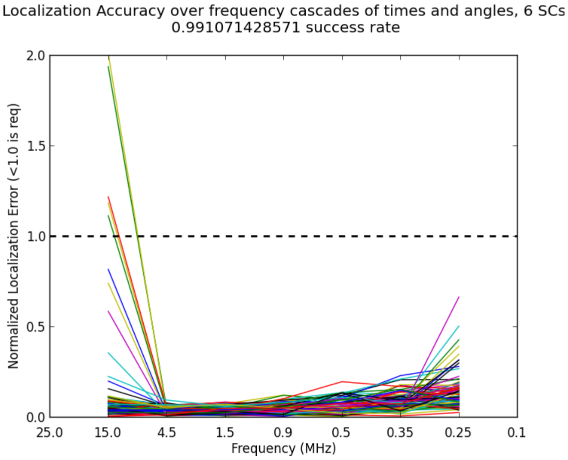

(c) 6 Spacecraft Event Localization Success

Figure 4.12: Localization Success Rates

4.3.7 Pipeline Testing

To test the SunRISE science pipeline, state of the art MHD simulations were done to track various aspects of a 2005/05/13 CME all the way from $2 - 20$ solar radii, SunRISE's operating range. Radio emission whose frequency and shape was derived from the MHD data was modelled on top of various parts of the shock over time and fed into the analysis pipeline to see if it can distinguish between the various hypotheses for Type II bursts. Figure 4.10 shows the result of this test, demonstrating that SunRISE provides a first of its kind measurement that can clearly see the difference between competing hypotheses for type II burst generation. The blue curve is a smoothed representation of the shock of the CME. The dashed lines are at 2 and 20 solar radii, SunRISE's operating range. The morphological differences in the path traced out over time both in sky position and frequency provide a unique view to distinguish between competing hypotheses for type II burst generation.

Not biasing our testing by only analyzing a single event, we have run this localization analysis pipeline throughout 10 places in SunRISE's orbit, each testing CMEs going out at eight different propagation angle locations for seven frequencies to come up with an average localization error. The mean error and root mean square of the errors are shown in Figure 4.11 for all frequencies, showing that we meet the localization requirements.

One may also look at the data for each simulated CME to see if it was localized sufficiently over its entire emitting range. In Figure 4.12, each line corresponds to a single time in the orbit and a propagation angle of the CME. By looking the localization performance over frequency for each event, one can see that even if a single snapshot did not correctly localize to the true source, it is easy to fill in any holes by looking at all the other snapshots at different frequencies of the event together. In this way SunRISE shows robustness to any single faulty localization, and can rely on the sheer number of snapshots over time and frequency to create a continuous map of where the type II is coming from with reference to the CME. Of the 80*7 = 560 reconstructions over various frequencies, times in the orbit, and CME propagation angles, over 99% succeed for 5 and 6 S/C, and 97.5% succeed for the threshold mission of four S/C.

The bottom line obtained from 560 reconstructions over various frequencies, times in the orbit, and CME propagation angles, is that with 5 or 6 spacecraft SunRISE meets its localization requirements more than 99% of the time, and the threshold mission of 4 spacecraft meets its requirements 97.5% of the time. As seen in Figure 4.10, this means SunRISE has the ability to map where type II bursts are coming from, and when combined with Coronagraph images and MHD simulations, can answer the question of where on a CME they are being generated. This in turn will reveal where solar energetic particles are being accelerated in CMEs, an important result for space weather prediction.

4.4 Extended Science for SunRISE

SunRISE also has the capabilities of measuring several other bright radio sources in the sky. These would be the first such measurements of the bodies in these low frequencies, and would lay the groundwork for larger arrays such as RELIC that would have even more sensitivity and resolution. Due to constraints in telemetry, the instrument acquires 0.66 ms of data every 100 ms and only saves 64 out of the 4096 frequency sub-bands (6.1 kHz each) in the spectrum. The snapshot sensitivity for each acquisition is $\sqrt{T}_{\mathrm{int}\Delta\mathrm{f}} \simeq 2$. For radio astronomical imaging, the data will be integrated over longer periods of time but with a duty cycle of 0.66%. As stated before, the Solar radio bursts that are SunRISE's main science are by far the brightest things in the low frequency sky when they occur, which is why a relatively small mission is sufficient. Only the brightest and closest things in the low frequency radio sky are estimated to be bright enough to detect over SunRISE's lifetime.

4.4.1 Sensitivity Estimates

The main noise budget of SunRISE is composed of 3 main factors: amplifier noise, galactic noise, and plasma noise. As seen in Figure 4.13, at some point within the operational bandwidth of SunRISE, each of these sources become the dominant term. Therefore understanding the frequency

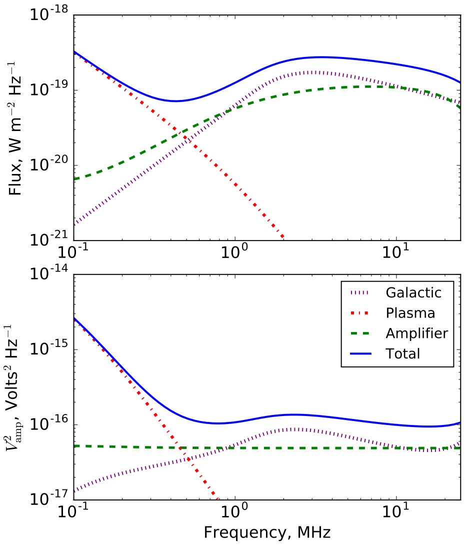

Figure 4.13: *Top:* Background fluxes and *Bottom*: the equivalent noise voltage spectrum in the front-end amplifier. for a 5 meter full-length dipole and a $Z_L \simeq 12.8\ \mathrm{k}\Omega$ front-end impedance. The amplifier noise is based on a model of the OPA656 provided by the manufacturer. The Galactic noise uses the model of Cane 1979. The plasma noise model is from Meyer-Vernet & Perche 1989 as implemented by Zaslavsky et al. 2011 for modeling the performance of the STEREO/WAVES instrument.

dependence of each source is critical for accurate sensitivity calculations.

We have extended the regular SunRISE pipeline, usually just meant for snapshots, so that it can integrate over the entire orbit to produce a longer exposure picture of the sky. The SunRISE orbits are designed so that at any given time, there is a pair of baselines with $\geq$ 6.5 km separation in the projected plane normal to the array and the Sun. Note that the array is not coplanar so it is expected that this condition will be met, with perhaps a few exceptions, in any given direction although it is only required in the direction of the Sun. Among the few bodies expected to be detectable are Cygnus A, Centaurus A, and Virgo A. All of these are radio galaxies that are among the brightest in the sky, but SunRISE doesn't have the resolution to resolve them to more than a point source, so the mapping that can be done is limited. In the case of Cassiopeia A, there may be some useful science that simple low frequency flux measurements could accomplish, as described in the following section.

Just as for ground based arrays, integration of a space based array also leads to a better syn-

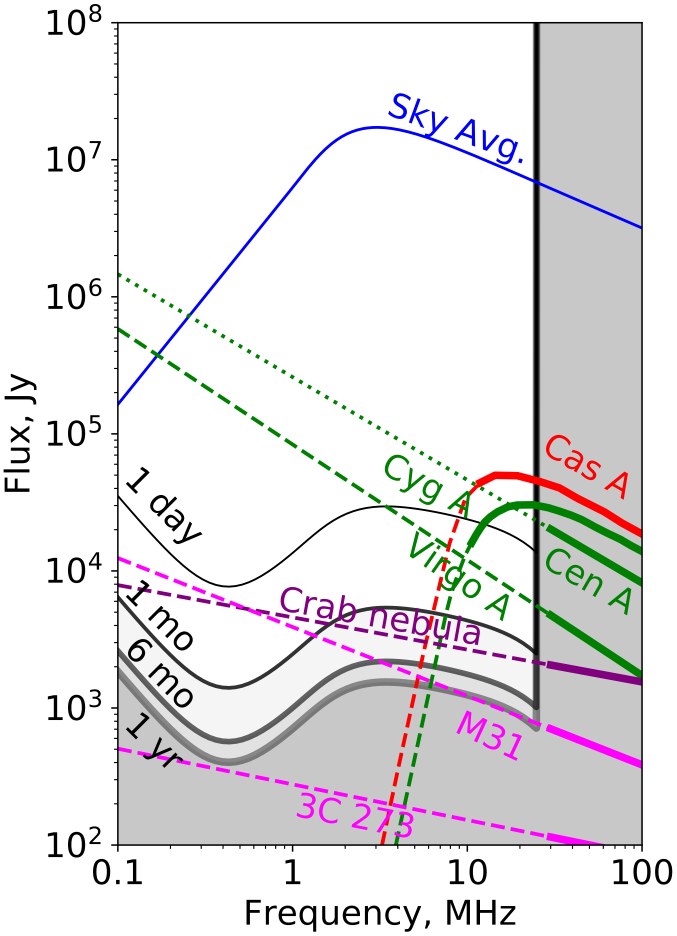

Figure 4.14: SunRISE sensitivity various integration times (1 day to 1 year in increasing line thickness) compared to extrapolated fluxes for the brightest objects in the sky. Shaded regions below each sensitivity line indicate fluxes not detectable by SunRISE. The sky average is from Cane 1979. The integrated Centaurus A flux is from Alvarez et al. (1999), A&A 355, 863. The rest of the fluxes are obtained from Kraus's Radio Astronomy textbook.

thesized beam with more sampled baselines. Figure 4.15 shows the progression of the 5 MHz synthesized beam as SunRISE integrates over an entire orbit. One can see that in panel a), there are significant sidelobes that decay as we increase the integration time to 2 hours in panel b), and disappear entirely into a $\approx 5\%$ rms variation outside the main lobe after 24 hours in panel c). Figure 4.16 shows the integrated synthesized SunRISE beam after 24 hours from 3 different angles in the sky. This shows how the synthesized beam is similarly good at any angle in the sky, a result of the orbital design that is evenly spread across 3 dimensions.

4.4.2 Supernova Remnant Cassiopeia A

It is widely accepted that radio emission from supernova remnants (SNRs) is due to synchrotron radiation. However, it is still debated whether electrons are accelerated by Fermi processes caused by turbulent wakes generated in the surrounding medium by the motion of fast-moving knots [68] or by turbulence generated through hydromagnetic instabilities [69] [70]. Low frequency images of the Supernova remnant Cassiopeia A (Cas A) could reveal the locations and evolution of particle accelerating regions. However, Cas A spans ~ 5.3 arcminutes, which is not resolvable with the SunRISE array. The simulated performace of SunRISE as it integrates an image of Cas A is seen in Figure 4.17

Another potential way to probe the behavior of particle acceleration is by obtaining a time series of fluxes at low frequencies. Analysis of 51 years of data from Cas A have shown that the flux at at 38 MHz has up to 4 modes of oscillation with frequencies of 24, 9.9, 5.1, 3.1 [71]. At higher frequencies, a secular decrease in the spectrum is observed with no evidence of oscillations. It is not clear whether the parameters of the four-cosine fit are due to stochastic variations, but regardless, this behavior may hint at mechanisms such as the interaction of shock fronts with ejecta and the external medium. SunRISE will have the ability to monitor the fluctuations of the spectrum at lower frequencies almost continuously (except of occultation of the Earth and Sun) during the nominal mission duration of 1 year and possibly longer with an extended mission. Although the duration of these observations is shorter than the modes of oscillation observed at 38 MHz, it is expected that the frequency of emission is proportional to the magnetic field strength and energy of electrons. It is possible that faster variations in the flux occur for for weaker shocks or turbulence that accelerate particles.

The best-fit frequency spectrum of Cas A from a study by Arias et al., 2018 [72] is shown in Figure 4.14. The low frequency cutoff is due to the presence of a molecular cloud in the line of site to Cas A. Based on these expectation, it will be possible to obtain daily flux curves above $\sim$7

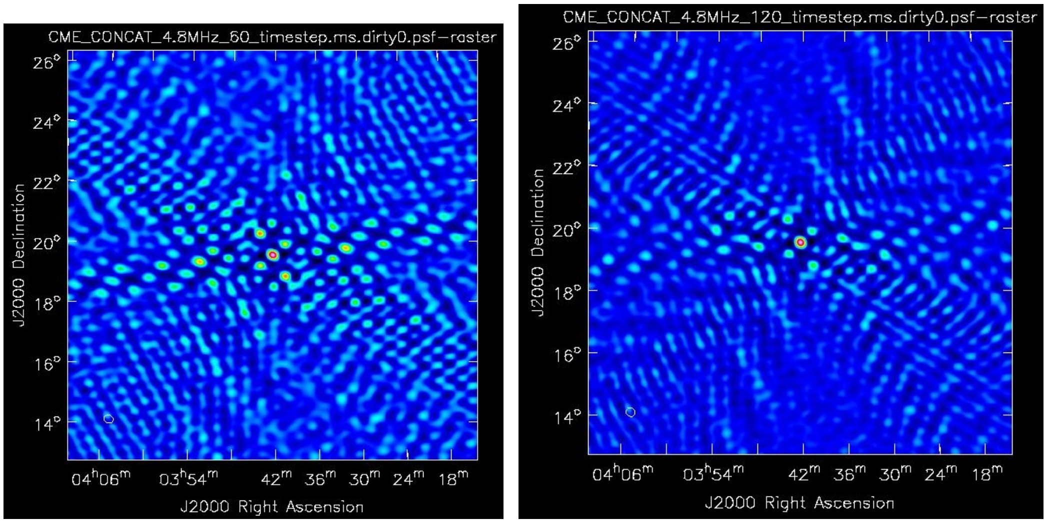

(a) 5 MHz Beam after 1 hour integration

(b) 5 MHz Beam after 2 hours integration

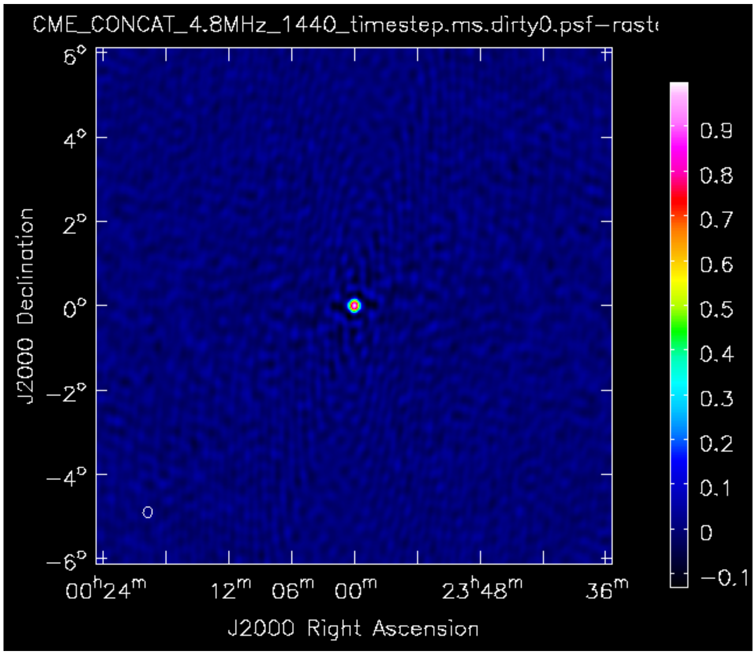

(c) 5 MHz Beam after 25 hours integration

Figure 4.15: Example of how the synthesized beam improves as integration progresses over the spacecrafts' orbit. All 3 panels here point towards the same point in the sky, the origin of the J2000 system.

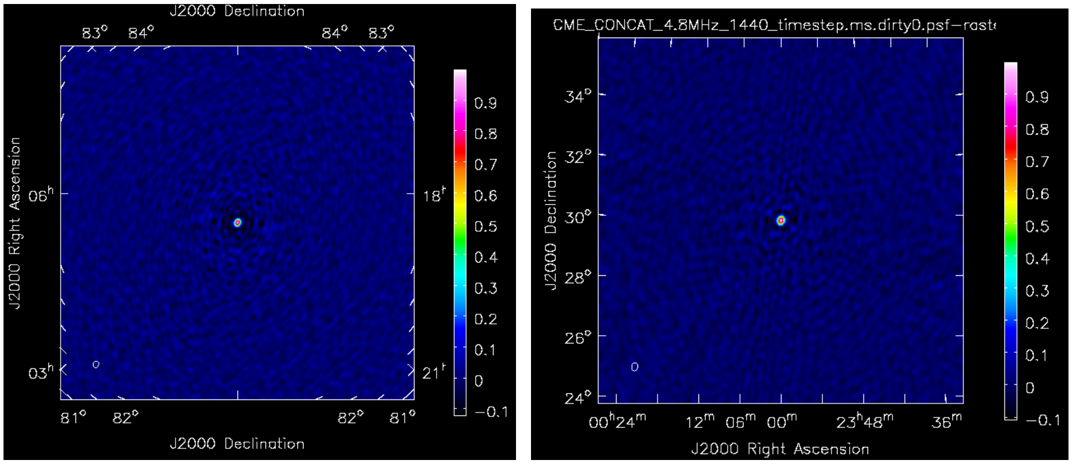

(a) 5 MHz Beam at 90° Declination

(b) 5 MHz Beam at 30° Declination

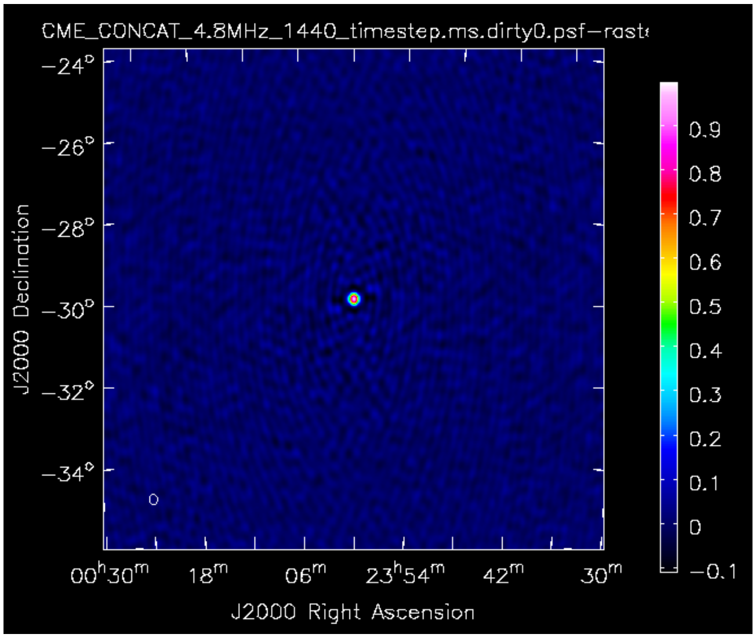

(c) 5 MHz Beam at −30° Declination

Figure 4.16: 24 Hour Orbit Integrated Synthesized Beams at different declinations in the sky. This shows how the synthesized beam is similarly good at any angle in the sky, a result of the orbital design that is evenly spread across 3 dimensions.

MHz up to ~20 MHz.

4.5 Low Frequency Astrophysics with RELIC

4.5.1 Mission Overview

Besides the few examples mentioned previously, most static objects in the low frequency sky are too weak to be detected with just a few antenna. We need many more antenna with much higher separations in order to get high resolution, high contrast images. SunRISE may be able to see only the brightest example of an astrophysical category, eg SNRs with Cas A and radio galaxies with Cygnus A and a couple others, but there are many more things in the sky waiting to be imaged at low frequencies for the first time. The 3CR catalogue [8] shows that there are many feasible radio galaxies to image, if only we had the resolution and sensitivity.

RELIC hopes to be the array that does this for the first time, using a mothership with 32 daughterships in a Lunar orbit. Each daughtership would have dual-polarization dipole antennas, similar to the SunRISE design. In a paper published in Experimental Astronomy in which I was a co-author [28], we sketched out many aspects of the mission concept. The tables and figures in this section are reprinted with permission from Springer Nature, Experimental Astronomy, A space-based decametric wavelength radio telescope concept, Belov et al., ©2018. In Table 4.1, the requirements for the orbits of the 32 spacecraft is shown.

4.5.2 DRAGN Science

Radio galaxies can frequently have large lobes of radio emission that are far larger than the galaxy itself. These lobes are thought to be from jets of energetic particles originating from the black holes at the galactic center. There is hypothesized to be a shockwave at the end of the jet that generates the cloud of emission. These bodies are called Double Radio sources Associated with a Galactic Nuclei (DRAGN). An example can be seen in Figure 4.20 panel a.

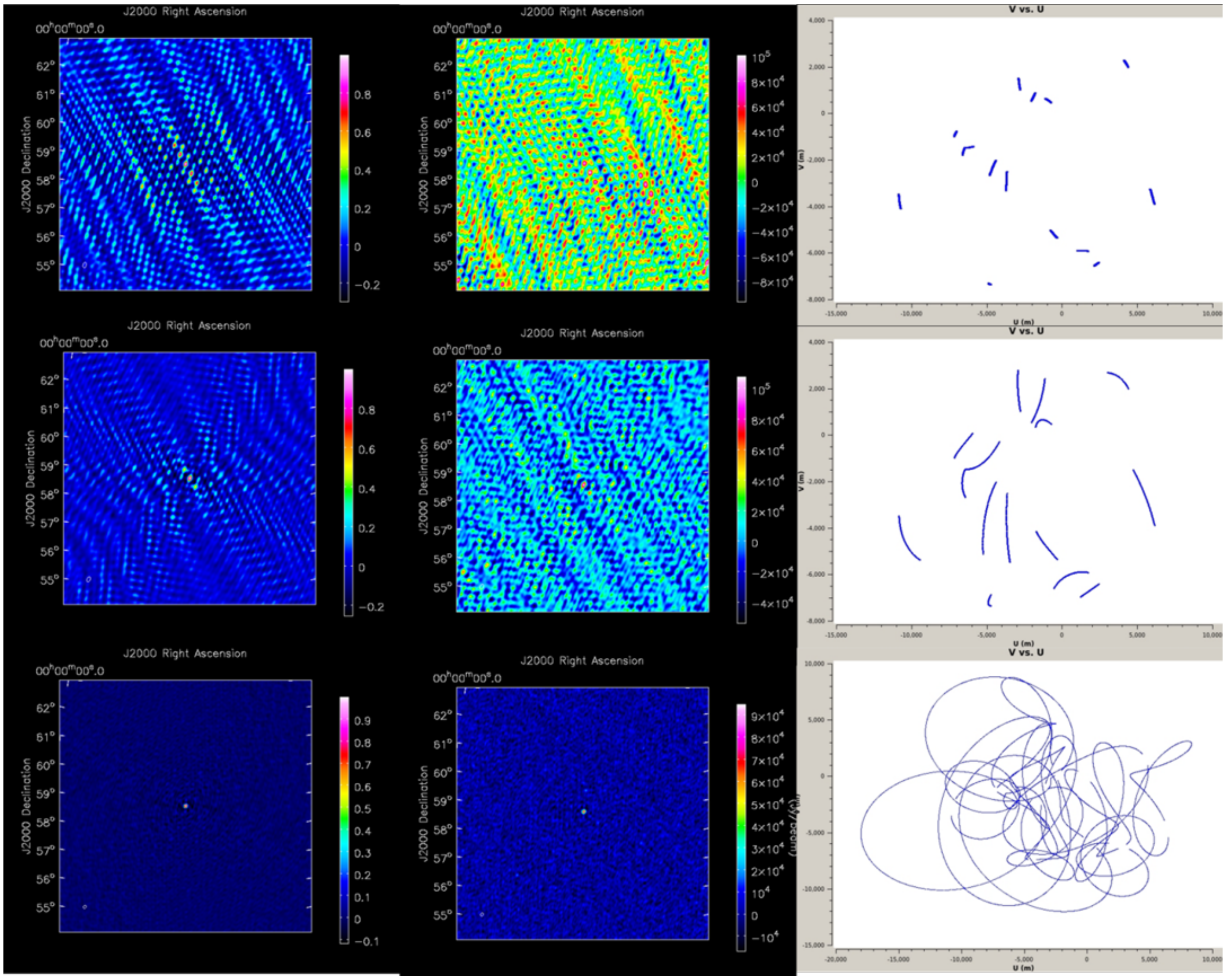

Figure 4.17: *Left Column*: Point spread functions over 30 minutes, 2 hours, and 24 hours for the SunRISE synthetic aperture pointed in the direction of Cas A. *Middle Column*: Noisy dirty image of Cas A at 10 MHz made by the SunRISE array after 30 minutes, 2 hours, and 24 hours of integration. Cas A was modeled as a point source with a flux density of 10^5 Jy imaged over a system equivalent flux density (SEFD) of $2.5 \cdot 10^7$ Jy over a bandwidth of 6.1 kHz, a duty cycle of 6.6 milliseconds/second, and a correlator efficiency of 90%. Right Column: UV coverage in the frame pointed towards Cas A of a 6 element SunRISE array after 30 minutes, 2 hours, and 24 hours of integration. One can see the progression of the relative separations between spacecraft as they progress throughout their orbit, almost coming back around to their original position after 24/25 hours of its periodic orbit has passed.

Table 4.1: Science Driven Requirements for RELIC

Requirement	Science	Implied Mission Requirements
Angular resolution	$10''$	620 km max S/C separation
Largest angular scale	$30'$	12 km min S/C separation Non-repeating baselines 32 S/C minimum
Frequency bandwidth	0.1-10 MHz + 30 MHz Best science $<$ 10 MHz Overlap with ground: 30 MHz	Data rate
Image S/N ratio	10	Min source obs. time 3 hours
Frequency resolution	16 kHz	PFB Speedups
Spectral windows	> 64	Integration time & Data Transmission
Dynamic range	10^3–10^4	Expected S/N ratios

In order to set high-level science requirements for the RELIC concept, we selected the nearest 85 DRAGNs from the 3CR sample [8]. Figure 4.18 from [28] summarizes the range of angular scales observed in DRAGNs, scaled to 10 MHz. The mean size is approximately $100''$ and 80% of the sources being in the range $10''$ to $500''$. In addition to the intrinsic sizes of DRAGNs, at the frequencies of interest, significant angular broadening due to density fluctuations in the interstellar medium occurs [73]. This propagation effect limits to approximately $10''$ the finest angular resolution that is required. Figure 4.19 from [28] shows the distribution of flux densities at 10 MHz for our sample. Most DRAGNs in our sample are predicted to be at least 100 Jy at 10 MHz.

4.5.3 RELIC Simulations

The plots in Figure 4.20 were created with a data processing pipeline to emulate the performance of the 32 element RELIC array. We tested an average DRAGN for the array, 100 arcsec wide, 100 Jy total brightness, and used a detailed picture of Cygnus A at 21 cm to provide realistic complexity to the truth image. We are integrating for 35 minutes, which is 2100 seconds, again a typical expectation. The spacecraft would be using ranging techniques to gauge the relative separations between spacecraft. Any uncertainty and error from this process gets translated to errors in the baselines and visibility data we use in the imaging pipeline. We assume a 5 nanosecond phase

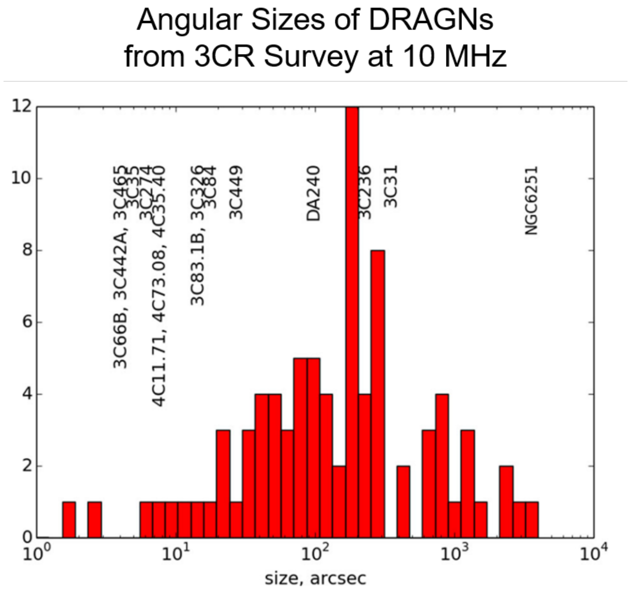

Figure 4.18: Size distribution of DRAGNs selected from the 3CR catalogue [8]

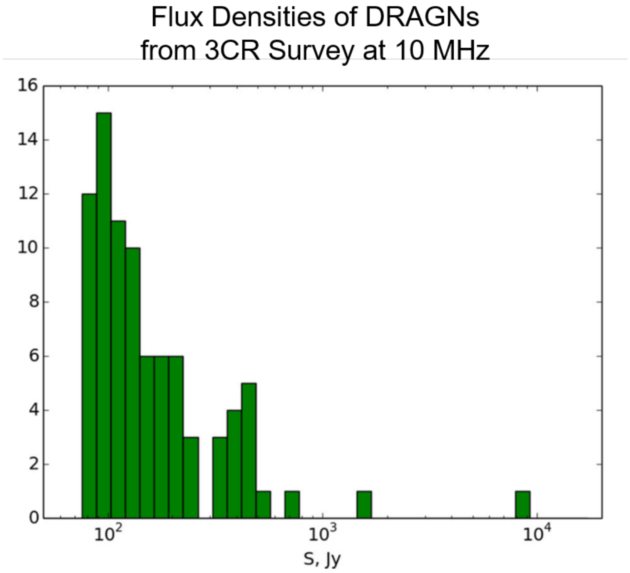

Figure 4.19: Flux densities of our double radio sources associated with a galactic nuclei (DRAGNs) sample, as selected from the 3CR survey [8] and scaled to 10 MHz. The truncation at low flux densities represents the completeness limit of the parent catalog from which our sample is drawn

uncertainty per spacecraft, and galactic noise at 10 MHz. We are using CASA's CLEAN algorithm to create the image and have w-projection turned on. We have shrunk the baselines by a factor of 10, which gives us an image 10x larger than our prescribed 100 arcsec. This was done since CASA crashes if the baselines are too large. But the relative scales are the same, so it provides an accurate sense of RELIC's performance. These simulations show that RELIC will be able to map and image the sample of DRAGNs chosen from the 3CR survey. This would be a huge leap towards mapping the entire low frequency sky, a heroic feat.

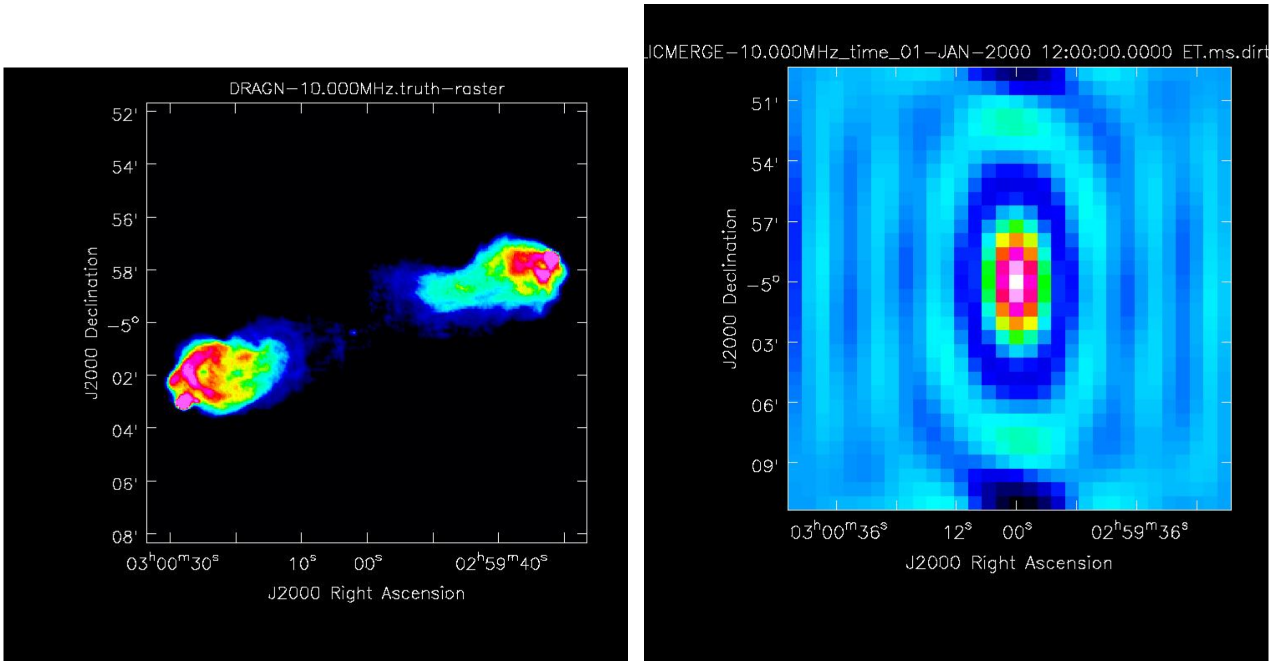

(a) Truth Image of 100 arcsec 100 Jy DRAGN, from Cyg A (b) Synthesized beam from 35 minutes of integrated orbits

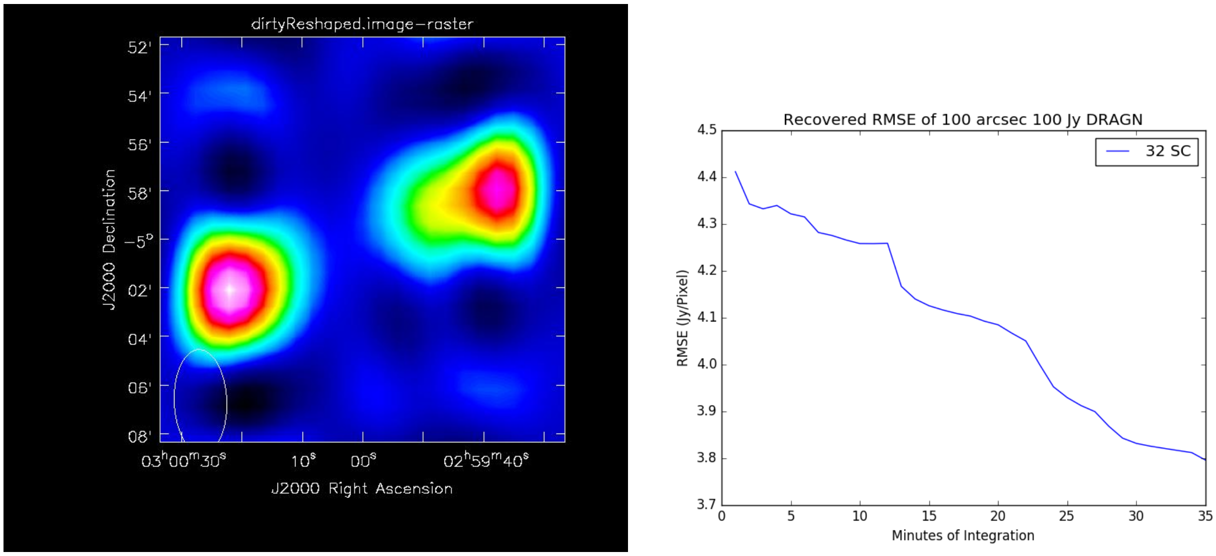

(c) Smoothed recovered dirty image after 35 minutes of integration (d) Root Mean Squared Error (RMSE) of the recovered dirty image over time

Figure 4.20: Images showing the CASA simulated performance of RELIC on a 100 arcsecond wide, 100 Jy total bright DRAGN. This was done with part of the orbit where the maximum baseline is 370 km, which corresponds to a resolution of roughly 15-20 arcsec. This resolution can be seen in effect in panel c, where the 100 arcsecond image is visibly only 5 or so beamwidths across.

CHAPTER 5

Low Frequency Earth Emissions

In the following sections, I will review transient low frequency emission sources originating from Earth's magnetosphere. These will be the target science of the lunar surface concept array in Chapter 6. Thus alongside the typical measured flux densities of each class of emission at the distances they were measured at, I have accordingly scaled the flux density out to lunar distances.

5.1 Auroral Kilometric Radiation

Auroral Kilometric Radiation (AKR) is typically found in frequencies from 50-500 kHz and can sometimes go up to 800 kHz. AKR is a powerful natural radio source emitting 10^7 to 10^8 W, and can exceed 10^9 in some events [74]. It is typically generated at magnetic latitudes greater than 65° at altitudes from 5000-15000 km. Its power generally increases with magnetospheric activity, especially when substorms develop. Reported in [74], the Interplanetary Monitoring Platform (IMP) 8 satellite observed AKR at a distance of 25.2 RE on December 20 1973 with a peak emission of 10^{-14} W/m^2/Hz at 100-200 kHz. Applying a r^{-2} law, this predicts spectral flux densities of $\sim 1.4 \cdot 10^{-15}$ W/m^2/Hz = 10^{11} Jy at the position of the Moon. While this emission is transient, it far outshines the Radiation Belt emission.

The source of this emission is thought to be the electron maser instability [75]. The cyclotron maser mechanism provides the following characteristic predictions: (1) emission occurs near the local electron cyclotron frequency Ω_e defined in Equation 5.3; (2) the plasma frequency $\omega_{pe} =$

$\sqrt{\frac{n_e e^2}{m_e \epsilon_0}}$ for electron density n_e, elemental charge e, electron mass m_e, and permittivity of free space ϵ_0 in the source region must be much smaller than Ω_e; (3) generation of the radiation occurs primarily in the right-hand extraordinary (R-X) mode. There is now evidence to back all of these features in the form of an identification of an AKR source region by [76].

[77] used data from the 4 spacecraft Cluster array to determine a typical AKR angular beaming pattern. They found that individual events were highly confined latitudinally (typically $\pm 20^\circ$ from the magnetic field tangent direction), but much wider longitudinally, i.e., along the cavity. The emission is also subjected to strong refraction upwards as it travels, implying that not every event will be detectable from lunar orbit. By looking at the average beaming of the emission over many days worth of events, we can predict what the emission may look like from the lunar surface.

[78] provides a statistical study of AKR as seen from Cassini as it passed by Earth in 1999. Using data out to several thousand R_E, they observe an average beaming of the Northern and Southern AKR consistent with conical beams each tilted towards the nightside, illuminating approximately a hemisphere each, with only sporadic observations from the day side. Past the shadow zone below 12 R_E on the nightside, emission from both poles is seen at magnetic latitudes lower than 12° or so [78, Fig. 2]. Since the Moon's orbit is inclined $\sim 28.5^\circ$ relative to the Earth's magnetic Equator, this means that observations of AKR from the Moon are predicted to sample all 3 regions: only Right Handed (RH) emission from the north pole, only Left Handed (LH) emission from the south pole, and a combination of both when its orbit is near the Earth's magnetic equator. [78] reports AKR occurence rates for this region having a nonperiodic average recurrence time of 2-4 hours, with each burst lasting 1-3 hours. The bursts are distributed log-normal in power with the likeliest power being 10^7 W, which is in agreement with the CMI triggering process. This implies that AKR can be expected to corrupt measurements of the synchrotron emission about 50% of the time on the nightside, so roughly 25% overall.

5.2 Other Auroral Transients

Related to AKR is auroral hiss, reviewed in [79]. This is mostly recorded in the evening and night hours in the auroral oval region. The continuous auroral hiss stays below 30 kHz. The impulsive auroral hiss is in the 100s of kHz range and can sometimes go up above 500 kHz, usually lasting less than 5 minutes. The likely main energy source of auroral hiss emissions is electrons at energies below 100 eV at heights greater than about 5000 km above the aurora/ ionosphere precipitating downward. Maximum spectral flux densities of $\sim 1{\cdot}10^{-11}$ W/m^2/Hz = 10^{15} Jy seen from elevations of 1-2 R_E by satellites such as Injun-5 and Alouette-2 from 2500 km above the surface. This scales to a maximum spectral flux density of around 6.1$\cdot10^{-18}$ W/m^2/Hz = 6.1 $\cdot10^{8}$ Jy at lunar distances. [80] shows the space based occurrence rates of auroral hiss from the ISIS-2 satellite being between 30-50% of the time, depending on latitude and geomagnetic local time.

Medium Frequency (MF) bursts are also prominent sources near these frequencies. MF bursts are correlated with auroral hiss and they are both thought to be associated with the substorm expansion phase [81]. They have a frequency range of about 1.5-4.3 MHz, and usually last around 10 minutes, though they are actually made up of many wave packets lasting 200-300 microseconds each. Assuming a source altitude of 500 km, on ground brightest packets yield 1-2 microvolt/m/$\sqrt{\text{Hz}}$, but over 100 ms, the average signal is at most 750 nanovolts/m/$\sqrt{\text{Hz}}$. The wave packet nature of MF Bursts may be due to nonlinear wave processes or bursty characteristics in the precipitating auroral electrons. The maximum spectral flux density at the lunar surface would be a couple orders of magnitude below that of AKR at around 10^{-18} W/m^2/Hz = $\cdot10^{8}$ Jy . [81] reports the occurrence rates of MF bursts as once every 6 to 20 hours, depending on K_p.

Auroral roar is another class of low frequency emission that is usually found between 2.8 and 3.0 MHz and only has a bandwidth of a few hundred kHz. It is highly structured and induces voltages of about 1-2$\cdot10^{-13}$ V^2/m^2/Hz [82] and lasts around 10 minutes. They are thought to occur at about twice the local electron cyclotron frequency, at an altitude of around 250 km. This emission has a typical strength of 1 microvolt/m, and may be beamed. AKR in same place is 10-100 millivolts/m implying that auroral roar's total flux density is couple orders of magnitude below that of AKR at around 10^{-18} W/m^2/Hz = $\cdot 10^8$ Jy. [83] reports on the latitudinal dependence for auroral roar occurrence rates, showing that it occurs once every 3-5 hours, and is correlated with K_p.

These last 3 sources are sometimes highly localized, with a signal decrease of 35 dB between observations 200 km away [81]. This indicates there may some inherent beaming or directional scattering in these processes that may further decrease the signal seen from the lunar near side. There also may be a degree of absorption from the ionosphere between the signal source and the lunar surface. A pathfinder antenna on the lunar near side would be helpful in quantifying how many of these events are detectable from the lunar surface, and how strong they are.

Table 5.1: Characteristics of Earth originating transients as seen from a lunar based radio array

Transient Source	Frequency Range	Lunar Flux Density 1 MHz	Occurrence Rate	10 km (Over)resolution
Auroral Kilometric Radiation	50 - 800 kHz	10^{10} Jy	50% on night side	0.2-0.4° at 500 kHz 10x better
Auroral Hiss	100 - 600 kHz	$6 \cdot 10^8$ Jy	30-50% K_p correlation	0.3° at 500 kHz
Medium Frequency Bursts	1.5-4.3 MHz	10^6 Jy	10 minutes every 6-20 hours K_p correlation	0.7° at 3 MHz
Auroral Roar	2.8-3.0 MHz	10^6 Jy	10 minutes every 3-5 hours K_p correlation	0.7° at 3 MHz
Terrestrial Continuum Radiation	30 - 200 kHz	10^5 Jy	60%	N/A low frequency

5.3 Terrestrial Continuum Emission

[84] analyzes data from the Dynamics Explorer 1 (DE1) spacecraft and provides an overview of Terrestrial Continuum Emission (TCE). Virtually all continuum events have their sources near the magnetic equator between 2.0 and 4.0 Re geocentric distance and occur at frequencies between 30 and 200 kHz, with little emission expected at angles less than $20°$ from the magnetic equator. The radiation is beamed outward in a broad beam directed along the magnetic equator with a beam

width of about $100°$.

DE1 was 5 Earth Radii away from the Earth, and about 2 Earth Radii away from sources that were more than 2-4 orders of magnitude above the Galactic background. This implies at lunar distances the flux densities will be 0.1% of the brightness at DE1, on the order of the Galactic background around 10^{-21} W/m^2/Hz = $\cdot 10^5$ Jy. Unlike the tight beaming of auroral transients in the previous subsection, TCE's wide, equatorial beaming ensures that a lunar near side array would see the majority of TCE events occuring on the visible half of Earth. [84] also reports the occurrence frequency of TCE as 60% of the time. The occurrence rates increase sharply at the midnight meridian, and increases toward the dawnward direction.

5.4 Overresolution of Bright Transients

[23] shows how localization better than the beamwidth can be achieved provided there is a strong Signal to Noise Ratio (SNR). This can be used to estimate the degree to which the array can localize any strong transient emissions. Θ_M represents the true minimum size of a source that can still be resolved by the interferometer. β is a constant that depends on the exact configuration of the array, but is usually between 0.5-1.0. λ_c is the value of log-likelihood corresponding to the critical probability of the null hypothesis taking a value of 3.84 for a 2 sigma cutoff, and 8.81 for a 3 sigma cutoff. The null hypothesis in this case is that the source is a true point soruce, so Θ_M can also be thought of as the largest source that could be confused with a point source for a given SNR, giving a measure of the true resolution of an array. This measure is given relative to the Full Width Half Maximum (FWHM) in radians of the synthesized beam of the array, which is the regular method of determining the array's resolution depending on the observing wavelength λ and the longest projected distance between receivers D.

$$FWHM = 1.22\frac{\lambda}{D} \tag{5.1}$$

$$\Theta_M = \beta\left(\frac{\lambda_c}{2(SNR)^2}\right)^{\frac{1}{4}} \cdot FWHM \tag{5.2}$$

For bright transients like strong Auroral Kilometric Radiation, this implies that the array will be able to localize in the plane of sky far better than its beamwidth. In fact, for all of the following transient signals the ability for a high degree of localization from our array would be interesting science topics in themselves. The level of overresolution possible for a given SNR transient is listed in Table 5.1, alongside other relevant quantities such as occurrence rates and frequency ranges. Transient emission is difficult to characterize to the 1 Jy level, so it is assumed that any data flagged to contain a transient source will be removed for the analysis of the synchrotron emission.

5.5 Earth Synchrotron Emission

5.5.1 Synchrotron Physics

Understanding the energetic electron environment below 6 Earth radii has long been an area of scientific interest as well as practical concern. This information helps us to understand the radiation dosages that spacecraft at different orbits are likely to see over time, which in turn goes into the Total Ionizing Dose (TID) the spacecraft is designed to be tolerant to. The response of the radiation belts to solar input can elicit a variety of responses, complicating the calculation of how much radiation a given spacecraft has actually been exposed to so far. In order for spacecraft industries to track the predicted remaining lifetimes of all their satellites, it would be useful to have some real measure of how many energetic electrons were in Earth's radiation belts at any given time. This is especially useful for the many satellites that do not have energetic particle detectors to measure their received radiation dose. Even with detectors, existing satellites can give only single point *in situ* measurements of the electron distribution from a stable orbit. Measurements of the global synchrotron emission could yield a view of the bigger picture by providing a proxy measurement of the global electron distribution, providing useful constraints for space weather forecasting models and TID calculations. An array capable of such measurements would also be able to localize auroral transient events with high precision, providing local, small scale electron data in addition to global data.

Many planets with magnetic fields have radiation belts from trapped electrons to some degree. However, Jupiter is the only outer planet that has had synchrotron emission detected from its radiation belts, making it a good case to look at in order to understand what to expect in observing the Earth's synchrotron emission. Jupiter's strong magnetic field traps high energy electrons up to 10s of MeV [85], and these stable energetic electron belts produce synchrotron emission in the decimeter (DIM) wavelength range [86]. The physics of synchrotron emission are well understood at this point [87]: an electron at a certain energy will release photons at a broad spectrum of frequencies corresponding to the the envelope of the summation of harmonics of the cyclotron frequency. The cyclotron frequency f_c is the frequency in Hz at which a charged particle such as an electron with mass m and charge q gyrates around a magnetic field with field strength B in Gauss (G).

$$f_c = \frac{qB}{2\pi m} \tag{5.3}$$

An electron with energy E in Mega electronvolts (MeV) and pitch angle α will emit a broad range of frequencies corresponding to the envelope of the summation of cyclotron harmonics, with a maximum at around f_{max} MHz, where

$$f_{max} \approx 4.8E^2 B \sin\alpha \tag{5.4}$$

It is important to note that f_{max} is the frequency at which the maximum amount of photons are being emitted, not the highest frequency with any emission.

The energy of the Jovian radiation belt electrons that contribute to the DIM emission typically ranges from hundreds of keV (i.e., barely relativistic electrons) to several hundred MeV (i.e., ultra-relativistic electrons). It is generally accepted that at Jupiter this synchrotron emission from high-energy electrons dominates at frequencies 100-3000 MHz, while thermal emission overtakes it at higher frequencies. This synchrotron emission is characterized by large angular extent relative to the visible disk and by its high degree of linear polarization.

With the basic physics of synchrotron emission pinned down, a challenge in recent years was to deduce the spatial and energy distribution of electrons to allow to best reproduction of the observed 2D and 3D maps of radio emission [88, 89]. This has been achieved with synthetic 2D radio maps that have excellent agreement with radio observations [90, 91, 92]. These results used a version of the Salammbô code tuned to Jupiter's environment to model the physics in the radiation belt emissions [93] [94] [95].

Observation of the Jovian radiation belt synchrotron emissions has enabled major progress in the understanding of the radiation belts physics and average distribution ([92] and references therein). They also enabled the study of short time scale changes (hours to months) in the electron distributions near Jupiter related to cometary impacts [96] or to the solar wind [97]. Long time scale dynamics (years) linked to the solar wind have also been revealed [98].

Earth's radiation belts also have keV and MeV electrons as confirmed by [99] using the EPT (Energetic Particle Telescope) onboard the satellite PROBAV, as well as measurements from THEMIS [100]. These energetic electrons should also produce synchrotron emission, the brightness of which reveals the electron distribution across different energy levels. In theory, one could use measurements from an array with sufficient sensitivity to measure the brightness spectrum in small bandwidths from 1 MHz and below, and back out a detailed proxy for the current global electron energy distribution. In reality, signal to noise concerns mean that for initial arrays, large bandwidths will have to be combined in order to make good detections. Even with large bandwidths, this would still be valuable information for understanding the global response of the Earth's radiation belts to space weather. In this work we design an initial array that could do some baseline imaging of the radiation belts from the lunar sub-Earth point.

5.5.2 Simulations

As seen in Equation 5.4, the peak emission frequency for a given electron energy level is proportional to electron energy E^2 and B, the strength of the planetary magnetic field. The magnetic moment of Jupiter is $1.59 \cdot 10^{30} G/cm^3$, while Earth's is $2.10 \cdot 10^{25} G/cm^3$ [101]. Jupiter has a peak flux of ≥ 1 MeV electrons of 10^8 electrons/cm^2/s while Earth has a peak flux of ≥ 1 MeV electrons of 10^7 electrons/cm^2/s. The most energetic electrons in Earth's magnetosphere at 6 Earth radii are below 10 MeV, while the most energetic electrons in Jupiter's magnetosphere at 9.5 Jovian radii are above 1000 MeV [101, Fig. 3]. This implies that the expected emission at Earth will be at a far lower frequency than seen at Jupiter. It is partially for this reason that progress on imaging the Earth's radiation belts has been significantly slower than for those of Jupiter, since there is not

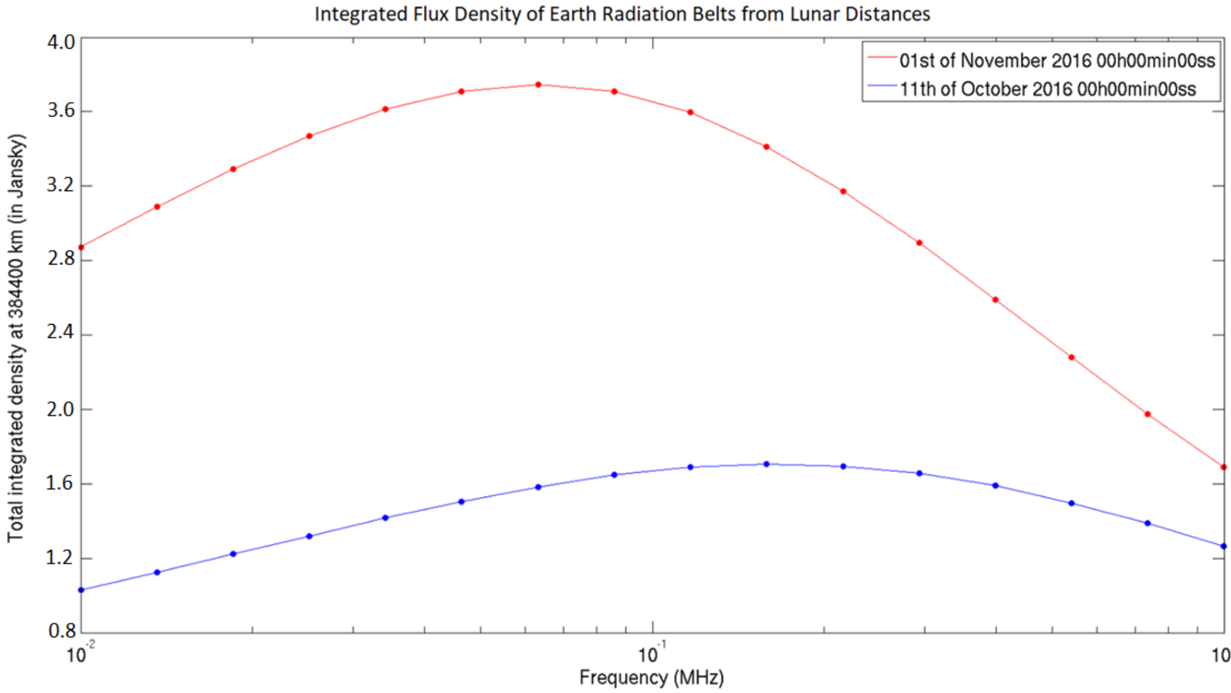

Figure 5.1: Integrated Spectral Flux Density of Synchrotron Radiation from Lunar Orbit

a straightforward way to image the global structure of the belts when you are trying to do it from a small portion of the globe itself. There is also the issue of the ionospheric cutoff, which precludes radio waves below 10 MHz from making all the way through the ionosphere to the Earth's surface. This means that 1 MHz signals generated near the topside ionosphere could not make it down to the ground for detection.

A lunar near side array would be uniquely positioned to measure the belts, and provide a near real time measure of how the Earth's radiation belts are responding to the current solar input. The Salammbô code solves the three-dimensional phase-space diffusion equation while modeling Coulomb collisions with neutral and plasma populations around Earth, wave-particle interactions, radial diffusion and magnetopause shadowing induced dropouts. It models the radiation belts in a computational domain that extends from L=1 to L=10 and uses the International Geomagnetic Reference Field (IGRF) decentered tilted dipole magnetic field model. The simulation starts 50 days before the two target dates with empty radiation belts. At L=10, the modern iteration of the Salammbô code uses the Time History of Events and Macroscale Interactions during Substorms/Solid State Telescope (THEMIS-SST) data set of electron distributions up to several hundred keV as an outer boundary condition [102]. The SST instruments aboard THEMIS provide measurements of omnidirectional electron flux in 11 energy channels ranging from 31 keV to 720 keV, as well as unidirectional ones resolving eight pitch angles between 0° and 180° [100]. The model also takes Kp as an input, which parameterizes radial diffusion strength and plasmapause position. An Ensemble Kalman Filter (EnKF) is employed by the model for data assimilation, leading to improvements in the predictions. The output is a global model of the trapped electrons in the radiation belts from 1 keV to 100 MeV.

be seen on 11th of October 2016, and a "storm time" on 1st of November 2016 when electron fluxes were higher as a result of the impact of solar wind structures onto the Earth's magnetosphere. Only these two dates are used as a research target in this study. A thorough investigation of the synchrotron radiation emitted by the radiation belts in more extreme configurations, identifying the lowest and highest possible electron fluxes, is left for future work, as are the time dynamics and response of synchrotron radiation to solar wind events. The output of these two simulated periods are then analyzed to provide realistic predictions of the brightness of the synchrotron emission up to 1 MHz. To do so, the synchrotron emission simulator developed at ONERA for Jupiter and Saturn has been adapted to Earth (for details on the synchrotron simulator, see [92] and references therein). The synchrotron emission simulator takes the electron distribution in the belts as input, as well as the magnetic field of the planet and the position of the observer. The output is a 2D image of the total intensity (first Stokes parameter) of the synchrotron emissions for a given frequency.

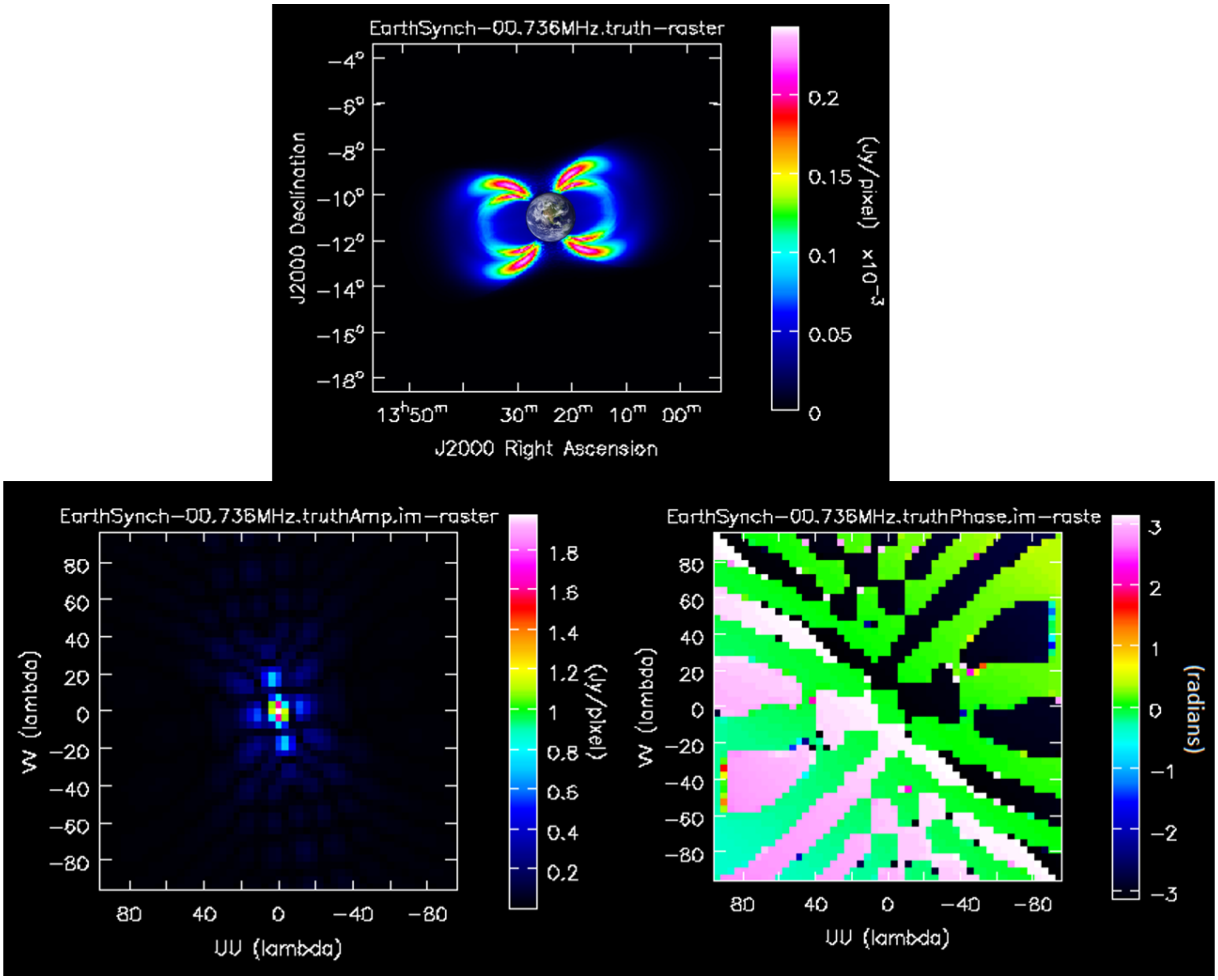

Figure 5.2: Simulated Radiation Belt Emission & Fourier Transform. *Top*: Truth image of synchrotron emission from radiation belts at Lunar Distances. This is what goes into the simulated array pipeline and is compared to the output. Brightness map created from Salammbô electron simulation data. The 1.91° Earth is added in for a scale indicator.*Left*: 2D Fourier Transform Amplitude. *Right*: 2D Fourier Transform Phase (radians).

It is expressed as brightness temperatures (in Kelvin) and can be converted to Jansky/beam or Jansky/pixel. For lunar distances, the output images are 400x400 .038 degree pixels, for a total area in the sky of 15.2 degrees. On average, the angular size of Earth from the lunar surface is 1.91 degrees, so 1 Earth radius is about 25 pixels in this scale.

We generated brightness maps from 0.1 to 1 MHz scaled to lunar distances with an overall spectral flux density in the 1 - 3.75 Jy range. These spectral flux density totals at lunar distances are seen in Figure 5.1. An example of the brightness map for a stormy period at 736 kHz is seen in Figure 5.2 (a). The other parts of Figure 5.2 show the 2D Fourier Transform of the sky brightness pattern, which is what the synthetic aperture described in Section 4 will be sampling. One should note that the synchrotron intensities are directly proportional to the flux of trapped electrons at a given energy, and a variation of a factor of 10 is easily encountered in the Earth radiation belts during extreme solar wind events.

Brightness maps of Earth synchrotron emissions can exhibit and confirm what has been observed by the Van Allen Probes, that found an “impenetrable” barrier at L=2.8, below which energetic electrons cannot penetrate [103]. This barrier has been observed over the course of many years [104], and is thought to originate from a magnetically confined bubble of very low frequency (VLF) wave emissions of human origin [105]. Equation 5.4 implies that at the highest synchrotron frequencies, most the contribution comes from the highest energy electrons at the strongest magnetic field strengths. This emission, seen in Figure 5.2a, maps the synchrotron brightness at 734 kHz, on the high end of Earth’s synchrotron emission. As expected, brightest emission is near the footpoints of the magnetic L shells where the magnetic field is stronger, and there is almost no emission below the barrier of L=2.8 at these highest frequencies, implying a lack of energetic electrons in agreement with observations from the Van Allen Probes.

CHAPTER 6

Lunar Arrays

A Lunar near side array would be the ideal location in many ways for a low frequency Earth observing array. The near side is always facing Earth, and if situated near the sub-Earth point, the Earth would stay nearly fixed in the sky's zenith. A static array configuration would get rid of problems with positional uncertainty that plagues free flying arrays. There is space on the surface to spread out, and as long as the hardware is built to last through the large temperature swings of day and night, all it has to do is survive and transmit data. The wealth of interesting Earth science described in the last chapter is waiting to be imaged in the low frequency for the first time, if we could only build the array to see it. In this develop a novel concept array that would be large enough to detect the faintest emission described in the previous chapter: synchrotron emission. We choose this as a focal point for array design because if our array can image synchrotron emission, it will have the resolution and sensitivity to see most other magnetospheric emission.

The high kinetic energy electrons that populate the Earth radiation belts spontaneously emit synchrotron emissions (the relativistic counterpart of cyclotron emissions) because of their interaction with the planetary magnetic field. The brightness of the Earth's synchrotron emission from its radiation belts reveals the electron distribution across different energy levels. A lunar near side array would be uniquely positioned to image this emission and provide a near real time measure of how the Earth's radiation belts are responding to the current solar input. The Salammbô code is a physical model of the dynamics of the three-dimensional phase-space electron densities in the radiation belts, allowing the prediction of 1 keV to 100 MeV electron distributions trapped in the belts. This information is put into a synchrotron emission simulator which provides the brightness distribution of the emission up to 1 MHz from a given observation point. We run simulations on a “quiet time” which represents what can be seen on 11th of October 2016 (midnight) and a “storm time” (1st of November 2016). These yield brightness maps from 0.1 to 1 MHz for a Lunar observer with a overall spectral flux density in the 1 - 3.75 Jy range.

Using Digital Elevation Models from Lunar Reconaissance Orbiter (LRO) Lunar Orbiter Laser Altimeter (LOLA) data, we select a set of locations near the Lunar sub-Earth point with minimum elevation variation over various sized patches where we simulate radio receivers to create a synthetic aperture. We consider realistic noise sources from amplifier noise, quasithermal noise from electrons on the Lunar Surface, Galactic foreground, Blackbody radiation, Earth Auroral Kilometric Radiation, Auroral Roar, Auroral Hiss, Medium Frequency Bursts, and Terrestrial continuum radiation. We decide on a science bandwidth of 500-1000 kHz to avoid most of the transient interference. By using various post processing techniques and order of magnitude arguments, we reduce the noise problem to amplifier noise and electron quasithermal noise. The latter of these is contested in its intensity, and we have thus created an optimal, moderate, and conservative noise budget by varying the level of electron quasithermal noise.

We then use a custom CASA code to image and process the data from our defined array. We find that for a moderate lunar surface electron density of 250/cm^3, the radiation belts may be detected in 1-2 times a day with a 16384 element array over a 10 km diameter circle. Lunar surface electron densities in the 1000s mean there will be too much quasithermal noise to observe the radiation belts in a reasonable time frame. Such high densities are only theoretically possible at low Solar Zenith Angles, and would fall off towards the night side. If functional at Lunar night, such an array could make a snapshot of Earth’s radiation belts 10-20 times a day.

6.1 Noise Environment

We follow [26] which gives the equations needed for calibrating the response of a short dipole antenna. They use these equations to do the antenna calibration of the STEREO/WAVES (S/WAVES) radio instrument [106] onboard the STEREO spacecraft [107], using the Galactic radio background as a reference source. They considered 3 main sources: amplifier noise, quasithermal noise from free electrons, and Galactic background radiation from the Milky Way. Out study will include all relevant potential sources of noise for measurements requiring sensitivity on the order of 1 Jy. These competing sources can be put into 3 classes of signals: removable constants, transients, and unavoidable noise.

6.1.1 Removable Constant Background Radiation

These noise sources are static in nature and must be understood to the sub-1 Jy level in order to remove them and detect the synchrotron emission from Earth's radiation belts.

6.1.1.1 Galactic Background Radiation

Galactic Thermal Noise from the Milky Way has been characterized extensively before [65] [108]. The model from [108] is seen in Figure 6.1 alongside other large noise sources. From spinning antenna experiments, it's been thought that the Galactic brightness below 10 MHz is mostly isotropic. Modulations as a function of the observed solid angle are around 20% at 0.3 MHz, and decreases down to near 0% at 3.6 MHz [109], with the Galactic poles having a slight brightness enhancement.

This implies for nonzero baselines, there is a maximum power of 20% of the average Galactic brightness. In order to detect the radiation belts, this is a foreground source that will needed to be understood to around a 10^{-5} level in order to not confuse it with the weaker synchrotron emission. This will be a mapping effort that has happened at higher frequencies, but never to such a degree for the lowest frequency radio sky. Because Galactic background radiation is the largest static source in the low frequency sky, it is also the most useful for calibration of the antennas [26].

6.1.1.2 Blackbody Noise

There are 3 main blackbody Sources to consider: the Earth, the Sun, and the lunar surface itself. Earth has an equivalent blackbody temperature of 288 K. Following Plank's law [110], a maximum blackbody brightness is found to be $8.8{\cdot}10^{-26}$ W/m^2/sr/Hz at 1 MHz, and decreases for lower frequencies. One can multiply these values by $4\pi \cdot (\frac{R_E}{D_{EM}})^2$ to account for the inverse square decrease in intensity from the Earth's surface to the Moon and convert to spectral flux density units W/m^2/Hz to make a Jansky comparison. This decreases the total signal from the Earth's blackbody output to an integrated 30.4 mJy for 1 MHz at lunar distances and is less strong at lower frequencies. This effect is small and fairly constant and may be subtracted out of the data on a per channel basis. In the scale of our truth images, this 30.4 mJy signal is spread throughout the 1960 or so pixels that make up the Earth, giving an average of about 0.0156 mJy/pix. This over an order of magnitude below the peak mJy/pix values for the radiation belt, and is ignored in our simulations.

The Sun has a blackbody temperature of 5800 K, giving a maximum surface brightness of $1.78{\cdot}10^{-24}$ W/m^2/sr/Hz at 1 MHz. The mean radius of Sun is 696,000 kilometers and 1 AU is $1.496{\cdot}10^{8}$ kilometers. Multiplying again by $(\frac{r_1}{r_2})^2 \cdot 4\pi$ yields $4.838{\cdot}10^{-28}$ W/m^2/Hz or 48 mJy for the flux density at the Moon. This originates from a 0.2 degree circular source, and would correspond to to about 2.5 mJy/pixel when spread through the 20 or so pixels the sun would take up in the resolution of our truth images. These levels are similar to those in the signal in the Earth's synchrotron emission at lunar distances, and will thus have to be removed in post processing with CLEAN [67] or a similar algorithm if it is close to the Earth in the sky. A more advanced multiscale method like MultiScale-CLEAN (MS-CLEAN) [111] may also be used to remove the Sun from the image, using the known size of the Sun as an input to facilitate an direct removal of that sized feature. Peeling methods [112] may also be used to remove the influence from this known source in the visibility domain, before the imaging process.

The Moon has an average black body temperature of 271 K, but can have temperatures of 373 K in the daytime (yielding a 1 MHz blackbody noise of $1.14{\cdot}10^{-25}$ W/m^2/sr/Hz or $1.44{\cdot}10^{-24}$

W/m^2/Hz = 144 Jy) and 100 K at night (yielding a 1 MHz blackbody noise of 3.06$\cdot 10^{-26}$ W/m^2/sr/Hz or 3.85$\cdot 10^{-25}$ W/m^2/Hz = 38.5 Jy). Since this is from the surface of the Moon itself, and not from a small area in the sky, this blackbody noise will add random thermal noise to our system, but is less than 3 orders of magnitude below other noise sources even in optimistic amplifier limited noise regimes. We will therefore not include it in our simulations. A summary of the basic characteristics of these constant background radiation noise sources can be seen in Table 6.1.

Table 6.1: Characteristics of constant sources as seen from a lunar based radio array

Constant Source	Lunar Flux Density 1 MHz	Notes
Galactic Brightness	$5 \cdot 10^6$ Jy	Acts like correlated noise
Earth Blackbody	$3 \cdot 10^{-2}$ Jy	1.9° circle from the Moon 273 K
Lunar Blackbody	38 - 144 Jy Night to Day	Added to background noise 100 - 373 K
Solar Blackbody	$4.84 \cdot 10^{-2}$ Jy	0.5° circle from the Moon 5800 K

6.1.2 Unavoidable Noise

These are noise sources that drive the integration time required for a good detection. There is no way to subtract it out or get around it.

6.1.2.1 Amplifier Noise

This is receiver dependent noise that will not be fully understood until actual hardware prototypes are built. [113] goes through the process of characterizing the noise and impedance of the amplifier and other electronics of the receiver for the Long Wavelength Array antenna. Similar techniques would be used to analyze the response of our chosen antenna for a lunar based array. As a stand in, we choose a level of amplifier noise with equivalent flux density of 10^{-20} W/m^2/Hz/sr. This was chosen to roughly match the amplifier noise of other space based antennas such as SunRISE and STEREO/WAVES.

6.1.2.2 Quasithermal Noise

Below 750 kHz plasma thermal noise is a non-negligible factor in solar wind conditions, and dominates the noise levels below 500 kHz. For a lunar surface with an enhanced electron density from photoionization from Solar photon flux on the dayside, this noise can become the dominant factor. For electrically short antenna, the formula for the induced voltage by these free electrons is given by [114] and [115], where n_e and T_e are the local electron density (cm^3), f is the observing frequency, and L the physical length (m) of one boom (or arm) of the dipole. We assume for each receiver, each boom is 5 m long.

$$V_{QTN}^2 = 5 \cdot 10^{-5} \frac{n_e T_e}{f^3 L} \tag{6.1}$$

This is the voltage at the ends of the antenna, so the actual received variations will be multiplied by the gain parameter/wave reflection coefficient from impedance mismatch Γ^2 which we take as 0.5^2 in our calculations, matching S/WAVES [26, Eqn. 7]. In Equation 6.2, V_r^2 is the received spectral voltage power, V_{noise}^2 is the amplifier noise, R_r is the radiation resistance of the antenna, λ is the observing wavelength, and B_f is the average spectral sky brightness.

$$V_r^2 = V_{noise}^2 + \Gamma^2 V_{QTN}^2 + 2\Gamma^2 R_r \lambda^2 B_f \tag{6.2}$$

In order to apply this formula to estimate the level of quasithermal noise on the lunar surface, we have to have expected values for the electron density and temperature. There has never been a radio antenna that could measure the true level of quasithermal noise on the surface of the Moon, so we survey the predictions from theory and remote sensing experiments. The first experiments that provided an estimate of lunar electron density on the surface were observing radio refractions from the crab nebula [116] [117]. From these measurements they inferred the presence of a lunar ionosphere above the sunlit lunar surface with peak electron concentrations $n_e \approx$ 500 - 1000 /cm^3.

A few years later, Soviet spacecraft also did a radio refraction timing experiment [118] [119] [120]. Luna 19 and 22 estimated radial density profiles from radio refraction timing data finding the surprising result that the lunar surface may host a stable electron density on the order of 1000/cm^3 observed on the sunlit side, including regions near the terminator.

Lunar Prospector data from 1998$-$1999 used a Electron Reflectometer to measure T_e and n_e at altitude ranges of 30$-$115 km. The Reflectometer collected data for electrons from 7 eV to 20 keV for 19 months [121]. On the day side, $n_e \approx$ 8/cm^3 and $T_e \approx$ 12 eV. At the night side n_e decreases exponentially and T_e reaches to 50 eV. On the lunar night side n_e shows a range of 2–0.002/cm^3 and T_e has a range of 15-50 eV. Lunar surface potential is found to be highly dependent on electron temperature, which varies with solar input, and may be especially dependent on crustal magnetic fields.

A more recent experiment with LRS (Lunar Radio Science) on Kaguya-SELENE by the Japanese space agency has found evidence of transient enhancements in surface electron density around 250/cm^3 but only within a solar zenith angle of 60 degrees. They used radio occultation experiments with multiple spacecraft to probe the lower lunar atmosphere [122]. SELENE did not find a large persistent enhancement like Luna over the whole dayside. An additional factor that may explain the discrepancy is the amount of ultraviolet radiation at the times of the experiments [123]. The F10.7 index is a measure of the noise level generated by the sun at a wavelength of 10.7 cm at the earth's orbit, and acts as a useful proxy for ultraviolet radiation from the Sun. The F10.7 index was particularly low at 70 solar flux units (1 sfu = 10^{-22} W m^2 Hz^{-1}) during the SELENE mission at solar minimum. On the other hand, during the Luna 19 and 22 missions the index was in a range between 75–125 sfu.

There have also been several theory driven approaches to estimating electron conditions at the lunar surface. [124] did a calculation of the photoelectron sheath finding a surface electron density of 60/cm^3, using a Maxwellian distribution for the photoelectrons. This may be outdated by [125] and [126], which use a more physically motivated half Fermi Dirac (F-D) distribution for velocities

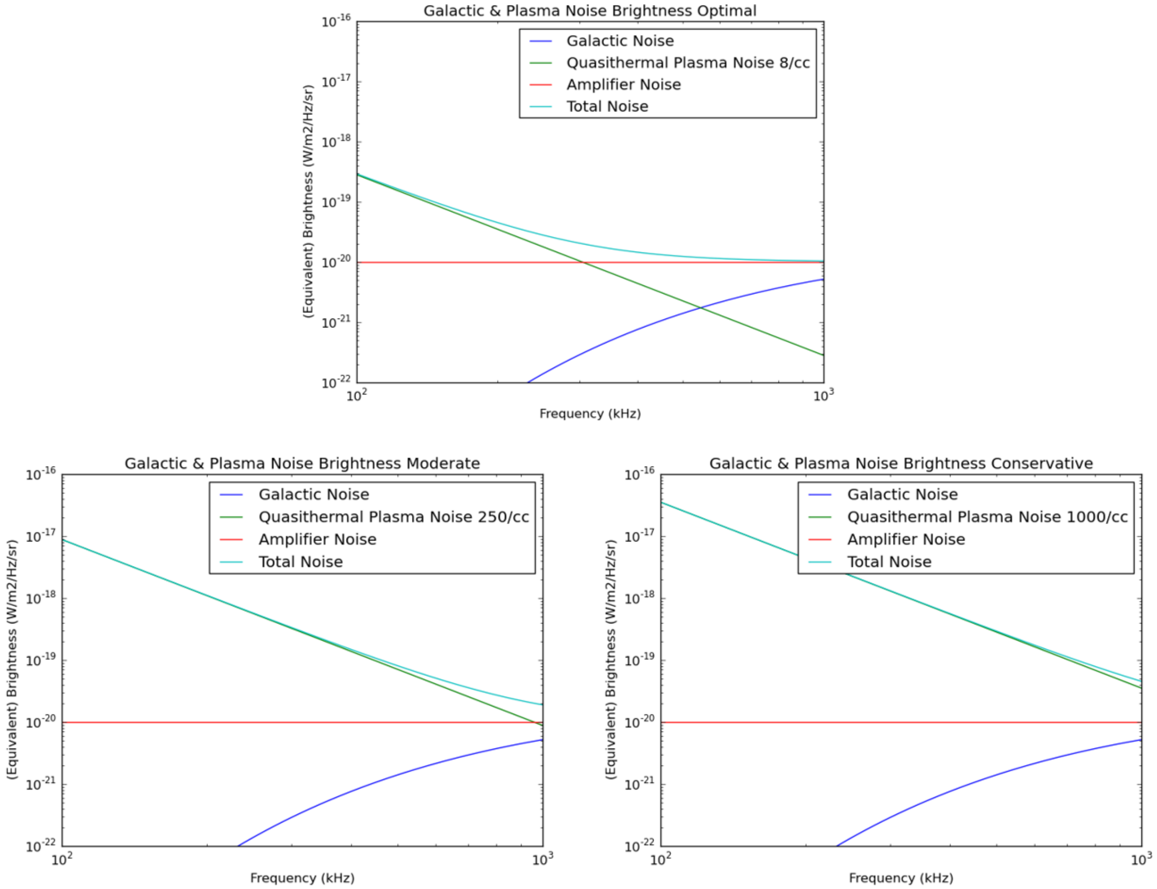

Figure 6.1: Noise budgets with different quasithermal noise assumptions. These include the main unavoidable static noise sources for a lunar surface radio array over the range 100-1000 kHz. *Top*: Optimal 250/cm^3, Amplifier Dominated Noise Budget. *Left*: Moderate, 250/cm^3 Electron Quasithermal Noise Dominated. *Right*: Conservative, 1000/cm^3 Electron Quasithermal Noise Dominated. The sum of these noise sources is multiplied by 4π steradian to compute the System Equivalent Flux Densities (SEFDs) which we use to compute Signal to Noise ratios.

of the photoelectrons. These analyses find a electron densities on the order of 1000/cm^3, and up to 7000/cm^3 and higher depending on the solar wind input and photoelectric efficiency of the surface. Both of these theories predict the reduced photon flux in late afternoon or nighttime will lead to a corresponding decrease in electron density.

We can plug these values into Equation 6.1 to get conservative (1000/cm^3 n_e), moderate (250/cm^3 n_e), and optimistic (8/cm^3 n_e) values for the plasma noise portion of the noise budget that dominates the lower band. A electron temperature of 12 eV will be used for all noise budgets, which is justified since the only time it is known to be higher than that is on the night side when n_e is also much lower, so the product of $n_e T_e$ from Equation 6.1 is equivalent to the optimistic case. Figure 6.1 shows the equivalent brightness of all the unavoidable noise sources together with a model of the Galactic brightness for reference.

6.1.3 Deciding on an Operational Science Band

In order to avoid most of the transient sources, we are setting the observing range to 500-1000 kHz. This range avoids most of the AKR, Auroral Hiss, and Earth Continuum Emission that occurs below 500 kHz, and almost completely avoids the Auroral Roar and MF Bursts that occur above 1.5 MHz. There were no Salammbô simulations done to predict the radiation belts above 1.0 MHz, but 1.0-1.5 MHz is likely to be a useful extension of our observing range since there are normally no more transients than there are in the 500-1000 kHz range. But for the rest of the paper, we assume a operational bandwidth of 500-1000 kHz. Averaging over this range, the optimistic noise budget gives an average brightness of $1.1 \cdot 10^{-20}$ W/m^2/Hz/sr which we multiply by 4π for a system equivalent flux density (SEFD) of $1.38 \cdot 10^{-19}$ W/m^2/Hz = $1.38 \cdot 10^7$ Jy. The moderate noise budget gives an average brightness of $3.66 \cdot 10^{-20}$ W/m^2/Hz/sr which we multiply by 4π for a SEFD of $4.6 \cdot 10^{-19}$ W/m^2/Hz = $4.6 \cdot 10^7$ Jy. The conservative noise budget gives an average brightness of $1.16 \cdot 10^{-19}$ W/m^2/Hz/sr which we multiply by 4π for a SEFD of $1.46 \cdot 10^{-18}$ W/m^2/Hz = $1.46 \cdot 10^8$ Jy. If there are any transients that leak into this operating range, we will have to have some system to recognize the extra flux, and filter the data from that bandwidth and time period from the data that will go into the synchrotron imaging. The data could be processed at high spectral resolution to flag interference before integrating across the observing band for imaging.

6.2 Designing a Mock Array

Predicted brightness maps have to be run through simulated lunar arrays with realistic noise to see what array size/ configuration will be needed to image the emission of the belts. However, traditional radio astronomy software is hard coded to assume an Earth based array. To circumvent this, we manually calculate the antenna separations and insert them along with the simulated visibilities into a Common Astronomy Software Applications (CASA) Measurement Set (MS) file for analysis [24]. These MS files contain the information of the array configuration, alignment with the sky, and visibility data. This is a standard format that can be used with a wide range of existing imaging and analysis algorithms.

The mathematics and theory of creating images with radio arrays has been fleshed out in classic textbooks such as Thompson et al.'s Interferometry and Synthesis in Radio Astronomy [2]. Stated informally, the basic insight to understand is that for a group of antennas, the cross correlation of any pair of antennas (a *visibility*) will yield the information of a single 2D Fourier coefficient of the sky brightness pattern. The exact spatial 2D wave that is sampled depends on the separation between the given pair of radio receivers in units of wavelength of the observing frequency. The further apart the receivers are in a certain coordinate system oriented towards the imaging target, the higher the spatial frequency sample will be provided, giving higher resolution details at small scales. Conversely, the closer a pair of receivers are in that same reference frame, the lower the spatial frequency sampled, yielding larger scale structure information at a lower resolution.

In order to solve for the antenna separations, or *baselines*, a set of locations were chosen using data from the Lunar Reconnaissance Orbiter (LRO) [127]. We use Lunar Orbiter Laser Altimeter (LOLA) data [128] which provides high-resolution Lunar Topography (SLDEM2015) data, giving the altitude for any given longitude and latitude. The data is in the Moon Mean Earth/Polar Axis (ME) frame, which has the Sub-Earth point at Longitude 0° Latitude 0°. The Moon ME frame is standard for all lunar data in the Planetary Data System (PDS). We use SPICE [129] to align the Moon ME frame to the celestial sky in order to track its relative position with the Sun and Earth. By having the array near the sub-Earth point, the array will be very close to planar all the time due to the orbital lock of the Moon with Earth. The Earth will be directly overhead near the center of the sky at all times, with only slight variations in the projected baselines from the wobbling of the lunar rotation, which is accurately tracked by SPICE.

With this simulation pipeline in hand, the simulated synchrotron map may be propagated through a model of a distributed radio array on the Moon to produce dirty images that approximate the performance of the array. A dirty image is an array's imperfect representation of the true sky brightness pattern that has been corrupted by the inherent sparseness of a distributed radio array. The configuration of the array determines the dirty beam, or the point spread function (psf), that is the combination of unweighted Fourier samples obtained from each pair of antennas. The dirty image is mathematically equivalent to a convolution of the true sky brightness pattern with the dirty beam. Any sidelobes or imperfections in the beam will translate into imperfections in the dirty image.

6.2.1 Array Locations

We will test out 3 array sizes: 6 km diameter, 10 km diameter, and 20 km diameter. In order to find a good place for the center of each array, we zoom in on the area around the Sub Earth point at 0° Longitude 0° Latitude. We limit our search to the area of ±2° Longitude and Latitude around the Sub-Earth point. At the equator, each degree of Longitude is 29.67 km, so the approximate area considered was 14085 km^2. Within this area, patches of land with low variance in elevation were found in order to base various sized arrays. We found the 5$\times$5 km^2, the 10$\times$10 km^2, and the 20$\times$20 km^2 patches that had the lowest variance in elevation according to the SLDEM2015 data with a resolution of 128 pixels per degree. These locations and their root mean square (RMS) in elevation are shown in Figure 6.2 (b)-(e).

6.2.2 Array Formation

Now that we have locations for the arrays, we have to decide on the configuration of the array. We assume that we are using 5 m dual-polarization dipole antennas for all our receivers, and that there is a minimum distance of 15 m between receivers. This limits the maximum density of receivers to $\sim$ 4400 antennas/km^2. Though that dense of a distribution won't be needed everywhere, a large amount of receivers are needed to detect a low frequency synchrotron emission signal that is at least 5 orders of magnitude below the noise.

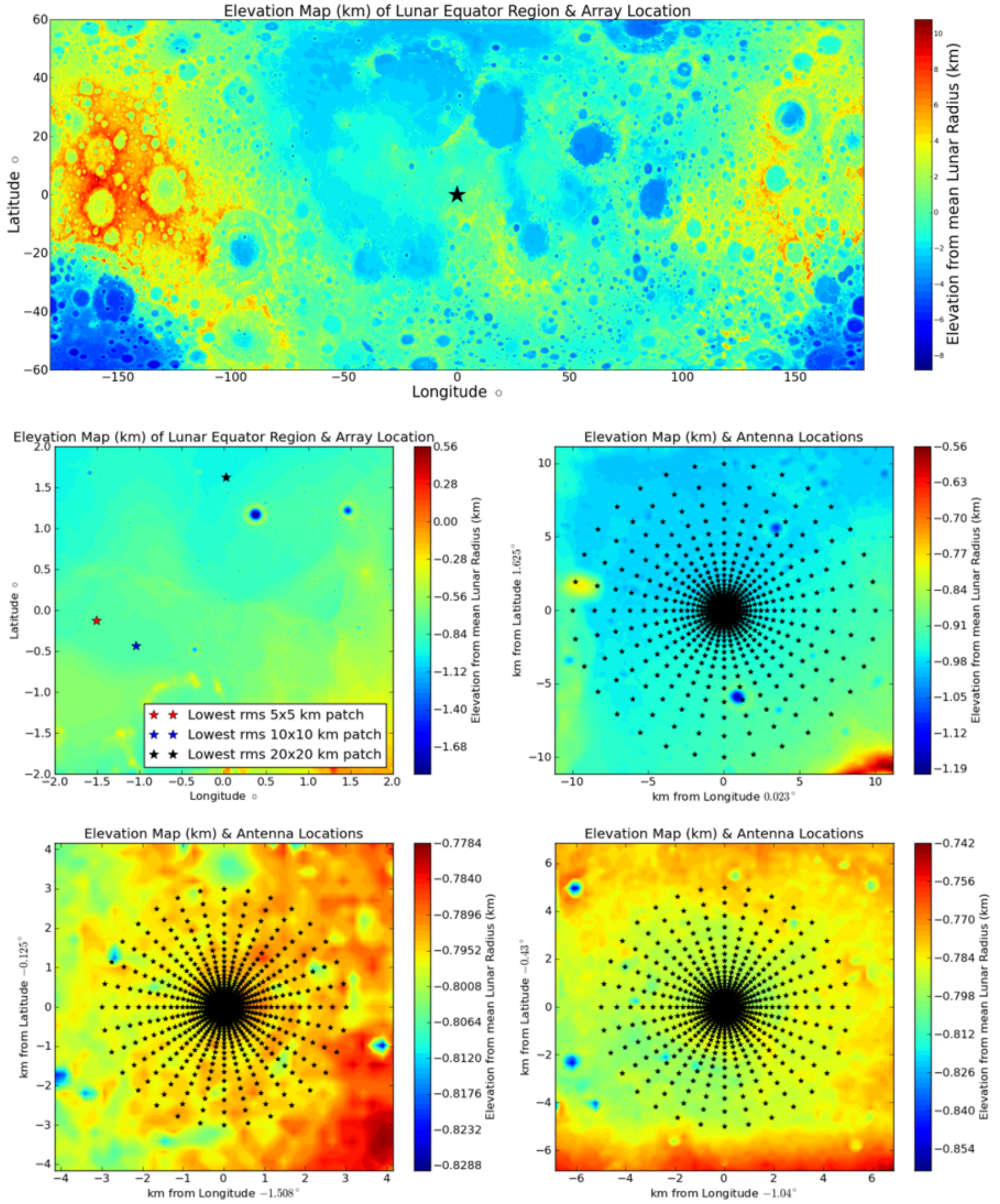
Elevation Map (km) of Lunar Equator Region & Array Location

Elevation Map (km) of Lunar Equator Region & Array Location

Elevation Map (km) & Antenna Locations

Elevation Map (km) & Antenna Locations

Elevation Map (km) & Antenna Locations

Figure 6.2: *Top:* Center of array at sub-Earth point, 0° Longitude, 0° Latitude in the Mean Earth/Polar Axis (ME) frame used for all modern lunar data. An array near here will have the Earth in the zenith of its sky continuously. *Middle Left*: Lowest elevation variation array location candidates near the Sub Earth Point for 6, 10, and 20 km arrays. *Middle Right*: 10 km radius Array, Elevation σ = 13.5 m. *Lower Left*: 5 km radius Array, Elevation σ = 5.6 m. *Lower Right*: 3 km radius Array, Elevation σ = 2.8 m. These elevation maps show different 1024 element array configurations of logarithmically spaced concentric circles. This configuration is relatively unoptimized, but provides many short baselines where most of the signal for diffuse structures are. The logarithmic aspect also provides some non-uniformity, increasing the array's UV coverage.

There exist several algorithms for the optimization of array configuration for a given number of antenna and location. Iterative algorithms for specific topographies [130] and imaging targets [131] may be used to find a high performing configuration better than simple arrangements such as logarithmically spaced circles. These techniques may be extended in different ways to take obstacles such as craters into account [132], or minimize certain parameters like cable length [133]. These cables are used to transmit data from each receiver to a central facility for data processing and transmission.

Minimizing cable length helps decrease construction costs, but an alternative to using cables in the first place is to have a central tower that has a Line of Sight (LOS) view of every antenna that would facilitate communication via a higher frequency antenna. The equation for the horizon distance is $d = \sqrt{h(2R + h)}$ for radius R and height of observation h. For lunar radius 1,737.5 km and d = 10 km, this equation can be solved for h = 28.8 meters. So a tower roughly 30 m or 100 ft tall could be seen by every antenna station out to 10 km. Though to actually transmit data at an acceptable rate it would need to be taller since transmitting directly to the horizon leaves little room for error. Fortunately, monopole towers up to 200 feet are commonly used on Earth for a myriad of uses, including wireless communication. These towers have a small footprint and foundation, and are relatively fast and easy to erect.

The decision for the configuration of a radio array should also take the point spread function into account and assure that an array has sufficient UV coverage. It has been shown that non-regular arrays such as hierarchical arrays that introduce small tweaks into their array geometry can give better signal to noise ratios or less sidelobe interference than more uniformly spaced arrays[134]. Previous experiments with array design have also showed one can employ a sequential optimization strategy to your layout and reach near theoretical limits on sidelobes [135] [136].

Another powerful technique that might be utilized for the configuration of a large scale lunar array is hybrid arrays. These are getting more popular on the ground with low frequency telescopes like the MWA [137], LOFAR [138], and LWA [139] all employing a version of this strategy. Hybrid arrays consist of a mixture of single elements and clusters of elements that have been phased up to act as a single element. Nearby groups of antennas are made to act like a single phased array, and then one employs interferometry to use many of these groups of antennas that spread far away from each other. This yields both short and long baselines while maintaining a tractable way to handle all the data processing that's spread over many kilometers.

As an initial stand in for a more optimized array design, we opt for an array shape of logarithmically spaced circles. By logarithmically spacing the antennas in each arm of the array, more baselines are concentrated in the shorter ranges that provide more signal for imaging the diffuse synchrotron emission belts. The logarithmic aspect of the layout also adds a layer of non-uniformity to the design, increasing the array's UV coverage. We simulate a 1024 element array with 32 arms with 32 logarithmically spaced antennas each, and calculate the noiseless visibilities from the synchrotron brightness model. We did this for a 6 km, 10 km, and 20 km array to see the noiseless response of different synthesized beam responses. The 1024 element layouts are seen over their respective lunar location in Figure 6.2. A more refined optimization of the array configuration that takes into account specific lunar geometries, cable length, point spread functions, and more is left for future work, and is described briefly in the Future Work section of the paper.

6.2.3 Imaging Performance

The noiseless recovered images of ~ 2 Jy stormy periods are seen in Figure 6.3. An important thing to note is the maximum of the colorbars in each of the panels. As the array is made smaller, the beam grows, reducing the resolution of the recovered image, but also making the features brighter because the beam takes in more signal. The sweet spot may be an array of 10 km since at that resolution 4 main synchrotron lobes are resolved unlike the 6 km array, but the lobes are twice as bright (albeit less well separated) than for the 20 km array. Images were made with a Briggs weighting scheme with a robustness parameter of -0.5, focusing more on resolution than noise reduction.

Now we add realistic noise to the radio visibilities. From [10], the interferometric noise for a single polarization can be calculated with

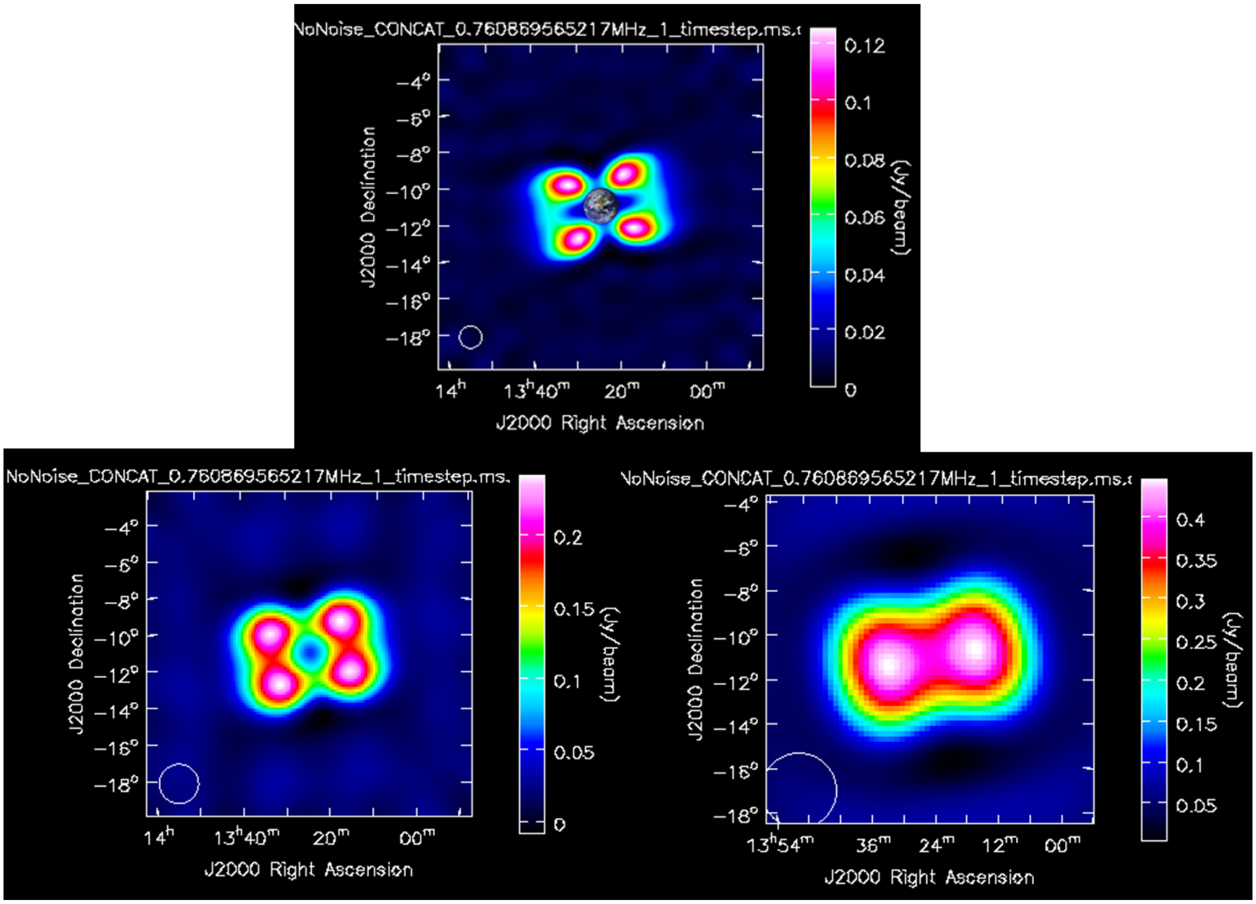

Figure 6.3: Noiseless Response of Different Sized Arrays to Synchrotron Emission of Stormy Radiation Belts. *Top*: Noiseless response of 20 km array. The 1.91° Earth is added in for a scale indicator. *Left*: Noiseless response of 10 km array. *Right*: Noiseless response of 6 km array. Images were made with a Briggs weighting scheme with a robustness parameter of -0.5.

$$\sigma = \frac{SEFD}{\eta_s \sqrt{N_{ant}(N_{ant}-1)\Delta\nu\Delta T}} \tag{6.3}$$

η_s is the system efficiency or correlator efficiency, which we have conservatively assumed to be 0.8. This efficiency is a function of how the correlator does its quantization, with more levels of quantization leading to less signal loss, but more computation with increasing sample rates. [140] provides a table of this correlator efficiency for a number of quantization levels, showing that for a Nyquist sampled voltage waveform, anything over 3 level quantization will lead to a correlator efficiency of over 0.8. This should not be a limiting factor since modern arrays such as the Very Large Array (VLA) use 8 bit sampling, leading to 256 quantization levels, and a correlator efficiency over 0.9. The System Equivalent Flux Density (SEFD) is a useful way to talk about a radio antenna's total noise because it ties in both the effective area and the system temperature, giving a simple way to compare the signal and the noise. We take the SEFD as the average noise over our operational science band described in section 3.4 and take $\Delta\nu$ to be 500 kHz.

Equation 6.3 is for point source sensitivity, and is valid because the Fourier transform of a delta function has a constant non-zero amplitude. For diffuse sources in the sky such as the radiation belts, the distribution of baselines is important. For the synchrotron emission belts, Figure 5.2 (b)

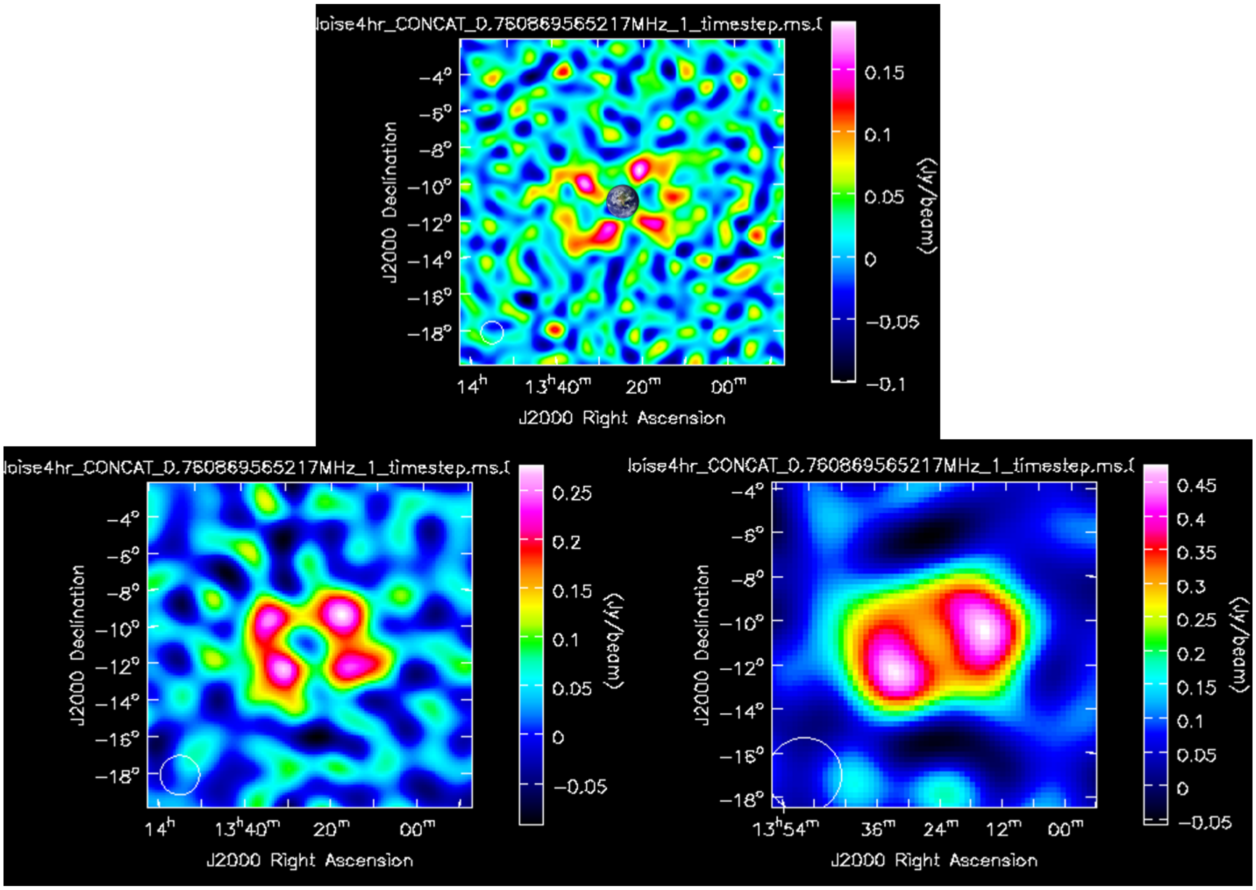

Figure 6.4: Recovered Dirty Images after 4 hours Integration with Optimal, Amplifier Limited Noise. *Top*: Noisy response of 20 km array, σ = .0318 Jy/beam $\Longrightarrow$ SNR $\approx$ 3.93 for each lobe. The 1.91° Earth is added in for a scale indicator. *Left*: Noisy response of 10 km array, σ = 0.041 Jy/beam $\Longrightarrow$ SNR $\approx$ 5.85 for each lobe. *Right*: Noisy response of 6 km array, σ = 0.073 Jy/beam $\Longrightarrow$ SNR $\approx$ 6.44 per lobe. Images were made with a Briggs weighting scheme with a robustness parameter of -0.5, and are showed here completely unCLEANed.

shows that most of the power is in a couple 10s of wavelengths, with generally more power the shorter the baseline. This means the amount of signal added from a baseline is not constant, and imaging software like CASA is needed to understand what the SNR would be for a given array configuration imaging diffuse structures such as the synchrotron emission from radiation belts. The units for the Signal and Noise in the recovered images from an interferometer are Jy/beam. Figure 5.2 (c) also shows that the 3 areas of UV space that the most power have phases close to either 0°, $180°$, or $-180°$. This will be a useful check on the real measurements, and may be used to detect errors in phase measurement. However, we will not go into this advanced level of array calibration for this paper.

We treat the values with an appropriate amount of noise, using Equation 6.3 with N_{Ant} = 2 for each visibility. Equation 6.3 also tells us that overall noise decreases roughly linearly with increasing N_{Ant}. We can use our 1024 element model to estimate a 16384 element array by dividing the noise by 16, as long as we assume the expanded array has a similar distribution of baselines. Under this assumption, a 16384 element array has ~256 similar baselines for every 1 baseline of a 1024 element array. So when adding all the visibility data to create an image, the Fourier sample for that baseline will have its noise decreased by a factor of $\sqrt{256} = 16$ when compared to the single corresponding baseline for a 1024 element array. So by dividing the noise from our 1024 element arrays by 16, we have simulated a 16384 element array spread over 6, 10 and 20 km. Recovered dirty images of stormy period synchrotron emission for a 4 hour integration time using 16384 receivers in an optimal, amplifier limited noise environment are seen in Figure 6.4. With the SNR in Jansky/beam from these simulations, we can come up with predicted times it would take to reach a given SNR for a particular noise environment. Data were imaged using a Briggs weighting scheme [141] with a robustness parameter of -0.5, so more on the uniform weighting side as opposed to natural weighting. This seemed to make the best images for this imaging target, with larger robustness values giving up too much resolution, while more negative values being noisier. The images are otherwise uncleaned, with 0 iterations of any sort of CLEANing algorithm.

From Figure 5.1, the average integrated spectral flux density for the radiation belts in a noisy storm period is 2 Jy over 500-1000 kHz, while for a calm period it is 1.4 Jy. The translates into needing an integration time roughly twice as long in order to reach a similar SNR for a given array. There is roughly a factor of 3.3 between optimal and moderate noise, and a factor of 3.16 between moderate and conservative noise. This means that to reach the same SNR takes $\sim$10 times longer in moderate environment than in the optimal, and also (at least) 10 times longer in the conservative regime over the moderate environment. So if the antenna array can be powered during lunar night, snapshots could be taken of the radiation belts every couple hours. On the other hand, electron densities over 1000/cm^3 at low Solar zenith angles (near lunar noon) could overwhelm the array to the small signal that the radiation belts give off. The expected integration times for a 16384 element array for our various noise budgets and array sizes is shown in Table 6.2.

Table 6.2: Expected Integration Times for 16384 Element Arrays of Various Sizes

Integration Time (minutes) for 16384 Element Array over 500 kHz	6 km array	10 km array	20 km array
Optimal Noise 3 σ Lobe Detection Calm	104	126	280
Optimal Noise 3 σ Lobe Detection Storm	52	63	140
Moderate Noise 3 σ Lobe Detection Calm	1132	1372	3050
Moderate Noise 3 σ Lobe Detection Storm	566	686	1525
Conservative Noise 3 σ Lobe Detection Calm	11096	13442	28873
Conservative Noise 3 σ Lobe Detection Storm	5548	6721	14936

6.3 Discussion

Imaging the synchrotron emission from the Earth's radiation belts at regular intervals would go a long way towards understanding the global response of Earth to variable Solar input. However, due to the relative weakness of the signal compared to the unavoidable noise sources from the lunar ionosphere and receiver electronics, thousands of antennas would be needed to get good measurements at a decent cadence. This paper outlines many of the transient noise sources and provides estimates of what it would take to achieve useful results, but it is only a first attempt at answering the problem. Many antenna design & implementation details would have to be taken into account for a real mission, a few of which are listed in the Future Work section.

Table 6.2 outlines the integration times needed for successful detections of the synchrotron emission under different conditions, saying that the data equivalent needed for a certain level of detection is X minutes times 500 kHz. There is an implicit optimism here because in reality, a flagging system would need to be implemented that could take out noisy channels that have other sources of unknown strength overpowering the synchrotron signal. This would mean it would likely take longer than stated in the table to actually reach the amount of data needed for a given SNR. Another important factor not mentioned so far is duty cycle. Most antennas are not recording data 100% of the time. A system where every antenna has a 50% duty cycle means that it would take twice as long to collect the same amount of signal.

Some useful takeaways from this paper are that $\sim$10 km seems to be a good compromise in array size because at that resolution 4 main synchrotron lobes are resolved, but are still relatively bright. A 10x10 km patch could hold over 440000 antennas if densely packed, but a circular distribution with many logarithmically spaced arms could make do with 16384 elements. Several low variance altitude regions near the Sub Earth point of the lunar surface were identified as promising array locations. This work also demonstrates a data processing pipeline combining SPICE, lunar surface data from LRO, and CASA that can generate the dirty images for a lunar array. The integration times required for detections are predicted to be highly dependent on Solar Zenith Angle, since less incident Sunlight will lead to fewer photoionized electrons, which will mean less quasithermal noise. This results in faster snapshots of the synchrotron emission as you move from lunar noon, to lunar late afternoon, to lunar night. This provides an incentive for a power supply system that can power the system as late as possible into the lunar night. This will require either highly efficient solar panels and batteries, or a radioisotope thermoelectric generator.

6.4 Future Work

As discussed in the Array Formation section, there are a number of optimizations that could be made to the array configuration. Logarithmically spaced circles are used as a stand-in, but in reality we would want to optimize the configuration, avoiding any small craters at the array site, minimizing key parameters such as total cable length, and designing the point spread function to have good UV coverage. In addition to increasing the imaging performance of the array, these optimizations can also help decrease construction costs.

Improvements in the simulations could be made by including a channel dependent simulated foreground removal for removable constant noise sources such as blackbody signals and Galactic background structure. The data processing pipeline could also use a fleshed out transient event detection scheme that removes flagged channels from the data that goes into the synchrotron emission imaging. The pipeline could then be tested on imaging these transient signals to demonstrate the degree of localization possible for a given SNR transient.

As discussed in the Amplifier Noise section, there is hardware specific characterization of the noise and impedance of the receiver to be done. [113] provides a useful guide to look to as they go through these processes for the Long Wavelength Array (LWA) antenna. Similar techniques would be used to analyze the response of our chosen antenna for a lunar based array. Mutual coupling and Galactic noise correlation can lead to a decrease in sensitivity for arrays with receivers less than a few wavelengths away from one another, as discussed in [142]. This is reflected in a increase in expected SEFD for the array, especially for beams formed over 10° from zenith. For beams near zenith the effects of coupling is frequency dependent, and may be better or worse than expected. For the purpose of imaging the Earth's synchrotron emission, the consequences from coupling are minimal since the array's location ensures that the Earth will always be near the sky's zenith. In order to unlock the array's full potential, studies of the expected SEFD as a function of elevation angle and frequency will have to be done, as [142] did for the LWA.

The NASA SMD recently chose the Radio wave Observations on the Lunar Surface of the photoElectron Sheath (ROLSES) mission with PI Robert MacDowall to put a STEREO WAVES inspired radio antenna on the lunar near side [143]. This will be an excellent pathfinder for many engineering aspects of the array not described in this paper, and will also finally provide direct measurements of the photoelectron sheath density near the surface over the course of the lunar day. This will solidify the noise budget in Figure 6.1, and will help drive requirements for signal to noise levels for all future lunar radio arrays. It will also provide occurrence rates and flux density levels for transient events detectable on the lunar near side. The instrument will be flown as part of the Commercial Lunar Payload Services (CLPS) program, where private landers will robotically deliver and deploy selected payloads. The expected Payload Delivery Date is August 2020. Another CLPS mission is Solar Cell Demonstration Platform for Enabling Long-Term Lunar Surface Power will demonstrate advanced solar arrays for longer mission duration. The expected Payload Delivery Date is March 2020.

CHAPTER 7

Conclusions

Low frequency radio astronomy is rapidly catching up with higher frequency astronomy. The field is soon set to break past the limits of Earth, and into space, free from the bounds of Earth's ionosphere that limits measurements below 10 MHz. This thesis has sketched out much of the data analysis pipelines and science analysis needed for radio arrays to detect a wide range of physical phenomena that create low frequency emissions. With this new leap into space comes a host of new challenges. In the realm of low frequency interferometry, simple signal to noise ratio (SNR) formulas do not always hold, since every pair of antenna is sampling a different Fourier component of the sky, the specific coherence pattern determined by the 3D separation between the antenna and the observing frequency.

For diffuse (i.e. non point like) structures in the sky, the Fourier transform of the sky brightness pattern is non-constant. This means the amount of signal added from a given pair of antenna is not constant, and imaging software like CASA [24] is needed to understand what the SNR would be for a given array configuration imaging diffuse structures with realistic noise. However, traditional radio astronomy software like CASA is hard coded to assume an Earth based array.

To circumvent this, I have created an altered version of CASA that can simulate space based arrays. My version takes new space based sources of localization error into account, and can accurately track the changing array configuration from an evolving orbital constellation, as opposed to the standard of Earth rotation synthesis. I have also created a version that employs lunar topological maps with orbital tracking software to make a version for lunar surface arrays. This simulation pipeline has been leveraged to make sure the concept arrays described in the text can meet their scientific objectives.

I have taken the reader through trade space studies in Chapter 2, showing how optimal communication strategies can change as one scales up the number of spacecraft in an array. In Chapter 3, I reviewed the current theory for Solar type II and III bursts, which are low frequency emissions caused from energetic particles from the Sun. I described how we can take the cutting edge physics to describe the dynamics of the inner corona of the Sun and propagate their solutions in time, recreating real events in simulations. I then showed how one can take plasma data from these simulations and create synthetic spectra to compare to the real spectra. I found that of the various theories of the location of the burst generation of type II bursts, the shock nose matched the shape of the real burst.

I then used these same data cuts of the 4 categories of theories of particle acceleration in Chapter 4 as input to test the proposed space based radio interferometer, SunRISE. SunRISE is the Sun Radio Interferometer Space Experiment that would for the first time directly image these type II and III bursts in the low radio frequencies. I have outlined the data processing and science analysis for this mission, tracking all the the sources of noise, and taking physically inspired test data from the MHD simulations to make sure that SunRISE could fulfill its mission requirements. On top of tracking regular thermal noise sources, novel aspects of the mission, specifically the positional awareness system, has its own set of uncertainties that carry over errors into the data. This frequency dependent phase noise from positional uncertainty was accounted for in the simulations. It was found to be slightly harmful at the upper range of 20 MHz, but did not stop SunRISE from completing its mission in simulated trials. We also outlined several other astrophysical targets that would be within SunRISE's sensitivity to detect. The pipeline used to simulate these measurements required a custom addition to the industry standard radio astronomy software, CASA. My addition allows the calculation of key parameters of the simulated array in a space based setting, including the projected baselines and visibility data.

This same pipeline architecture allows the simulation of larger arrays, such as RELIC. RELIC would be made of 32 spacecraft. An array of this size has high enough data transmission costs that having a mothership to transmit data for all the spacecraft is most economical, as shown in principle by the trade study in Chapter 2. A RELIC pipeline was created, again with realistic noise sources including positional uncertainty. I show that RELIC can image radio emission from galactic sources down to 100 arcsec wide, with 100 Jy total brightness. This sensitivity and resolution will open up an entirely new window into the universe, providing a detailed look at the lowest frequency sky for the first time.

I added additional elements to my space based radio pipeline, using LRO LOLA data to simulate radio arrays on the Lunar surface, using SPICE to align the Lunar frame to that of the Sky. This pipeline has enabled some simulation of powerful arrays pointed towards the Earth to image a range of low frequency magnetospheric emissions. Among the zoo of transient emissions such as AKR from the magnetosphere that are above the noise floor, there is a tantalizing target in the form of Synchrotron emission. Characterization of this emission with a large Lunar near side array would allow unprecedented proxy measurements of the global electron energy distribution. I was given realisitic models of the Earth's synchrotron emission from Lunar distances, and I propagated them through the defined Lunar array to show that this emission is detectable in theory. I have identified candidate sites for the arrays on the Lunar surface, near the sub–Earth point. I have sketched out a noise budget that will be solidified in 2020 once the ROLSES mission sends a radio antenna to the Lunar surface. There is plenty of work to be done on Lunar arrays, from understanding how to deal with the harsh thermal environment, to fine tuning array configurations, to simulating individual antenna response on top of the lunar regolith and deciding whether to include elements such as a ground plane.

Rarely does a single work push the field towards a previously unknown ripe area of research. Great minds of the past have often imagined things deemed fanciful and impractical in their original time, only to have the fruit of their idea grow ripe as the decades pass. In this vein, space based radio arrays have been dreamed about for over 30 years [144], and now many factors are pointing towards the idea that the time finally seems ripe for low frequency radio astronomy to make its move to outer space. Both the reliability and decreasing costs of small satellites is a huge game changer for the entire space industry, incentivizing mission designs that can take advantage of the distributive nature of multiple small inexpensive spacecraft to do the jobs traditionally done by larger, more costly spacecraft. Because of the long wavelengths of the radiation of interest, low frequency radio astronomy requires the distance between receivers on the scale of kilometers, far exceeding the practical size of a single spacecraft. Industry has finally caught up with the dreamers, which means it's time for the dreamers to become the makers. This thesis is a step towards making the dream of space based radio arrays a reality.

BIBLIOGRAPHY

[1] Zarka, P., “Plasma interactions of exoplanets with their parent star and associated radio emissions,” *Planetary and Space Science*, Vol. 55, April 2007, pp. 598–617.

[2] Thompson, A. R., Moran, J. M., and Swenson, G. W., *Interferometry and synthesis in radio astronomy*, 1986.

[3] Leblanc, Y., Dulk, G. A., and Bougeret, J.-L., “Tracing the Electron Density from the Corona to 1 au,” *Solar Physics*, Vol. 183, No. 1, Nov 1998, pp. 165–180.

[4] Kontar, E. P., Yu, S., Kuznetsov, A. A., Emslie, A. G., Alcock, B., Jeffrey, N. L. S., Melnik, V. N., Bian, N. H., and Subramanian, P., “Imaging spectroscopy of solar radio burst fine structures,” *Nature Communications*, Vol. 8, No. 1, 2017, pp. 1515.

[5] Reid, H. A. S. and Ratcliffe, H., “A review of solar type III radio bursts,” *Research in Astronomy and Astrophysics*, Vol. 14, July 2014, pp. 773–804.

[6] Melrose, D. B., “Coherent emission,” *Proceedings of the International Astronomical Union*, Vol. 4, No. S257, 2008, pp. 305315.

[7] Krupar, V., Maksimovic, M., Kontar, E. P., Zaslavsky, A., Santolik, O., Soucek, J., Kruparova, O., Eastwood, J. P., and Szabo, A., “Interplanetary Type III Bursts and Electron Density Fluctuations in the Solar Wind,” *The Astrophysical Journal*, Vol. 857, No. 2, apr 2018, pp. 82.

[8] Laing, R. A., Riley, J. M., and Longair, M. S., “Bright radio sources at 178 MHz - Flux densities, optical identifications and the cosmological evolution of powerful radio galaxies,” *MNRAS* , Vol. 204, July 1983, pp. 151–187.

[9] Jansky, K. G., *Directional Studies of Atmospherics at High Frequencies*, Springer Netherlands, Dordrecht, 1982, pp. 10–22.

[10] Taylor, G. B., Carilli, C. L., and Perley, R. A., editors, *Synthesis Imaging in Radio Astronomy II*, Vol. 180 of *Astronomical Society of the Pacific Conference Series*, 1999.

[11] Event Horizon Telescope Collaboration, Akiyama, K., Alberdi, A., Alef, W., Asada, K., Azulay, R., Baczko, A.-K., Ball, D., Baloković, M., Barrett, J., and et al., “First M87 Event Horizon Telescope Results. II. Array and Instrumentation,” *The Astrophysical Journal*, Vol. 875, April 2019, pp. L2.

[12] Event Horizon Telescope Collaboration, Akiyama, K., Alberdi, A., Alef, W., Asada, K., Azulay, R., Baczko, A.-K., Ball, D., Baloković, M., Barrett, J., and et al., "First M87 Event Horizon Telescope Results. III. Data Processing and Calibration," *The Astrophysical Journal*, Vol. 875, April 2019, pp. L3.

[13] Event Horizon Telescope Collaboration, Akiyama, K., Alberdi, A., Alef, W., Asada, K., Azulay, R., Baczko, A.-K., Ball, D., Baloković, M., Barrett, J., and et al., "First M87 Event Horizon Telescope Results. IV. Imaging the Central Supermassive Black Hole," *The Astrophysical Journal*, Vol. 875, April 2019, pp. L4.

[14] Orru, E. O. and Intema, H., "The case of 3C326: VLA 74 MHz observations during a geomagnetic storm," *ISKAF2010 Science Meeting*, Jan 2010, p. 75.

[15] Condon, J. J., Cotton, W. D., Fomalont, E. B., Kellermann, K. I., Miller, N., Perley, R. A., Scott, D., Vernstrom, T., and Wall, J. V., "Resolving the Radio Source Background: Deeper Understanding through Confusion," *ApJ* , Vol. 758, No. 1, Oct 2012, pp. 23.

[16] Condon, J. J., "Confusion and Flux-Density Error Distributions," *ApJ* , Vol. 188, March 1974, pp. 279–286.

[17] Jones, D. L., Weiler, K. W., Allen, R. J., Desch, M. M., Erickson, W. C., Kaiser, M. L., Kassim, N. E., Kuiper, T. B. H., Mahoney, M. J., Marsh, K. A., Perley, R. A., Preston, R. A., and Stone, R. G., "The Astronomical Low-Frequency Array (ALFA)," *IAU Colloq. 164: Radio Emission from Galactic and Extragalactic Compact Sources*, edited by J. A. Zensus, G. B. Taylor, and J. M. Wrobel, Vol. 144 of *Astronomical Society of the Pacific Conference Series*, 1998, p. 393.

[18] MacDowall, R. J., Bale, S. D., Demaio, L., Gopalswamy, N., Jones, D. L., Kaiser, M. L., Kasper, J. C., Reiner, M. J., and Weiler, K. W., "Solar Imaging Radio Array (SIRA): a multispacecraft mission," *Enabling Sensor and Platform Technologies for Spaceborne Remote Sensing*, edited by G. J. Komar, J. Wang, and T. Kimura, Vol. 5659 of *Proc. SPIE* , Jan. 2005, pp. 284–292.

[19] Cecconi, B., Dekkali, M., Briand, C., Segret, B., Girard, J. N., Laurens, A., Lamy, A., Valat, D., Delpech, M., Bruno, M., Glard, P., Bucher, M., Nenon, Q., Griemeier, J., Boonstra, A., and Bentum, M., "NOIRE study report: Towards a low frequency radio interferometer in space," *2018 IEEE Aerospace Conference*, March 2018, pp. 1–19.

[20] Sundkvist, D. J., Saint-Hilaire, P., Bain, H. M., Bale, S. D., Bonnell, J. W., Hurford, G. J., Maruca, B., Martinez Oliveros, J. C., and Pulupa, M., "CURIE: Cubesat Radio Interferometry Experiment," *AGU Fall Meeting Abstracts*, Dec. 2016, pp. SH11C–2271.

[21] Boonstra, A., Garrett, M., Kruithof, G., Wise, M., van Ardenne, A., Yan, J., Wu, J., Zheng, J., Gill, E. K. A., Guo, J., Bentum, M., Girard, J. N., Hong, X., An, T., Falcke, H., Klein-Wolt, M., Wu, S., Chen, W., Koopmans, L., Rothkaehl, H., Chen, X., Huang, M., Chen, L., Gurvits, L., Zarka, P., Cecconi, B., and de Haan, H., "Discovering the sky at the Longest Wavelengths (DSL)," *2016 IEEE Aerospace Conference*, March 2016, pp. 1–20.

[22] Rajan, R. T., Engelen, S., Bentum, M., and Verhoeven, C., "Orbiting Low Frequency Array for radio astronomy," *2011 Aerospace Conference*, March 2011, pp. 1–11.

[23] Martí-Vidal, I., Pérez-Torres, M. A., and Lobanov, A. P., "Over-resolution of compact sources in interferometric observations," *Astronomy & Astrophysics*, Vol. 541, May 2012, pp. A135.

[24] McMullin, J. P., Waters, B., Schiebel, D., Young, W., and Golap, K., "CASA Architecture and Applications," *Astronomical Data Analysis Software and Systems XVI*, edited by R. A. Shaw, F. Hill, and D. J. Bell, Vol. 376 of *Astronomical Society of the Pacific Conference Series*, Oct. 2007, p. 127.

[25] Kraus, J. D. and Marhefka, R. J., *Antennas for all applications*, 2002.

[26] Zaslavsky, A., Meyer-Vernet, N., Hoang, S., Maksimovic, M., and Bale, S. D., "On the antenna calibration of space radio instruments using the galactic background: General formulas and application to STEREO/WAVES," *Radio Science*, Vol. 46, No. 2, 2011.

[27] Alibay, F., Hegedus, A. M., Kasper, J. C., Lazio, T. J. W., and Neilsen, T., "SunRISE status: Concept development update," *2018 IEEE Aerospace Conference*, March 2018, pp. 1–11.

[28] Belov, K., Branch, A., Broschart, S., Castillo-Rogez, J., Chien, S., Clare, L., Dengler, R., Gao, J., Garza, D., Hegedus, A., Hernandez, S., Herzig, S., Imken, T., Kim, H., Mandutianu, S., Romero-Wolf, A., Schaffer, S., Troesch, M., Wyatt, E. J., and Lazio, J., "A space-based decametric wavelength radio telescope concept," *Experimental Astronomy*, Vol. 46, No. 2, Nov 2018, pp. 241–284.

[29] Alibay, F., Kasper, J. C., Lazio, T. J. W., and Neilsen, T., "Sun radio interferometer space experiment (SunRISE): Tracking particle acceleration and transport in the inner heliosphere," *2017 IEEE Aerospace Conference*, March 2017, pp. 1–15.

[30] Espley, J. R., "If It Has a Magnetic Field We Want to Measure It: Planetary Magnetometry of the Future," *Planetary Science Vision 2050 Workshop*, Vol. 1989 of *LPI Contributions*, Feb. 2017, p. 8058.

[31] Gaier, T., Kangaslahti, P., Lambrigtsen, B., Ramos-Perez, I., Tanner, A., McKague, D., Ruf, C., Flynn, M., Zhang, Z., Backhus, R., and Austerberry, D., "A 180 GHz prototype for a geostationary microwave imager/sounder-GeoSTAR-III," *2016 IEEE International Geoscience and Remote Sensing Symposium (IGARSS)*, July 2016, pp. 2021–2023.

[32] Hegedus, A. M., Soriano, M. A., Kurum, A., and Kasper, J. C., "Correlators for Synthetic Apertures in Space," *2019 IEEE Aerospace Conference*, March 2019, pp. 1–9.

[33] Rajan, R. T., Bentum, M., Gunst, A., and Boonstra, A., "Distributed correlators for interferometry in space," *2013 IEEE Aerospace Conference*, March 2013, pp. 1–9.

[34] Rajan, R. T., Bentum, M., and Boonstra, A., "Synchronization for space based ultra low frequency interferometry," *2013 IEEE Aerospace Conference*, March 2013, pp. 1–8.

[35] Engelen, S., Verhoeven, C., and Bentum, M., “OLFAR, a radio telescope based on nano satellites in moon orbit,” *24th Annual Conference on Small Satellites*, Utah State University, 8 2010, pp. 1–7.

[36] Zhou, D., “A Review of Polyphase Filter Banks and their Application,” Sep 2006.

[37] Haines, B. J., Armatys, M. J., Bar-Sever, Y. E., Bertiger, W. I., Desai, S. D., Dorsey, A. R., Lane, C. M., and Weiss, J. P., “One-Centimeter Orbits in Near-Real Time: The GPS Experience on OSTM/Jason-2,” *The Journal of the Astronautical Sciences*, Vol. 58, No. 3, Jul 2011, pp. 445–459.

[38] Jet Propulsion Laboratory, C. I. o. T., “GIPSY-OASIS Orbit and Clock Data Products,” 2019.

[39] Hegedus, A. M., Kasper, J. C., Lazio, J. W., Romero-Wolf, A., and Manchester, W., “The Data Processing Pipeline and Science Analysis of the Sun Radio Interferometer Space Experiment,” *2019 IEEE Aerospace Conference*, March 2019, pp. 1–10.

[40] National Imagery and Mapping Agency, “Department of Defense World Geodetic System 1984: its definition and relationships with local geodetic systems,” Tech. Rep. TR8350.2, National Imagery and Mapping Agency, St. Louis, MO, USA, Jan. 2000.

[41] Xilinx, “Zynq-7000 SoC Data Sheet: Overview,” 2018.

[42] Xilinx, “Radiation-Hardened, Space-GradeVirtex-5QV Family Data Sheet:Overview,” 2018.

[43] Aerospace, C., “EDGE Payload Processor Fact Sheet,” 2017.

[44] Network, D. S., “Deep Space Network Services Catalog,” 2015.

[45] Reames, D. V., “The Two Sources of Solar Energetic Particles,” *Space Science Reviews*, Vol. 175, No. 1, Jun 2013, pp. 53–92.

[46] Winter, L. M. and Ledbetter, K., “TYPE II AND TYPE III RADIO BURSTS AND THEIR CORRELATION WITH SOLAR ENERGETIC PROTON EVENTS,” *The Astrophysical Journal*, Vol. 809, No. 1, aug 2015, pp. 105.

[47] Aguilar-Rodriguez, E., Gopalswamy, N., MacDowall, R., Yashiro, S., and Kaiser, M. L., “A universal characteristic of type II radio bursts,” *Journal of Geophysical Research: Space Physics*, Vol. 110, No. A12, 2005.

[48] Tylka, A. J., Cohen, C. M. S., Dietrich, W. F., Lee, M. A., Maclennan, C. G., Mewaldt, R. A., Ng, C. K., and Reames, D. V., “Shock Geometry, Seed Populations, and the Origin of Variable Elemental Composition at High Energies in Large Gradual Solar Particle Events,” *The Astrophysical Journal*, Vol. 625, No. 1, may 2005, pp. 474–495.

[49] Tylka, A. J. and Lee, M. A., “A Model for Spectral and Compositional Variability at High Energies in Large, Gradual Solar Particle Events,” *The Astrophysical Journal*, Vol. 646, No. 2, aug 2006, pp. 1319–1334.

[50] Tylka, A. J. and Lee, M. A., *Spectral and Compositional Characteristics of Gradual and Impulsive Solar Energetic Particle Events*, American Geophysical Union (AGU), 2013, pp. 263–274.

[51] Schwadron, N. A., Lee, M. A., Gorby, M., Lugaz, N., Spence, H. E., Desai, M., Trk, T., Downs, C., Linker, J., Lionello, R., Mikić, Z., Riley, P., Giacalone, J., Jokipii, J. R., Kota, J., and Kozarev, K., "PARTICLE ACCELERATION AT LOW CORONAL COMPRESSION REGIONS AND SHOCKS," *The Astrophysical Journal*, Vol. 810, No. 2, sep 2015, pp. 97.

[52] Forbes, T. G. and Isenberg, P. A., "A catastrophe mechanism for coronal mass ejections," *The Astrophysical Journal*, Vol. 373, May 1991, pp. 294–307.

[53] Forbes, T. G. and Priest, E. R., "Photospheric Magnetic Field Evolution and Eruptive Flares," *The Astrophysical Journal*, Vol. 446, June 1995, pp. 377.

[54] Zank, G. P., Hunana, P., Mostafavi, P., Roux, J. A. L., Li, G., Webb, G. M., Khabarova, O., Cummings, A., Stone, E., and Decker, R., "DIFFUSIVE SHOCK ACCELERATION AND RECONNECTION ACCELERATION PROCESSES," *The Astrophysical Journal*, Vol. 814, No. 2, nov 2015, pp. 137.

[55] Ginzburg, V. L. and Zhelezniakov, V. V., "On the Possible Mechanisms of Sporadic Solar Radio Emission (Radiation in an Isotropic Plasma)," *Soviet Astronomy*, Vol. 2, Oct. 1958, pp. 653.

[56] Fermi, E., "On the Origin of the Cosmic Radiation," *Phys. Rev.*, Vol. 75, Apr 1949, pp. 1169–1174.

[57] Pulupa, M. P., Bale, S. D., and Kasper, J. C., "Langmuir waves upstream of interplanetary shocks: Dependence on shock and plasma parameters," *Journal of Geophysical Research (Space Physics)*, Vol. 115, April 2010, pp. A04106.

[58] Tth, G., van der Holst, B., Sokolov, I. V., Zeeuw, D. L. D., Gombosi, T. I., Fang, F., Manchester, W. B., Meng, X., Najib, D., Powell, K. G., Stout, Q. F., Glocer, A., Ma, Y.-J., and Opher, M., "Adaptive numerical algorithms in space weather modeling," *Journal of Computational Physics*, Vol. 231, No. 3, 2012, pp. 870 – 903, Special Issue: Computational Plasma Physics.

[59] Gombosi, T. I., Powell, K. G., De Zeeuw, D. L., Clauer, C. R., Hansen, K. C., Manchester, W. B., Ridley, A. J., Roussev, I. I., Sokolov, I. V., Stout, Q. F., and Toth, G., "Solution-adaptive magnetohydrodynamics for space plasmas: Sun-to-Earth simulations," *Computing in Science Engineering*, Vol. 6, No. 2, March 2004, pp. 14–35.

[60] van der Holst, B., Sokolov, I. V., Meng, X., Jin, M., W. B. Manchester, I., Tóth, G., and Gombosi, T. I., "ALFVÉN WAVE SOLAR MODEL (AWSoM): CORONAL HEATING," *The Astrophysical Journal*, Vol. 782, No. 2, jan 2014, pp. 81.

[61] Chandran, B. D. G., Dennis, T. J., Quataert, E., and Bale, S. D., “INCORPORATING KINETIC PHYSICS INTO A TWO-FLUID SOLAR-WIND MODEL WITH TEMPERATURE ANISOTROPY AND LOW-FREQUENCY ALFVÉN-WAVE TURBULENCE,” *The Astrophysical Journal*, Vol. 743, No. 2, dec 2011, pp. 197.

[62] Manchester, IV, W. B., van der Holst, B., and Lavraud, B., “Flux rope evolution in interplanetary coronal mass ejections: the 13 May 2005 event,” *Plasma Physics and Controlled Fusion*, Vol. 56, No. 6, June 2014, pp. 064006.

[63] Takakura, T., “Some Characteristics of Solar Radio Type IV Bursts,” *PASJ* , Vol. 15, 1963, pp. 327.

[64] Bastian, T. S., “Angular scattering of solar radio emission by coronal turbulence,” *ApJ* , Vol. 426, May 1994, pp. 774–781.

[65] Cane, H. V., “Spectra of the non-thermal radio radiation from the galactic polar regions,” *Monthly Notices of the Royal Astronomical Society*, Vol. 189, No. 3, 12 1979, pp. 465–478.

[66] Evans, S., Taber, W., Drain, T., Smith, J., Wu, H.-C., Guevara, M., Sunseri, R., and Evans, J., “MONTE: the next generation of mission design and navigation software,” *CEAS Space Journal*, Vol. 10, March 2018, pp. 79–86.

[67] Högbom, J. A., “Aperture Synthesis with a Non-Regular Distribution of Interferometer Baselines,” *Astronomy and Astrophysics Supplement*, Vol. 15, June 1974, pp. 417.

[68] Chevalier, R. A., Oegerle, W. R., and Scott, J. S., “Further studies of particle acceleration in Cassiopeia A.” *ApJ* , Vol. 222, Jun 1978, pp. 527–536.

[69] Gull, S. F., “A numerical model of the structure and evolution of young supernovaremnants,” *MNRAS* , Vol. 161, Jan 1973, pp. 47–69.

[70] Cowsik, R. and Sarkar, S., “The evolution of supernova remnants as radio sources.” *MNRAS* , Vol. 207, Apr 1984, pp. 745–775.

[71] Helmboldt, J. F. and Kassim, N. E., “THE EVOLUTION OF CASSIOPEIA A AT LOW RADIO FREQUENCIES,” *The Astronomical Journal*, Vol. 138, No. 3, jul 2009, pp. 838–844.

[72] Arias, M., Vink, J., de Gasperin, F., Salas, P., Oonk, J. B. R., van Weeren, R. J., van Amesfoort, A. S., Anderson, J., Beck, R., Bell, M. E., Bentum, M. J., Best, P., Blaauw, R., Breitling, F., Broderick, J. W., Brouw, W. N., Brüggen, M., Butcher, H. R., Ciardi, B., de Geus, E., Deller, A., van Dijk, P. C. G., Duscha, S., Eislöffel, J., Garrett, M. A., Grießmeier, J. M., Gunst, A. W., van Haarlem, M. P., Heald, G., Hessels, J., Hörandel, J., Holties, H. A., van der Horst, A. J., Iacobelli, M., Juette, E., Krankowski, A., van Leeuwen, J., Mann, G., McKay-Bukowski, D., McKean, J. P., Mulder, H., Nelles, A., Orru, E., Paas, H., Pandey-Pommier, M., Pandey, V. N., Pekal, R., Pizzo, R., Polatidis, A. G., Reich, W., Röttgering, H. J. A., Rothkaehl, H., Schwarz, D. J., Smirnov, O., Soida, M., Steinmetz, M., Tagger, M., Thoudam, S., Toribio, M. C., Vocks, C., van der Wiel, M. H. D., Wijers, R. A. M. J.,

Wucknitz, O., Zarka, P., and Zucca, P., "Low-frequency radio absorption in Cassiopeia A," *A&A*, Vol. 612, 2018, pp. A110.

[73] Cordes, J. M., "Low frequency interstellar scattering and pulsar observations," *Low Frequency Astrophysics from Space*, edited by N. E. Kassim and K. W. Weiler, Vol. 362 of *Lecture Notes in Physics, Berlin Springer Verlag*, 1990, pp. 165–174.

[74] Gurnett, D. A., "The Earth as a radio source: Terrestrial kilometric radiation," *Journal of Geophysical Research (1896-1977)*, Vol. 79, No. 28, 1974, pp. 4227–4238.

[75] Wu, C. S. and Lee, L. C., "A theory of the terrestrial kilometric radiation," *The Astrophysical Journal*, Vol. 230, June 1979, pp. 621–626.

[76] Calvert, W., "The auroral plasma cavity," *Geophysical Research Letters*, Vol. 8, No. 8, 1981, pp. 919–921.

[77] Mutel, R. L., Christopher, I. W., and Pickett, J. S., "Cluster multispacecraft determination of AKR angular beaming," *Geophysical Research Letters*, Vol. 35, No. 7, 2008.

[78] Lamy, L., Zarka, P., Cecconi, B., and Prangé, R., "AKR diurnal, semi-diurnal and shorter term modulations disentangled by Cassini/RPWS observations," *J. Geophys. Res.*, Vol. 115, No. A09221, 2010.

[79] Sazhin, S., Bullough, K., and Hayakawa, M., "Auroral hiss: a review," *Planetary and Space Science*, Vol. 41, No. 2, 1993, pp. 153 – 166.

[80] Ondoh, T., *Polar Hiss Observed by Isis Satellites*, American Geophysical Union (AGU), 2013, pp. 387–398.

[81] LaBelle, J., Shepherd, S. G., and Trimpi, M. L., "Observations of auroral medium frequency bursts," *Journal of Geophysical Research*, Vol. 102, Sept. 1997, pp. 22221–22232.

[82] LaBelle, J., Trimpi, M. L., Brittain, R., and Weatherwax, A. T., "Fine structure of auroral roar emissions," *Journal of Geophysical Research: Space Physics*, Vol. 100, No. A11, 1995, pp. 21953–21959.

[83] Hughes, J. M. and LaBelle, J., "The latitude dependence of auroral roar," *Journal of Geophysical Research: Space Physics*, Vol. 103, No. A7, 1998, pp. 14911–14915.

[84] Morgan, D. and A. Gurnett, D., "The source location and beaming of terrestrial continuum radiation," *Journal of Geophysical Research*, Vol. 96, 06 1991, pp. 9595–9613.

[85] Bolton, S. J., Janssen, M., Thorne, R., Levin, S., Klein, M., Gulkis, S., Bastian, T., Sault, R., Elachi, C., Hofstadter, M., Bunker, A., Dulk, G., Gudim, E., Hamilton, G., Johnson, W. T. K., Leblanc, Y., Liepack, O., McLeod, R., Roller, J., Roth, L., and West, R., "Ultra-relativistic electrons in Jupiter's radiation belts," *Nature*, Vol. 415, Feb 2002, pp. 987.

[86] Carr, T. D., Desch, M. D., and Alexander, J. K., *Phenomenology of magnetospheric radio emissions*, 1983, pp. 226–284.

[87] Pacholczyk, A. G., *Radio astrophysics. Nonthermal processes in galactic and extragalactic sources*, 1970.

[88] Santos-Costa, D. and Bolton, S. J., "Discussing the processes constraining the Jovian synchrotron radio emission's features," *Planetary and Space Science*, Vol. 56, No. 3, 2008, pp. 326 – 345.

[89] Girard, J. N., Zarka, P., Tasse, C., Hess, S., de Pater, I., Santos-Costa, D., Nenon, Q., Sicard, A., Bourdarie, S., Anderson, J., Asgekar, A., Bell, M. E., van Bemmel, I., Bentum, M. J., BErnardi, G., Best, P., Bonafede, A., Breitling, F., Breton, R. P., Broderick, J. W., Brouw, W. N., Bruggen, M., Ciardi, B., Corbel, S., Corstanje, A., de Gasperin, F., de Geus, E., Deller, A., Duscha, S., Eislöffel, J., Falcke, H., Frieswijk, W., Garrett, M. A., Grießmeier, J., Gunsing, Hessels, J. W. T., Hoeft, M., Hörandel, J., Iacobelli, M., Juette, E., Kondratiev, V. I., Kuniyoshi, M., Kuper, G., van Leeuwen, J., Loose, M., Maat, P., Mann, G., Markoff, S., McFadden, R., McKay-Bukowski, D., Moldon, J., Munk, H., Nelles, A., Norden, M. J., Orru, E., Paas, H., Pandey-Pommier, M., Pizzo, R., Polatidis, A. G., Reich, W., Röttgering, H., Rowlinson, A., Schwarz, D., Smirnov, O., Steinmetz, M., Swinbank, J., Tagger, M., Thoudam, S., Toribio, M. C., Vermeulen, R., Vocks, C., van Weeren, R. J., Wijers, R. A. M. J., and Wucknitz, O., "Imaging Jupiter's radiation belts down to 127 MHz with LOFAR," *Astronomy and Astrophysics*, Vol. 587, Feb. 2016, pp. A3.

[90] Santos-Costa, D. and Bourdarie, S. A., "Modeling the inner Jovian electron radiation belt including non-equatorial particles," *Planet. Space Sci*, Vol. 49, March 2001, pp. 303–312.

[91] Sicard, A. and Bourdarie, S., "Physical Electron Belt Model from Jupiter's surface to the orbit of Europa," *Journal of Geophysical Research: Space Physics*, Vol. 109, No. A2, 2004.

[92] Nnon, Q., Sicard, A., and Bourdarie, S., "A new physical model of the electron radiation belts of Jupiter inside Europa's orbit," *Journal of Geophysical Research: Space Physics*, Vol. 122, No. 5, 2017, pp. 5148–5167.

[93] Beutier, T. and Boscher, D., "A three-dimensional analysis of the electron radiation belt by the Salammbô code," *Journal of Geophysical Research: Space Physics*, Vol. 100, No. A8, 1995, pp. 14853–14861.

[94] Bourdarie, S., Boscher, D., Beutier, T., Sauvaud, J.-A., and Blanc, M., "Magnetic storm modeling in the Earth's electron belt by the Salammbô code," *Journal of Geophysical Research: Space Physics*, Vol. 101, No. A12, 1996, pp. 27171–27176.

[95] Boscher, D., Bourdarie, S., Thorne, R., and Abel, B., "Influence of the wave characteristics on the electron radiation belt distribution," *Advances in Space Research*, Vol. 26, No. 1, 2000, pp. 163 – 166, Space Weather: Physics and Applications.

[96] Santos-Costa, D., Bolton, S. J., Sault, R. J., Thorne, R. M., and Levin, S. M., "VLA observations at 6.2 cm of the response of Jupiter's electron belt to the July 2009 event," *Journal of Geophysical Research: Space Physics*, Vol. 116, No. A12, 2011.

[97] Santos-Costa, D., de Pater, I., Sault, R. J., Janssen, M. A., Levin, S. M., and Bolton, S. J., "Multifrequency analysis of the Jovian electron-belt radiation during the Cassini flyby of Jupiter," *Astronomy & Astrophysics*, Vol. 568, 2014, pp. A61.

[98] Han, S., Murakami, G., Kita, H., Tsuchiya, F., Tao, C., Misawa, H., Yamazaki, A., and Nakamura, M., "Investigating Solar Wind-Driven Electric Field Influence on Long-Term Dynamics of Jovian Synchrotron Radiation," *Journal of Geophysical Research: Space Physics*, Vol. 123, No. 11, 2018, pp. 9508–9516.

[99] Pierrard, V., Lopez Rosson, G., and Botek, E., "Dynamics of Megaelectron Volt Electrons Observed in the Inner Belt by PROBA-V/EPT," *Journal of Geophysical Research (Space Physics)*, Vol. 124, No. 3, Mar 2019, pp. 1651–1659.

[100] Angelopoulos, V., "The THEMIS Mission," *Space Science Reviews*, Vol. 141, Dec. 2008, pp. 5–34.

[101] Jun, I. and Garrett, H. B., "Comparison of high-energy trapped particle environments at the earth and jupiter," *Radiation Protection Dosimetry*, Vol. 116, No. 1-4, 12 2005, pp. 50–54.

[102] Maget, V., Sicard-Piet, A., Bourdarie, S., Lazaro, D., Turner, D. L., Daglis, I. A., and Sandberg, I., "Improved outer boundary conditions for outer radiation belt data assimilation using THEMIS-SST data and the Salammbo-EnKF code," *Journal of Geophysical Research: Space Physics*, Vol. 120, No. 7, 2015, pp. 5608–5622.

[103] Baker, D. N., Jaynes, A. N., Hoxie, V. C., Thorne, R. M., Foster, J. C., Li, X., Fennell, J. F., Wygant, J. R., Kanekal, S. G., Erickson, P. J., Kurth, W., Li, W., Ma, Q., Schiller, Q., Blum, L., Malaspina, D. M., Gerrard, A., and Lanzerotti, L. J., "An impenetrable barrier to ultrarelativistic electrons in the Van Allen radiation belts," *Nature*, Vol. 515, Nov 2014, pp. 531.

[104] Baker, D. N., Hoxie, V., Zhao, H., Jaynes, A. N., Kanekal, S., Li, X., and Elkington, S., "Multiyear Measurements of Radiation Belt Electrons: Acceleration, Transport, and Loss," *Journal of Geophysical Research: Space Physics*, Vol. 124, Mar 2019.

[105] Foster, J. C., Erickson, P. J., Baker, D. N., Jaynes, A. N., Mishin, E. V., Fennel, J. F., Li, X., Henderson, M. G., and Kanekal, S. G., "Observations of the impenetrable barrier, the plasmapause, and the VLF bubble during the 17 March 2015 storm," *Journal of Geophysical Research: Space Physics*, Vol. 121, No. 6, 2016, pp. 5537–5548.

[106] Bale, S. D., Ullrich, R., Goetz, K., Alster, N., Cecconi, B., Dekkali, M., Lingner, N. R., Macher, W., Manning, R. E., McCauley, J., Monson, S. J., Oswald, T. H., and Pulupa, M., "The Electric Antennas for the STEREO/WAVES Experiment," *Space Science Reviews*, Vol. 136, No. 1, Apr 2008, pp. 529–547.

[107] Bougeret, J. L., Goetz, K., Kaiser, M. L., Bale, S. D., Kellogg, P. J., Maksimovic, M., Monge, N., Monson, S. J., Astier, P. L., Davy, S., Dekkali, M., Hinze, J. J., Manning, R. E., Aguilar-Rodriguez, E., Bonnin, X., Briand, C., Cairns, I. H., Cattell, C. A., Cecconi, B., Eastwood, J., Ergun, R. E., Fainberg, J., Hoang, S., Huttunen, K. E. J., Krucker, S.,

Lecacheux, A., MacDowall, R. J., Macher, W., Mangeney, A., Meetre, C. A., Moussas, X., Nguyen, Q. N., Oswald, T. H., Pulupa, M., Reiner, M. J., Robinson, P. A., Rucker, H., Salem, C., Santolik, O., Silvis, J. M., Ullrich, R., Zarka, P., and Zouganelis, I., "S/WAVES: The Radio and Plasma Wave Investigation ontheSTEREO Mission," *Space Science Reviews*, Vol. 136, No. 1, Apr 2008, pp. 487–528.

[108] Novaco, J. C. and Brown, L. W., "Nonthermal galactic emission below 10 megahertz," *The Astrophysical Journal*, Vol. 221, April 1978, pp. 114–123.

[109] Manning, R. and Dulk, G. A., "The Galactic background radiation from 0.2 to 13.8 MHz," *Astronomy & Astrophysics*, Vol. 372, No. 2, 2001, pp. 663–666.

[110] Planck, M., *The Theory of Heat Radiation*, P. Blakiston's Son and Co., Philadelphia, PA, USA, 1914, Authorized translation by Morton Masius.

[111] Cornwell, T. J., "Multiscale CLEAN Deconvolution of Radio Synthesis Images," *IEEE Journal of Selected Topics in Signal Processing*, Vol. 2, No. 5, Oct 2008, pp. 793–801.

[112] Noordam, J. E., "LOFAR calibration challenges," *Ground-based Telescopes*, edited by J. M. Oschmann, Jr., Vol. 5489 of *Proc. SPIE* , Oct. 2004, pp. 817–825.

[113] Hicks, B. C., Paravastu-Dalal, N., Stewart, K. P., Erickson, W. C., Ray, P. S., Kassim, N. E., Burns, S., Clarke, T., Schmitt, H., Craig, J., Hartman, J., and Weiler, K. W., "A Wide-Band, Active Antenna System for Long Wavelength Radio Astronomy," *Publications of the Astronomical Society of the Pacific*, Vol. 124, No. 920, oct 2012, pp. 1090–1104.

[114] Meyer-Vernet, N. and Perche, C., "Tool kit for antennae and thermal noise near the plasma frequency," *Journal of Geophysical Research: Space Physics*, Vol. 94, No. A3, 1989, pp. 2405–2415.

[115] Meyer-Vernet, N., Hoang, S., Issautier, K., Moncuquet, M., and Marcos, G., *Plasma Thermal Noise: The Long Wavelength Radio Limit*, American Geophysical Union (AGU), 2000, pp. 67–74.

[116] Elsmore, B., "Radio observations of the lunar atmosphere," *The Philosophical Magazine: A Journal of Theoretical Experimental and Applied Physics*, Vol. 2, No. 20, 1957, pp. 1040–1046.

[117] Andrew, B. H., Branson, N. J. B. A., and Wills, D., "Radio observation of the Crab nebula during a lunar occultation," *Nature*, Vol. 203, 1964, pp. 171–173.

[118] Vasil'Ev, M. B., Vinogradov, V. A., Vyshlov, A. S., Ivanovskii, O. G., Kolosov, M. A., Savich, N. A., Samovol, V. A., Samoznaev, L. N., Sidorenko, A. I., Sheikhet, A. I., and Shtern, D. Y., "Radio Transparency of Circumlunar Space Using the Luna-19 Station," *Cosmic Research*, Vol. 12, Jan. 1974, pp. 102.

[119] Vyshlov, A. S., "Preliminary results of circumlunar plasma research by the Luna 22 spacecraft," *Space research XVI*, edited by M. J. Rycroft, 1976, pp. 945–949.

[120] Vyshlov, A. S. and Savich, N. A., "Observations of radio source occultations by the moon and the nature of the plasma near the moon," *Cosmic Research*, Vol. 16, Jan. 1979, pp. 551–556.

[121] Chandran, S. R., Renuka, G., and Venugopal, C., "Plasma electron temperature variability in lunar surface potential and in electric field under average solar wind conditions," *Advances in Space Research*, Vol. 51, No. 9, 2013, pp. 1622 – 1626.

[122] Imamura, T., Nabatov, A., Mochizuki, N., Iwata, T., Hanada, H., Matsumoto, K., Noda, H., Kono, Y., Liu, Q., Futaana, Y., Ando, H., Yamamoto, Z., Oyama, K.-I., and Saito, A., "Radio occultation measurement of the electron density near the lunar surface using a subsatellite on the SELENE mission," *Journal of Geophysical Research: Space Physics*, Vol. 117, No. A6, 2012.

[123] Stubbs, T., Glenar, D., Farrell, W., Vondrak, R., Collier, M., Halekas, J., and Delory, G., "On the role of dust in the lunar ionosphere," *Planetary and Space Science*, Vol. 59, No. 13, 2011, pp. 1659 – 1664, Exploring Phobos.

[124] Colwell, J. E., Batiste, S., Hornyi, M., Robertson, S., and Sture, S., "Lunar surface: Dust dynamics and regolith mechanics," *Reviews of Geophysics*, Vol. 45, No. 2, 2007.

[125] Mishra, S. K. and Misra, S., "An analytical investigation: Effect of solar wind on lunar photoelectron sheath," *Physics of Plasmas*, Vol. 25, No. 2, 2018, pp. 023702.

[126] Sodha, M. S. and Mishra, S. K., "Lunar photoelectron sheath and levitation of dust," *Physics of Plasmas*, Vol. 21, No. 9, 2014, pp. 093704.

[127] Chin, G., Brylow, S., Foote, M., Garvin, J., Kasper, J., Keller, J., Litvak, M., Mitrofanov, I., Paige, D., Raney, K., Robinson, M., Sanin, A., Smith, D., Spence, H., Spudis, P., Stern, S. A., and Zuber, M., "Lunar Reconnaissance Orbiter Overview: TheInstrument Suite and Mission," *Space Science Reviews*, Vol. 129, No. 4, Apr 2007, pp. 391–419.

[128] Barker, M., Mazarico, E., Neumann, G., Zuber, M., Haruyama, J., and Smith, D., "A new lunar digital elevation model from the Lunar Orbiter Laser Altimeter and SELENE Terrain Camera," *Icarus*, Vol. 273, 2016, pp. 346 – 355.

[129] Acton, C. H., "Ancillary data services of NASA's Navigation and Ancillary Information Facility," *Planetary and Space Science*, Vol. 44, Jan. 1996, pp. 65–70.

[130] Boone, F., "Interferometric array design: Optimizing the locations of the antenna pads," *A&A*, Vol. 377, No. 1, 2001, pp. 368–376.

[131] Boone, F., "Interferometric array design: Distributions of Fourier samples for imaging," *A&A*, Vol. 386, No. 3, 2002, pp. 1160–1171.

[132] Girard, J., "Dèveloppement de la Super Station LOFAR & observations planètaires avec LOFAR," *Instrumentation et mèthodes pour l'astrophysique [astro-ph.IM]. Thèse de Doctorat, Observatoire de Paris, France*, 2013.

[133] Zyma, K., Girard, J. N., Landquist, E., Schaper, G., and Vasko, F. J., "Formulating and solving a radio astronomy antenna connection problem as a generalized cable-trench problem: an empirical study," *International Transactions in Operational Research*, Vol. 24, No. 5, 2017, pp. 943–957.

[134] KETO, E., "HIERARCHICAL CONFIGURATIONS FOR CROSS-CORRELATION INTERFEROMETERS WITH MANY ELEMENTS," *Journal of Astronomical Instrumentation*, Vol. 01, No. 01, 2012, pp. 1250007.

[135] Woody, D., "Radio Interferometer Array Point Spread Functions II. Evaluation and Optimization," *ALMA Memo Series*, Vol. 390, 2001.

[136] Woody, D., "Radio Interferometer Array Point Spread Functions I. Theory and Statistics," *ALMA Memo Series*, Vol. 389, 2001.

[137] Tingay, S. J., Goeke, R., Bowman, J. D., Emrich, D., Ord, S. M., Mitchell, D. A., Morales, M. F., Booler, T., Crosse, B., Wayth, R. B., Lonsdale, C. J., Tremblay, S., Pallot, D., Colegate, T., Wicenec, A., Kudryavtseva, N., Arcus, W., Barnes, D., Bernardi, G., Briggs, F., Burns, S., Bunton, J. D., Cappallo, R. J., Corey, B. E., Deshpande, A., Desouza, L., Gaensler, B. M., Greenhill, L. J., Hall, P. J., Hazelton, B. J., Herne, D., Hewitt, J. N., Johnston-Hollitt, M., Kaplan, D. L., Kasper, J. C., Kincaid, B. B., Koenig, R., Kratzenberg, E., Lynch, M. J., Mckinley, B., Mcwhirter, S. R., Morgan, E., Oberoi, D., Pathikulangara, J., Prabu, T., Remillard, R. A., Rogers, A. E. E., Roshi, A., Salah, J. E., Sault, R. J., Udaya-Shankar, N., Schlagenhaufer, F., Srivani, K. S., Stevens, J., Subrahmanyan, R., Waterson, M., Webster, R. L., Whitney, A. R., Williams, A., Williams, C. L., and Wyithe, J. S. B., "The Murchison Widefield Array: The Square Kilometre Array Precursor at Low Radio Frequencies," *Publications of the Astronomical Society of Australia*, Vol. 30, Jan. 2013, pp. e007.

[138] van Haarlem, M. P., Wise, M. W., Gunst, A. W., Heald, G., McKean, J. P., Hessels, J. W. T., de Bruyn, A. G., Nijboer, R., Swinbank, J., Fallows, R., Brentjens, M., Nelles, A., Beck, R., Falcke, H., Fender, R., Hörandel, J., Koopmans, L. V. E., Mann, G., Miley, G., Röttgering, H., Stappers, B. W., Wijers, R. A. M. J., Zaroubi, S., van den Akker, M., Alexov, A., Anderson, J., Anderson, K., van Ardenne, A., Arts, M., Asgekar, A., Avruch, I. M., Batejat, F., Bähren, L., Bell, M. E., Bell, M. R., van Bemmel, I., Bennema, P., Bentum, M. J., Bernardi, G., Best, P., Bîrzan, L., Bonafede, A., Boonstra, A.-J., Braun, R., Bregman, J., Breitling, F., van de Brink, R. H., Broderick, J., Broekema, P. C., Brouw, W. N., Brüggen, M., Butcher, H. R., van Cappellen, W., Ciardi, B., Coenen, T., Conway, J., Coolen, A., Corstanje, A., Damstra, S., Davies, O., Deller, A. T., Dettmar, R.-J., van Diepen, G., Dijkstra, K., Donker, P., Doorduin, A., Dromer, J., Drost, M., van Duin, A., Eislöffel, J., van Enst, J., Ferrari, C., Frieswijk, W., Gankema, H., Garrett, M. A., de Gasperin, F., Gerbers, M., de Geus, E., Grießmeier, J.-M., Grit, T., Gruppen, P., Hamaker, J. P., Hassall, T., Hoeft, M., Holties, H. A., Horneffer, A., van der Horst, A., van Houwelingen, A., Huijgen, A., Iacobelli, M., Intema, H., Jackson, N., Jelic, V., de Jong, A., Juette, E., Kant, D., Karastergiou, A., Koers, A., Kollen, H., Kondratiev, V. I., Kooistra, E., Koopman, Y., Koster, A., Kuniyoshi, M., Kramer, M., Kuper, G., Lambropoulos, P., Law, C., van Leeuwen, J., Lemaitre, J., Loose, M., Maat, P., Macario, G., Markoff, S., Masters, J., McFadden, R. A., McKay-Bukowski,

D., Meijering, H., Meulman, H., Mevius, M., Middelberg, E., Millenaar, R., Miller-Jones, J. C. A., Mohan, R. N., Mol, J. D., Morawietz, J., Morganti, R., Mulcahy, D. D., Mulder, E., Munk, H., Nieuwenhuis, L., van Nieuwpoort, R., Noordam, J. E., Norden, M., Noutsos, A., Offringa, A. R., Olofsson, H., Omar, A., Orrú, E., Overeem, R., Paas, H., Pandey-Pommier, M., Pandey, V. N., Pizzo, R., Polatidis, A., Rafferty, D., Rawlings, S., Reich, W., de Reijer, J.-P., Reitsma, J., Renting, G. A., Riemers, P., Rol, E., Romein, J. W., Roosjen, J., Ruiter, M., Scaife, A., van der Schaaf, K., Scheers, B., Schellart, P., Schoenmakers, A., Schoonderbeek, G., Serylak, M., Shulevski, A., Sluman, J., Smirnov, O., Sobey, C., Spreeuw, H., Steinmetz, M., Sterks, C. G. M., Stiepel, H.-J., Stuurwold, K., Tagger, M., Tang, Y., Tasse, C., Thomas, I., Thoudam, S., Toribio, M. C., van der Tol, B., Usov, O., van Veelen, M., van der Veen, A.-J., ter Veen, S., Verbiest, J. P. W., Vermeulen, R., Vermaas, N., Vocks, C., Vogt, C., de Vos, M., van der Wal, E., van Weeren, R., Weggemans, H., Weltevrede, P., White, S., Wijnholds, S. J., Wilhelmsson, T., Wucknitz, O., Yatawatta, S., Zarka, P., Zensus, A., and van Zwieten, J., "LOFAR: The LOw-Frequency ARray," *A&A*, Vol. 556, 2013, pp. A2.

[139] Ellingson, S. W., Clarke, T. E., Cohen, A., Craig, J., Kassim, N. E., Pihlstrom, Y., Rickard, L. J., and Taylor, G. B., "The Long Wavelength Array," *Proceedings of the IEEE*, Vol. 97, No. 8, Aug 2009, pp. 1421–1430.

[140] Thompson, A. R., Emerson, D. T., and Schwab, F. R., "Convenient formulas for quantization efficiency," *Radio Science*, Vol. 42, No. 3, 2007.

[141] Briggs, D. S., Schwab, F. R., and Sramek, R. A., "Imaging," *Synthesis Imaging in Radio Astronomy II*, edited by G. B. Taylor, C. L. Carilli, and R. A. Perley, Vol. 180 of *Astronomical Society of the Pacific Conference Series*, Jan 1999, p. 127.

[142] Ellingson, S. W., "Sensitivity of Antenna Arrays for Long-Wavelength Radio Astronomy," *IEEE Transactions on Antennas and Propagation*, Vol. 59, No. 6, June 2011, pp. 1855–1863.

[143] Graham, S. and Reckart, T., "NASA-provided Lunar Payloads," Mar 2019.

[144] Weiler, K. W., Johnston, K. J., Simon, R. S., Dennison, B. K., Erickson, W. C., Kaiser, M. L., Cane, H. V., and Desch, M. D., "A low frequency radio array for space," *A&A* , Vol. 195, April 1988, pp. 372–379.